

---

## Articles publiés dans des revues à comité de lecture

- Guennou, C., Auchère, F., Klimchuk, J. A., Bocchialini, K., Parenti, S. Can the differential emission measure constrain the timescale of the energy deposition in the solar corona? *The Astrophysical Journal*, 2013, Volume 774, pp.31-44. (*Disponible en annexe D*)
- Dudok de Wit, T., Moussaoui, S., Guennou, C., Auchère, F., Cessateur, G., Kretzschmar, M., Vieira, L. A., Goryaev, F. F. Coronal Temperature Maps from Solar EUV Images : A Blind Source Separation Approach. *Solar Physics*, Volume 283, Issue 1, pp.31-47.
- Barbey, N., Guennou, C., Auchère, F. TomograPy : A Fast, Instrument-Independent, Solar Tomography Software. *Solar Physics*, Volume 283, Issue 1, pp.227-245.
- Guennou, C., Auchère, F., Bocchialini, K., Parenti, S., Barbey, N. On the Accuracy of the Differential Emission Measure Diagnostics of Solar Plasmas. Application to AIA/SDO. Part I : Isothermal plasmas. *The Astrophysical Journal Supplement*, 2012, Volume 203, Issue 2, article id. 25. (*Disponible en annexe B*)
- Guennou, C., Auchère, F., Bocchialini, K., Parenti, S., Barbey, N. On the Accuracy of the Differential Emission Measure Diagnostics of Solar Plasmas. Application to AIA/SDO. Part II : Multithermal plasmas. *The Astrophysical Journal Supplement*, 2012, Volume 203, Issue 2, article id. 26. (*Disponible en annexe C*)

---

## A.2

---

### Articles publiés dans des revues sans comité de lecture

- Auchère, F., Guennou, C., Barbey, N. Tomographic reconstruction of polar plumes. EAS Publications Series, Volume 55, 2012, pp.207-211.

---

## A.3

---

### Communication orales nationales et internationales

- Guennou, C., Auchère, F., Klimchuk, J. A., Bocchialini, K., Parenti, S. Can the differential emission measure constrain the timescale of the energy deposition in the solar corona? Sixth Coronal Loops Workshop, La Roche-en-Ardenne, Belgique, Juin 2013.
- Guennou, C., Auchère, F., Klimchuk, J. A., Bocchialini, K., Parenti, S. Can the differential emission measure constrain the timescale of the energy deposition in the solar corona? Celebrating the achievements of Alan Gabriel, Orsay, France, Juin 2013.
- Guennou, C., Auchère, F., Klimchuk, J. A., Bocchialini, K., Parenti, S. Can the differential emission measure constrain the timescale of the energy deposition in the solar corona? LWS/SDO-7 Science Workshop "Exploring the Network of SDO Science", Cambridge MD, États-Unis, Mars 2013.
- Guennou, C., Auchère, F., Klimchuk, J. A., Bocchialini, K., Parenti, S., Barbey N. Diagnostic de la structure thermique de la couronne solaire : outils 2D et 3D, Centre de Recherche en Astronomie, Astrophysique et Géologie, Bouzareah, Alger, Algérie, février 2013.
- Guennou, C., Auchère, F., Seaton, D. Tomographic reconstruction of the solar corona using SWAP data. Nine European Space Weather Week, Bruxelles, Belgique, Novembre 2012.
- Guennou, C., Auchère, F., Klimchuk, J. A., Bocchialini, K., Parenti, S. Can the differential emission measure constrain the timescale of the energy deposition in the solar corona? COSPAR Scientific Assembly, Mysore, Bangalore, India, juillet 2012.
- Guennou, C., Auchère, F., Klimchuk, J. A., Bocchialini, K., Parenti, S., Barbey N. On the accuracy of the differential emission measure analysis : application to SDO/AIA and Hinode/EIS. Nasa Goddard Space Flight center, Greenbelt, MD, États-unis, juillet 2012.
- Guennou, C., Auchère, F., Bocchialini, K., Parenti, S., Barbey N. On the accuracy of the differential emission measure analysis : application to SDO/AIA. Fifth Coronal Loop Workshop, Palma de Mallorca, Espagne, juin 2011.

- Guennou, C., Auchère, F., Bocchialini, K., Parenti, S., Barbey N. On the accuracy of the differential emission measure analysis : application to SDO/AIA. LWS/SDO-1 Science Workshop, Squaw Valley, États-unis, Mai 2011.





## On the accuracy of the Differential Emission Measure diagnostics of solar plasmas. Application to *SDO/AIA*. I. Isothermal Plasmas

### B.1

---

#### Résumé

Le formalisme de la Mesure d'Émission Différentielle (DEM) est l'un des outils les plus utilisés pour l'étude des atmosphères stellaires. Cependant, sa dérivation ainsi que son interprétation sont particulièrement difficiles, en particulier à cause de la nature inverse du problème et de la présence d'erreurs systématiques et aléatoires. Dans ce travail, nous examinons les propriétés de l'inversion des données *SDO/AIA*, à l'aide de simulations utilisant des modèles de DEMs simples. Cette stratégie permet l'exploration systématique de l'espace des paramètres, et en utilisant une approche statistique, on peut ensuite calculer les probabilités associées à chaque DEM cohérente avec les incertitudes sous-jacentes. En suivant cette méthodologie, plusieurs propriétés importantes du problème de l'inversion de DEM peuvent être déduites, mettant ainsi en évidence de nouvelles limitations. Dans ce premier article, le formalisme de notre approche est décrite, puis appliqué dans le cadre des plasmas isothermes, considérés comme des composants de bases pour comprendre le comportement de l'inversion plus complexe dans le cas des plasmas multitherme, étudiés dans le second article. Ainsi, le comportement de l'inversion peut être quantifié, et de nouveaux outils permettant d'interpréter correctement les DEM mesurées sont présentés. Les résultats décrits ici montrent que les six bandes spectrales d'AIA améliorent fortement la robustesse de l'inversion isotherme, avec une résolution comprise entre  $0.03$  et  $0.11 \log T_e$ .

### B.2

---

Article publié dans *The Astrophysical Journal*

ON THE ACCURACY OF THE DIFFERENTIAL EMISSION MEASURE DIAGNOSTICS OF SOLAR PLASMAS. APPLICATION TO *SDO/AIA*. I. ISOTHERMAL PLASMASC. GUENNOU<sup>1</sup>, F. AUCHÈRE<sup>1</sup>, E. SOUBRIÉ<sup>1</sup>, K. BOCCHIALINI<sup>1</sup>, S. PARENTI<sup>2</sup>, AND N. BARBEY<sup>3</sup><sup>1</sup> Institut d'Astrophysique Spatiale, Bâtiment 121, CNRS/Université Paris-Sud, F-91405 Orsay, France; [chloe.guennou@ias.u-psud.fr](mailto:chloe.guennou@ias.u-psud.fr)<sup>2</sup> Royal Observatory of Belgium, 3 Avenue Circulaire, B-1180 Bruxelles, Belgium<sup>3</sup> SAp/Irfu/DSM/CEA, Centre d'études de Saclay, Orme des Merisiers, Bâtiment 709, F-91191 Gif sur Yvette, France

Received 2012 June 18; accepted 2012 October 5; published 2012 November 21

## ABSTRACT

Differential emission measure (DEM) analysis is a major diagnostic tool for stellar atmospheres. However, both its derivation and its interpretation are notably difficult because of random and systematic errors, and the inverse nature of the problem. We use simulations with simple thermal distributions to investigate the inversion properties of *SDO/AIA* observations of the solar corona. This allows a systematic exploration of the parameter space, and using a statistical approach the respective probabilities of all the DEMs compatible with the uncertainties can be computed. Following this methodology, several important properties of the DEM inversion, including new limitations, can be derived and presented in a very synthetic fashion. In this first paper, we describe the formalism and we focus on isothermal plasmas as building blocks to understand the more complex DEMs studied in the second paper. The behavior of the inversion of AIA data being thus quantified, and we provide new tools to properly interpret the DEM. We quantify the improvement of the isothermal inversion with six AIA bands compared to previous EUV imagers. The maximum temperature resolution of AIA is found to be  $0.03 \log T_e$ , and we derive a rigorous test to quantify the compatibility of observations with the isothermal hypothesis. However, we demonstrate limitations in the ability of AIA alone to distinguish different physical conditions.

*Key words:* plasmas – Sun: corona – Sun: UV radiation

## 1. MOTIVATION

The differential emission measure (DEM) diagnostic technique offers crucial information about the thermal structuring of the solar and stellar atmospheres, providing a measure of the temperature distribution of plasma along the line of sight (LOS). However, to derive the DEM from a set of observations is a complex task, due to the inverse nature of the problem, and understanding its robustness and accuracy is still relevant today (e.g., Landi et al. 2011; Testa et al. 2012). Spectrometers are by nature better suited for DEM analysis than broadband imagers. However, because the latter generally offer a higher signal-to-noise ratio over a larger field of view (FOV), DEM codes have nevertheless been applied to the three coronal bands of the Extreme-ultraviolet Imaging Telescope (EIT; Delaboudinière et al. 1995) and the *Transition Region and Coronal Explorer (TRACE; Handy et al. 1999)*. However, these instruments were shown not to constrain the DEM enough to reach conclusive results. In recent years, the multiplication of passbands in instruments such as the X-Ray Telescope (XRT) on *Hinode* (Golub et al. 2007) and the Atmospheric Imaging Assembly (AIA) telescope (Lemen et al. 2012) has provided new prospects for reliably estimating the DEM simultaneously over a large FOV. Case studies of the properties of the inversion using these instruments have been published by, e.g., Martínez-Sykora et al. (2011) and Reale et al. (2009).

Building on these results, the central objective of the work presented in this series of papers is to provide a systematic characterization of the DEM reconstruction problem to assess both its accuracy and its robustness. Using our technique, the capabilities of a given instrument can be evaluated, and new tools facilitating the DEM interpretation are presented. We illustrate our methodology in the specific case of the six coronal bands of AIA, but the same principle can be applied to any set of broadband or spectroscopic measurements.

Initially introduced for element abundance measurements, and then further developed by, e.g., Jefferies et al. (1972) and Jordan (1976), the DEM formalism has been extensively used in the past several decades, for most types of coronal structures, such as polar coronal holes (Hahn et al. 2011), polar plumes (e.g., Del Zanna et al. 2003), streamers (e.g., Parenti et al. 2000), prominences (e.g., Wiik et al. 1993; Parenti & Vial 2007), quiet Sun (e.g., Landi & Landini 1998; Parenti & Vial 2007), bright points (Brosius et al. 2008), and active regions (e.g., Warren et al. 2011). The thermal structuring of the stellar coronae has also been investigated using DEM analysis (e.g., Sanz-Forcada et al. 2003). In particular, the DEM is one of the tools commonly used to study the thermal stability of the coronal structures mentioned above, and to diagnose the energy source balancing the observed radiative losses. For example, it can help to discriminate between steady or impulsive heating models predicting different loop thermal structures (see, e.g., Klimchuk 2006; Reale 2010; Susino et al. 2010; Winebarger et al. 2011). One approach is to establish the cross-field thermal structure of resolved loops, which is then compared to the DEM simulated for impulsively or steadily heated unresolved multi-stranded and monolithic loops.

However, reliably inferring the DEM from observations has proved to be a genuine challenge. The fundamental limitations of DEM inversion have been discussed by, e.g., Jefferies et al. (1972), Craig & Brown (1976), Brown et al. (1991), and Judge et al. (1997), including measurement noises, systematic errors, the width and shape of the contribution functions, and the associated consequences of multiple solutions and limited temperature resolution. Many DEM inversion algorithms have been proposed to cope with these limitations, each with its own strengths and weaknesses (e.g., Withbroe 1975; Craig & Brown 1986; Judge et al. 1997; Landi & Landini 1997; Kashyap & Drake 1998; McIntosh 2000; Weber et al. 2004; Goryaev et al. 2010; Hannah & Kontar 2012). Early on and parallel to these

developments, authors were attentive to estimating the accuracy of the inversions (e.g., Dere 1978), eventually comparing several algorithms (e.g., Fludra & Sylwester 1986).

Due to the intrinsic underconstraint of inverse problems and to the inevitable presence of random and systematic measurement errors, multiple physical solutions consistent with the observations exist, even if mathematical uniqueness and stability can be ensured via, e.g., regularization. It is nevertheless possible to quantify the amount of knowledge, or ignorance, regarding the physical parameter of interest by rigorously defining levels of confidence in the possible solutions or classes of solutions that can explain the observations within the uncertainties. This is a desirable feature for any inversion scheme if it is to be able, for example, to discriminate between or even to define isothermality and multithermality.

In this perspective, we developed a technique to systematically explore the whole space of solutions, in order to determine their respective probabilities and quantify the robustness of the inversion with respect to plasma parameters, and random and systematic errors. We used data simulated with simple DEM forms to systematically scan a wide range of plasma conditions, from isothermal to broadly multithermal, and several inversion hypotheses. Comparing the DEM solutions to the input of the simulations, it is possible to quantify the quality of the inversion. Following this strategy, we are able to completely characterize the statistical properties of the inversion for several parametric DEM distributions. We argue that even though the specifics may vary, the main conclusions concerning the existence of multiple solutions and the ability to distinguish isothermality from multithermality also apply to more generic forms of DEM distributions.

In this first paper, we focus on the response of AIA to isothermal plasmas. The properties of the isothermal inversion thus observed will serve as building blocks for the interpretation of the more complex DEM solutions studied in the second paper (Guennou et al. 2012, hereafter Paper II). Section 2 describes the general methodology and the practical implementation in the case of AIA, including the data simulation, the inversion scheme, the sources of random and systematic errors, and the different DEM distribution models considered. Results for isothermal plasmas are presented and discussed in Section 3. A summary introducing the treatment of more generic DEM forms is given in the conclusion.

## 2. METHODOLOGY

### 2.1. DEM Formalism

Under the assumption that the observed plasma is optically thin, integration along the LOS of collisional emission lines and continua produces an intensity in the spectral band  $b$  of an instrument of

$$I_b = \frac{1}{4\pi} \int_0^\infty R_b(n_e, T_e) n_e^2 ds, \quad (1)$$

where  $R_b(n_e, T_e)$ , the response of the instrument to a unit volume of plasma of electron number density  $n_e$  and temperature  $T_e$ , is given by

$$R_b(n_e, T_e) = \sum_{X,l} S_b(\lambda_l) A_X G_{X,l}(n_e, T_e) + \int_0^\infty S_b(\lambda) G_c(n_e, T_e) d\lambda. \quad (2)$$

The first term of the right member accounts for each spectral line  $l$  of each ionic species  $X$  of abundance  $A_X$ , and the second term represents the contribution of the continua.  $S_b(\lambda)$  is the spectral sensitivity of the band  $b$  of the instrument. The respective contribution functions  $G_{X,l}(n_e, T_e)$  and  $G_c(n_e, T_e)$  of the lines and continua contain the physics of the radiation emission processes (e.g., Mason & Monsignori Fossi 1994) and can be computed using the relevant atomic data. As long as one considers total line intensities, Equations (1) and (2) are generic and apply to imaging telescopes as well as to spectrometers.

Summarizing the original reasoning of Pottasch (1963, 1964), since the function  $R_b(n_e, T_e)$  is generally weakly dependent on the density and is peaked with temperature,  $I_b$  gives a measure of  $\int_p n_e^2 ds$  where the integration is now limited to the portions  $p$  of the LOS where the temperature is such that significant emission is produced. If measurements are available at several wave bands, it is possible to plot  $\int_p n_e^2 ds$  as a function of the bands' peak temperatures. Generalizing this logic into a differential form, and assuming that the element abundances are constant, Equation (1) can be reformulated as

$$I_b = \frac{1}{4\pi} \int_0^{+\infty} R_b(T_e) \xi(T_e) d \log T_e, \quad (3)$$

where  $\xi(T_e) = \overline{n_e^2}(T_e) dp / d \log T_e$  is the DEM that provides a measure of the amount of emitting plasma as a function of temperature.<sup>4</sup> As demonstrated by Craig & Brown (1976),  $\overline{n_e^2}(T_e)$  is the mean square electron density over the regions  $dp$  of the LOS at temperature  $T_e$ , weighted by the inverse of the temperature gradients in these regions. The total emission measure (EM) is obtained by integrating the DEM over the temperature

$$\text{EM} = \int_0^{+\infty} \xi(T_e) d \log T_e = \int_0^\infty n_e^2 ds. \quad (4)$$

Solving the DEM integral equation (3) implies reversing the image acquisition, LOS integration, and photon emission processes to derive the distribution of temperature in the solar corona from observed spectral line intensities. We will now investigate the properties of this inversion.

### 2.2. Probabilistic Interpretation of the DEM Solutions

Let us consider a plasma characterized by a DEM  $\xi^P(T_e)$ . The corresponding intensities observed in  $N_b$  spectral bands are denoted  $I_b^{\text{obs}}(\xi^P)$ . In order to solve the DEM inverse problem—estimating  $\xi^P$  from the observations—one uses a criterion  $C(\xi)$  that defines the distance between the data  $I_b^{\text{obs}}$  and the theoretical intensities  $I_b^{\text{th}}(\xi)$  computed using Equations (2) and (3) for any DEM  $\xi(T_e)$ . By definition the DEM  $\xi^I(T_e)$  solution of the inversion is the one that minimizes this criterion:

$$\xi^I = \arg \min_\xi C(\xi). \quad (5)$$

Since the  $I_b^{\text{obs}}$  values are affected by measurement noises and the  $I_b^{\text{th}}$  values are affected by systematic errors in the calibration and atomic physics, the inversion can yield different solutions

<sup>4</sup> The logarithmic scale is justified by the shape of the contribution functions (see Figure 8). The DEM can also be defined in linear scale as  $\xi(T_e) = \overline{n_e^2}(T_e) dp / dT_e$ . There is a factor  $d \log T_e / dT_e = 1 / \ln 10 T_e$  between the two conventions.

$\xi^I$  of probabilities  $P(\xi^I|\xi^P)$  for a given DEM  $\xi^P$  of the plasma. Bayes' theorem then gives

$$P(\xi^P|\xi^I) = \frac{P(\xi^I|\xi^P)P(\xi^P)}{P(\xi^I)}, \quad (6)$$

which is the conditional probability that the plasma has a DEM  $\xi^P$ , knowing the result  $\xi^I$  of the inversion.  $P(\xi^I) = \int P(\xi^I|\xi^P)P(\xi^P) d\xi^P$  is the total probability of obtaining  $\xi^I$  whatever the  $\xi^P$ . In the Bayesian framework,  $P(\xi^P)$  is called the *prior*. It is uniformly distributed if there is no a priori information on the DEM  $\xi^P$  of the plasma. Conversely, a priori knowledge or assumptions on the plasma are represented by a varying  $P(\xi^P)$ . For example, zero probabilities can be assigned to non-physical solutions.

$P(\xi^P|\xi^I)$  contains all the information that can be obtained from a given set of measurements on the real DEM  $\xi^P$  of the plasma and as such, it is a desirable quantity to evaluate. Indeed, if the DEM is to be used to discriminate between physical models, as it is, for example, in the case in the coronal heating debate, finding a solution that minimizes the criterion is necessary, but it is not sufficient. It is also crucial to be able to determine if other solutions are consistent with the uncertainties, what their respective probabilities are, and how much they differ from each other.

In principle, and without an a priori on the plasma,  $P(\xi^I|\xi^P)$  and thus  $P(\xi^P|\xi^I)$  can be estimated for any minimization scheme using Monte Carlo simulations (Metropolis & Ulam 1949). For each  $\xi^P$ , the  $N_b$  observed  $I_b^{\text{obs}}(\xi^P)$  are simulated using Equations (2) and (3) and adding photon and instrumental noises. Systematic errors are incorporated into the  $I_b^{\text{th}}$  and the resulting criterion is minimized.  $P(\xi^I|\xi^P)$  is then evaluated from the  $N$  solutions  $\xi^I$  corresponding to  $N$  realizations of the random variables. But since several  $\xi^P$  can potentially yield the same  $\xi^I$ , the derivation of  $P(\xi^P|\xi^I)$  from Equation (6) requires us to know  $P(\xi^I)$ , the probability of obtaining  $\xi^I$  whatever  $\xi^P$ . This is generally not possible, for it requires the exploration of an infinite number of plasma DEMs.

This is why DEM inversion research often focuses on the minimization part of the problem,  $P(\xi^P|\xi^I)$  being supposed to be well behaved because of the proper choice of *prior* and the multiplication of passbands or spectral lines. However,  $P(\xi^P|\xi^I)$  can be computed if the DEM  $\xi^P$  of the plasma can be described by a limited number of parameters. In this case, one can scan the whole parameter space and use the Monte Carlo simulations to estimate  $P(\xi^I|\xi^P)$  for all possible  $\xi^P$ . The possibility that multiple  $\xi^P$  values yield an identical inversion solution  $\xi^I$ , which is now being taken into account, one can determine  $P(\xi^I)$  and thus derive  $P(\xi^P|\xi^I)$  from Equation (6).

This limitation of the complexity of the DEMs that can be considered corresponds to adopting a non-uniform *prior*  $P(\xi^P)$ , whereas probabilistic treatments were justly developed with the opposite objective of relaxing such non-physical assumptions (e.g., the method of Kashyap & Drake 1998, based on a Markov Chain Monte Carlo (MCMC) algorithm). But rather than the development of a generic DEM inversion method, our objective is to study the behavior of  $P(\xi^P|\xi^I)$  in controlled experiments. And if the parameterization is properly chosen, the  $\xi^P$  can still represent a variety of plasma conditions, from isothermal to broadly multithermal. In addition, we did not make any assumption on the number and properties of the spectral bands, or on the definition of the criterion, or on the algorithm used to minimize it. The method described to compute  $P(\xi^P|\xi^I)$

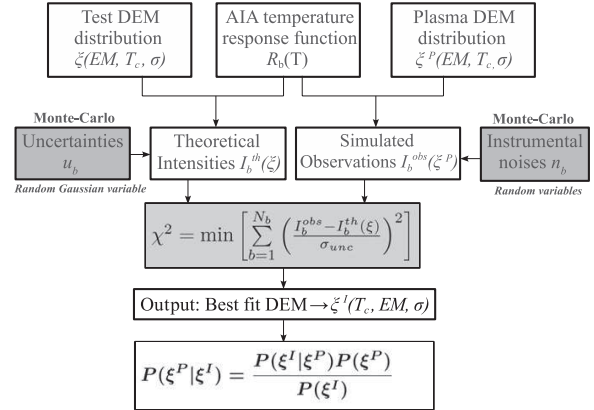


**Figure 1.** Principle of the method used. Reference theoretical intensities  $I_b^0$  are tabulated using CHIANTI for different parameterized DEM functional forms (Dirac, Gaussian, top-hat). A random variable is added to represent the uncertainties on the calibration and atomic physics. For a given plasma DEM  $\xi^P$ , AIA observations are simulated in a similar way. A  $\chi^2$  criterion is minimized to find the DEM  $\xi^I$  that best matches the simulated observations. By scanning the parameters defining  $\xi^P$ , the probabilities  $P(\xi^I|\xi^P)$  and  $P(\xi^P|\xi^I)$  are built from a large number of draws of the random variables. These probabilities and the corresponding distributions of  $\chi^2$  values give a complete characterization of the inversion for the chosen DEM forms.

can therefore be used to characterize any inversion scheme in the range of physical conditions covered by the chosen  $\xi^P$  distributions.

### 2.3. Inversion Method

Devising an efficient way to locate the absolute minimum of the criterion is not trivial. For example, without further assumptions, its definition alone does not guarantee that it has a single minimum, so that iterative algorithms may converge to different local minima depending on the initial guess solution. Furthermore, if the value of the minimum itself is a measure of the goodness of fit, it does not provide information on the robustness of the solution. How well the solution is constrained is instead related to the topography of the minimum and its surroundings; the minimum may be deep or shallow and wide or narrow with respect to the different parameters describing the DEM curve.

The number of DEMs resulting in significantly different sets of intensities within the dynamic range of an instrument is potentially extremely large. However, a systematic mapping of the criterion aimed at revealing its minima and their topography is possible if the search is restricted to a subclass of all possible DEM forms. Indeed, if the DEM is fully determined by a limited number of parameters, one can regularly sample the parameter space and compute once and for all the corresponding theoretical intensities  $I_b^{\text{th}}(\xi)$ . The criterion, i.e., the distance between the  $I_b^{\text{th}}$  and the measured  $I_b^{\text{obs}}$ , is thus computable as a function of the DEM parameters for any given set of observations. It is then trivial to find its absolute minimum and the corresponding DEM solution  $\xi^I$ , or to visualize it as a function of the DEM parameters.

### 2.4. Implementation

The procedure used to compute  $P(\xi^P|\xi^I)$  is summarized in Figure 1. The parametric DEM forms are described in Section 2.4.1. The intensities  $I_b^{\text{obs}}$  observed in  $N_b$  bands are



the sum of average intensities  $I_b^0$  and random perturbations  $n_b$  due to photon shot noise and measurement errors

$$I_b^{\text{obs}} = I_b^0 + n_b. \quad (7)$$

The  $I_b^0$  are equal to the theoretical intensities  $I_b^{\text{th}}$  in the case of a hypothetically perfect knowledge of the instrument calibration and atomic physics. In practice, however, the  $I_b^{\text{th}}$  values are affected by the systematic errors  $s_b$

$$I_b^{\text{th}} = I_b^0 + s_b. \quad (8)$$

Since there is no way of knowing whether the intensities that can be computed from Equations (2) and (3) for any DEM  $\xi$  are overestimated or underestimated, we identify them<sup>5</sup> as the reference theoretical intensities  $I_b^0$ . The distributions of random and systematic errors are discussed in Section 2.4.3. Details of the calculation of the  $I_b^0$  are given in Section 2.4.2. From these, we can either simulate observations  $I_b^{\text{obs}}$  by adding measurement noises  $n_b$  (Equation (7)), or obtain various estimates of the  $I_b^{\text{th}}$  by adding perturbations representing the systematics  $s_b$  (Equation (8)).

The criterion  $C(\xi)$  and the corresponding minimization scheme are described in Section 2.4.4. For any plasma DEM  $\xi^P$ , Monte Carlo realizations of the noises  $n_b$  and systematics  $s_b$  yield several estimates of  $\xi^I$ , from which we compute  $P(\xi^I|\xi^P)$ . Finally,  $P(\xi^P|\xi^I)$  is obtained after scanning all possible plasma DEMs (Section 2.4.5).

#### 2.4.1. DEM Distribution Models

In view of the discussions of Sections 2.2 and 2.3, the  $\xi^P$  and  $\xi^I$  are both constrained to belong to one of the three following classes of DEM distributions defined by two or three parameters:

1. Isothermal:

$$\xi_{\text{iso}}(T_e) = \text{EM} \delta(T_e - T_c), \quad (9)$$

where the DEM is reduced to a Dirac  $\delta$  function centered on the temperature  $T_c$ . EM is the total EM defined by Equation (4).

2. Gaussian in  $\log T_e$ :

$$\xi_{\text{gau}}(T_e) = \text{EM} \mathcal{N}(\log T_e - \log T_c),$$

$$\text{with } \mathcal{N}(x) = \frac{1}{\sigma\sqrt{2\pi}} \exp\left(-\frac{x^2}{2\sigma^2}\right). \quad (10)$$

The plasma is here predominantly distributed around a central temperature  $T_c$  with a width  $\sigma$ .

3. Top-hat in  $\log T_e$ :

$$\xi_{\text{hat}}(T_e) = \text{EM} \Pi(\log T_e - \log T_c),$$

$$\text{with } \Pi(x) = \begin{cases} \frac{1}{\sigma} & \text{if } |x| < \frac{\sigma}{2} \\ 0 & \text{else.} \end{cases} \quad (11)$$

The plasma is uniformly distributed over a width  $\sigma$  around  $T_c$ .

<sup>5</sup> It is also possible to adopt the view that the intensities computed with CHIANTI are one of the possible estimates of the  $I_b^{\text{th}}$ , in which case we obtain the  $I_b^0$  by adding systematic errors. The only difference between the two conventions is the sign of  $s_b$ . The criterion and therefore the results are identical in both cases.

There is no reason for the solar plasma to follow one of these distributions, nor are they the only possible choices. But even though they are simple enough to allow a detailed analysis of the properties of the DEM inversion, they can nonetheless represent a variety of plasma conditions. The conclusions drawn can therefore help us to understand the behavior of more generic DEM forms. Furthermore, since the class of solution DEMs  $\xi^I$  does not have to be the same as that of the plasma DEMs  $\xi^P$ , it is possible to investigate the impact of a wrong assumption on the shape of the DEM. For example, one can compute  $P(\xi^P|\xi^I)$  for isothermal solutions  $\xi^I$  while the plasma DEM  $\xi^P$  is multithermal (see Paper II).

#### 2.4.2. Reference Theoretical Intensities

Equations (2) and (3) are used to compute the reference theoretical intensities  $I_b^0(\xi)$  for any DEM  $\xi$ . They are then used to form both simulated observations and various estimates of the theoretical intensities with Equations (7) and (8).

From Equations (9)–(11), we derive the expressions of these reference intensities as a function of the parameters EM,  $T_c$ , and  $\sigma$  for the three types of DEM distributions.

1. Isothermal:

$$I_b^0(\text{EM}, T_c) = \text{EM} \int_0^{+\infty} R_b(T_e) \delta(T_e - T_c) d \log T_e$$

$$= \text{EM} R_b(T_c) \quad (12)$$

2. Gaussian:

$$I_b^0(\text{EM}, T_c, \sigma) = \text{EM} \int_0^{+\infty} R_b(T_e) \mathcal{N}(\log T_e - \log T_c) d \log T_e$$

$$= \text{EM} (R_b * \mathcal{N})(T_c, \sigma) \quad (13)$$

3. Top-hat:

$$I_b^0(\text{EM}, T_c, \sigma) = \text{EM} \int_0^{+\infty} R_b(T_e) \Pi(\log T_e - \log T_c) d \log T_e$$

$$= \text{EM} (R_b * \Pi)(T_c, \sigma). \quad (14)$$

We note that in all cases, the reference theoretical intensities are equal to the convolution product of the instrument response function  $R_b(T_e)$  by the chosen DEM  $\xi(T_e)$ . The  $I_b^0$  are pre-computed for all possible combinations of the parameters EM,  $T_c$ , and  $\sigma$ . The appropriate range and resolution to be used for each parameter can be determined from plausible plasma properties and by taking into account the instrument characteristics.

The responses  $R_b(T_e)$  of the six AIA coronal bands are computed using Equation (2). The contribution functions  $G(T_e)$  are obtained using version 7.0 of the CHIANTI atomic database (Dere et al. 1997, 2009). We used the CHIANTI ionization balance and the extended coronal abundances. The summation is extended over the 5–50 nm spectral range for all bands. The instrument sensitivity  $S_b(\lambda)$  is obtained as a function of wavelength in units of  $\text{DN cm}^2 \text{ photon}^{-1} \text{ sr}^{-1}$  by calling the function `aia_get_response` provided in the AIA branch of the Interactive Data Language *Solar Software* (SSW) package with the `/DN`, `/area`, and `/full` keywords. This function implements the AIA pre-flight calibration as described in Boerner et al. (2012). Since photon shot noise must be taken into account in the error budget (Section 2.4.3), the  $I_b^0(\xi)$  must be computed for given exposure times and not per second. We used the standard

AIA exposures of 2 s for the 17.1 nm and 19.3 nm bands, and 2.9 s for the others.

The contribution functions are computed using CHIANTI from  $\log(T_e) = 5$  to  $\log(T_e) = 7.5$  in steps of  $0.005 \log(T_e)$ , oversampling the CHIANTI grid by a factor of 10, using cubic spline interpolations. The EM varies over a wide range from  $10^{25} \text{ cm}^{-5}$  to  $10^{33} \text{ cm}^{-5}$  in steps of  $0.04 \log(\text{EM})$ . The DEM width varies linearly in 80 steps from  $\sigma = 0$  to  $\sigma = 0.8 \log(T_e)$ . This choice of sampling leads to pre-computing  $10^7$  groups of six AIA intensities, which represents easily manageable data cubes.

#### 2.4.3. Uncertainties

Uncertainties due to random and systematic errors are at the heart of the problem of the DEM inversion. The two affect the observations and their interpretation in different ways (see, e.g., Taylor 1997). Observations are mostly affected by random errors caused by both Poisson photon shot noise and nearly Gaussian detection noises like thermal and read noise. These noises vary randomly from pixel to pixel and from exposure to exposure. On the other hand, the errors made on the calibration and atomic physics systematically skew the interpretation of all observed intensities by the same amount and in the same direction.

It is possible to realistically simulate in the  $I_b^{\text{obs}}$  the statistical properties of the noises affecting the data. The reference intensities  $I_b^0$  have units of Digital Numbers (DNs). The number of electrons collected in each pixel over the exposure time is obtained by multiplying these values by the gains (in  $e^- \text{ DN}^{-1}$ ) of the detectors' analog-to-digital converters listed in SSW. The number of detected photons is then obtained by dividing the result by the quantum yield of the detector, i.e., the number of photoelectrons produced per interacting photon.<sup>6</sup> These photon intensities are then perturbed by Poisson noise and converted back to photoelectrons. 22  $e^-$  rms of Gaussian CCD read noise (Boerner et al. 2012) are finally added before conversion to DN.

Determining the statistical properties of the systematic errors is more challenging. The tabulated calibration and atomic physics provides a single estimate of the instrument response  $R_b$ , but systematics nonetheless have a probability distribution. Indeed, the calibration is the result of laboratory measurements themselves affected by random and systematic errors. If we could recalibrate the instrument a number of times in different facilities we would obtain a distribution of instrumental sensitivities  $S_b(\lambda)$ , the adopted calibration corresponding to one of them. Likewise, different atomic physics codes will give different estimates of the contribution functions  $G(n_e, T_e)$ , the CHIANTI output being one of them. It is, however, difficult to characterize these two probability distributions. They are generally implicitly assumed to be Gaussian and the adopted values to be the most probable. But the distributions may in fact be uniform, or asymmetric, or biased, etc.

The calibration involves a complex chain of measurements, the uncertainties of which are difficult to track and estimate. After independent radiometric calibrations, comparable EUV instruments on the *Solar and Heliospheric Observatory (SOHO)* were found to agree only within about 25% (Huber et al. 2002).

<sup>6</sup> An approximation of the quantum yield of silicon is given by  $hc/(3.65 q \lambda)$  where 3.65 is the energy in eV required to create an electron hole pair,  $q$  is the elementary charge,  $c$  is the speed of light in vacuum, and  $h$  is Planck's constant. Note that in this calculation we assume that all interacting photons have the same wavelength. However, since the FWHM of the AIA bands is comprised between 0.2 and 1.0 nm, the error made is only a few  $10^{-3}$ .

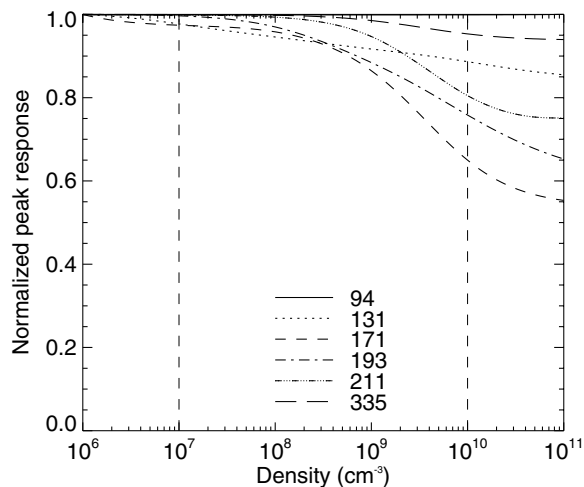


**Figure 2.** Normalized maximum of the response functions  $R_b(T_e, n_e)$  of the six AIA coronal bands as a function of electron number density. Only the 9.4 nm band is independent of the density as assumed in the DEM analysis. The other functions vary by up to 35% in the range of densities plausible in the AIA field of view (dashed vertical lines). This effect induces systematic errors in the DEM inversions.

Subsequent comparisons could not resolve the discrepancies or identify their origin in random errors or biases in the individual calibrations. We can only say that the adopted calibration of every *SOHO* instrument introduces a systematic error in the data analysis but without being able to tell how much and in what direction. It is likely that intercalibration between AIA and other instruments would run into similar limitations.

Errors in the contribution functions are a major contributor to the uncertainties (e.g., Lang et al. 1990; Judge et al. 1997). Since the properties of the known atomic transitions are derived either from measurements or modeling, they are not infinitely accurate. Missing transitions lead to underestimated contributions functions, as is the case for the 9.4 nm channel of AIA (e.g., Aschwanden & Boerner 2011; O'Dwyer et al. 2012; Foster & Testa 2011). The abundances are affected by about 10% uncertainties (Asplund et al. 2009), not taking into account possible local enhancements of high first ionization potential (FIP) elements (Young 2005). These imply that, at least in some cases, the abundances are not constant along the LOS, as assumed in the DEM analysis. The plasma may not be in ionization balance, in which case the CHIANTI calculations of transition rates are not valid. The response functions  $R_b$  of AIA are also not independent from the electron number density, which is one of the assumptions made in deriving the DEM expression from Equations (1) to (3). When using spectrometers, the spectral lines are chosen so that this hypothesis is effectively verified. We plot in Figure 2 the normalized maximum of  $R_b(T_e, n_e)$  versus electron number density. In the AIA FOV,  $n_e$  can vary from about  $10^7 \text{ cm}^{-3}$  in coronal holes at  $1.2 R_\odot$  (e.g., Guhathakurta et al. 1999) to about  $10^{10} \text{ cm}^{-3}$  in dense coronal loops (e.g., Reale 2002). In this range, only the 9.4 nm band (solid line) is completely independent of the density. The response function of all other bands decreases as the density increases, the variation reaching about 35% for the 17.1 nm band (short dashed line). Since the contribution functions have to be computed for a constant electron number density (we chose  $10^9 \text{ cm}^{-3}$ ), they are

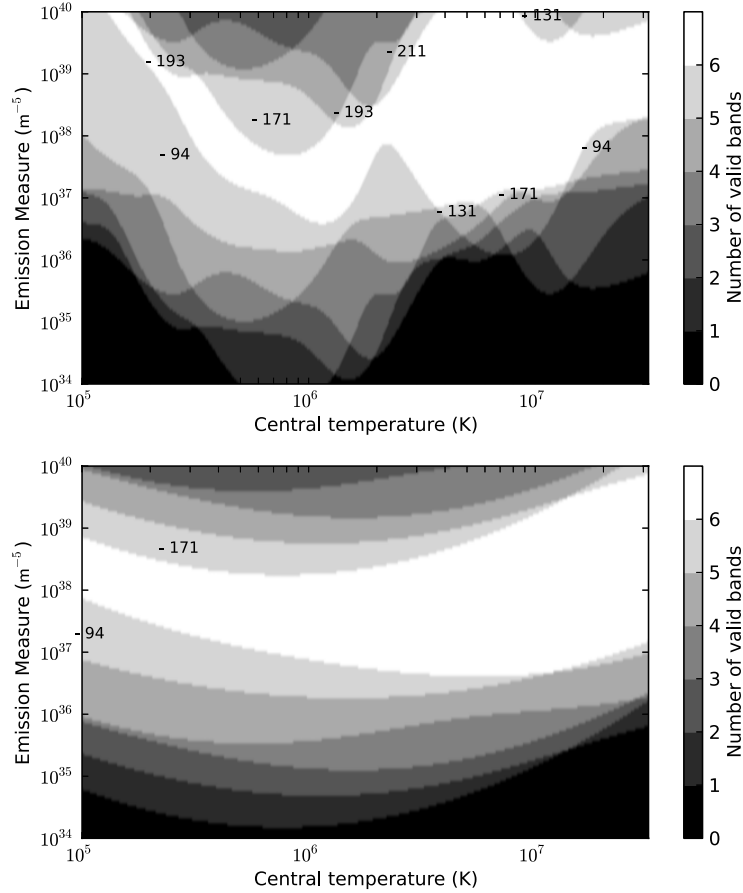


**Figure 3.** Number of AIA bands in which the signal is comprised between 1 DN (detection threshold) and 11,000 DN (saturation) as a function of temperature and emission measure, for standard exposure times. Left: isothermal plasmas; right: Gaussian DEMs with  $\sigma = 0.5 \log(T_e)$ . Only solar structures falling in the white regions produce exploitable signal in all six AIA coronal bands. The regions corresponding to five valid bands are labeled with the wavelength of the missing one. If exposure times were increased, the boundaries of all regions would be shifted toward smaller emission measures. If several images were summed up to overcome saturation, the upper boundaries would be moved upward.

respectively under or overestimated if the observed structures are more or less dense. The impact can be mitigated if one has independent knowledge of the range of densities on the LOS, but it nonetheless represents an additional source of uncertainty compared to using density insensitive spectral lines. Finally, these various sources of uncertainties do not affect all spectral bands by the same amount.

Rigorously estimating the properties of the probability distributions of the systematic errors would thus require a detailed analysis of the calibration process and of the atomic physics data and models, which is beyond the scope of this paper. In these conditions, we make the simplifying assumption that all systematics are Gaussian distributed and unbiased. According to Boerner et al. (2012), uncertainties on the pre-flight instrument calibration are of the order of 25%. This is thus interpreted as a Gaussian probability distribution centered on the tabulated values with a 25% standard deviation. Likewise, we used 25% uncertainty on the atomic physics for all bands, typical of the estimates found in the literature. Calibration and atomic physics uncertainties were added quadratically for a net 35% uncertainty on the response functions  $R_b$ . The  $I_b^{\text{th}}$  values are thus obtained by adding Gaussian random perturbations to the  $I_b^0$ .

#### 2.4.4. Criterion and Minimization

Since instrumental noises and systematic errors are assumed to be Gaussian distributed, we use a least-square criterion

$$C(\xi) = \sum_{b=1}^{N_b} \left( \frac{I_b^{\text{obs}} - I_b^{\text{th}}(\xi)}{\sigma_b^u} \right)^2 \quad (15)$$

normalized to the total standard deviation  $\sigma_b^u$  of the uncertainties in each band.  $\sigma_b^u$  is obtained by summing quadratically the standard deviations of the four individual contributions: photon noise, read noise, calibration, and atomic physics (Section 2.4.3). The value of the minimum of  $C(\xi)$  corresponding to the solution  $\xi^I$  is denoted

$$\chi^2 = \min C(\xi). \quad (16)$$

From Equations (8) and (7), we obtain

$$C(\xi) = \sum_{b=1}^{N_b} \left( \frac{I_b^0(\xi^P) - I_b^0(\xi) + n_b - s_b}{\sigma_b^u} \right)^2. \quad (17)$$

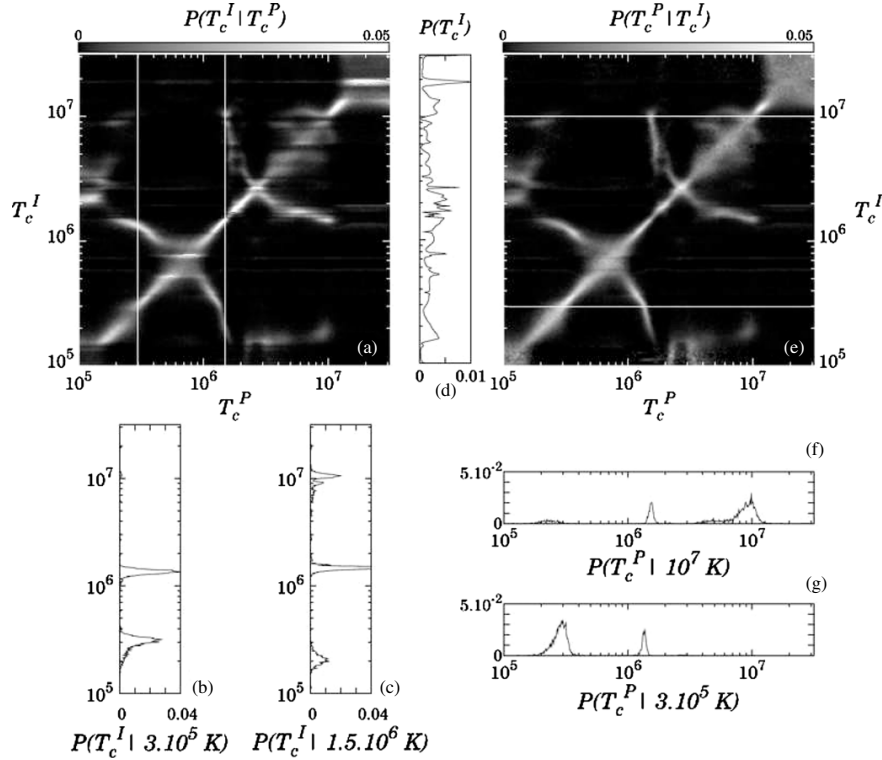


**Figure 4.** Probabilities of the isothermal solutions for observations of an isothermal plasma with three of the AIA coronal bands (17.1, 19.3 and 21.1 nm). (a) reading vertically, conditional probability  $P(T_c^I | T_c^P)$  that the inversion yields  $T_c^I$  for a given plasma temperature  $T_c^P$ . (e) reading horizontally, probability  $P(T_c^P | T_c^I)$  that the plasma has a temperature  $T_c^P$  for an inverted value  $T_c^I$ . (d) is obtained by normalizing (a) to (d) the unconditional probability  $P(T_c^I)$  that the inversion yields  $T_c^I$  whatever the plasma temperature, which is obtained by integrating (a) over  $T_c^P$ . The branches bifurcating from the diagonal reveal the existence of multiple solutions. The probability profiles (b) and (c) show for example that  $3 \times 10^5$  K or  $1.5 \times 10^6$  K plasmas can be measured at  $3 \times 10^5$  K,  $1.5 \times 10^6$  K or  $10^7$  K. Vice versa, the profiles (f) and (g) can be used to properly interpret  $3 \times 10^5$  K and  $10^7$  K inversions as both are also compatible with a  $1.5 \times 10^6$  K plasma. See Section 3.1 for details.

If the family of solutions (Dirac, Gaussian, or top-hat) is identical to that of the plasma DEM  $\xi^P$ , then in the absence of noise  $\chi^2 = 0$  and the solution  $\xi^I$  given by Equation (5) is strictly equal to  $\xi^P$ . However, in the presence of random and systematic errors or if the assumed DEM form differs from that of the observed plasma,  $\chi^2$  is not likely to be zero and the corresponding  $\xi^I$  may be different from  $\xi^P$ , since random fluctuations of  $n_b$  and  $s_b$  can compensate for a difference between  $I_b^0(\xi^P)$  and  $I_b^0(\xi)$ . As discussed in Section 3.3, properly interpreting the value of  $\chi^2$  provides a means of testing the pertinence of a given DEM model.

Folding Equation (12), (13), or (14) into Equation (15), we obtain the expression of  $C(\xi)$  for the corresponding DEM distributions. Given a set of observed intensities and a DEM model, the criterion can therefore be easily computed for all possible combinations of the parameters EM,  $T_c$ , and  $\sigma$  using the  $I_b^0(\xi)$  tabulated as described in Section 2.4.2. Finding its minimum and thus the solution  $\xi^I$  is simplified to the location of the minimum of the  $C(\xi)$  matrix. This minimization scheme is not fast compared to, e.g., iterative gradient algorithms, but it ensures that the absolute minimum of the criterion is found whatever its topography. Furthermore, this operation can be efficiently implemented on the Graphics Processing Units (GPUs) of modern graphics cards by using their Compute Unified Device Architecture (CUDA) capability. We implemented a scheme in which each GPU core is in charge

of computing an element of the  $C(\xi)$  matrix, with all GPU cores running in parallel. The search of the minimum of  $C(\xi)$  is also performed by the GPUs, thus reducing the transfers between GPU to CPU to the values of  $\chi^2$  and  $\xi^I$ .

#### 2.4.5. Monte Carlo Simulations

Restricting  $\xi^P$  and  $\xi^I$  to belong to one of the DEM classes described in Section 2.4.1,  $P(\xi^I | \xi^P)$  and  $P(\xi^P | \xi^I)$  are evaluated from Monte Carlo simulations. For every combination of the two or three parameters defining  $\xi^P$  (the ranges and resolutions given in 2.4.1), 5000 independent realizations of the random and systematic errors are obtained. For each of the corresponding sets of six simulated AIA intensities, the inversion code returns the values of the parameters defining  $\xi^I$  (Equation (5)), corresponding to the absolute minimum of the criterion (Equation (15)). From the resulting 5000  $\xi^I$ , we estimate the conditional probability  $P(\xi^I | \xi^P)$  with a resolution defined by the sampling of the parameters. Integration over  $\xi^P$  gives  $P(\xi^I)$  and using Bayes' theorem we obtain  $P(\xi^P | \xi^I)$ .

### 3. RESULTS: ISOTHERMAL SOLUTION TO ISOTHERMAL PLASMA

In order to understand the fundamental properties of the DEM inversion of the AIA data, we first applied the method to investigate the behavior of the isothermal solutions to simulations

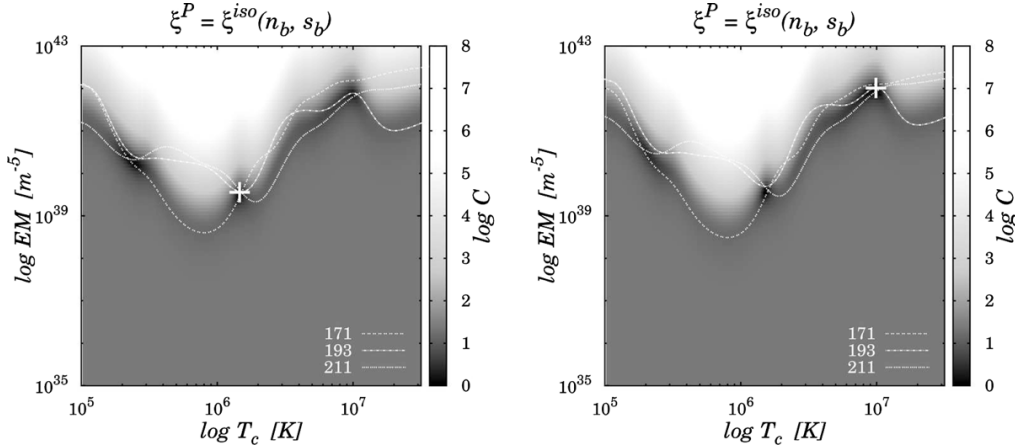


**Figure 5.** Least-squares isothermal criterion (Equation (15)) for a simulated isothermal plasma at  $T_c^P = 1.5 \times 10^6$  K. The two panels correspond to two of the random draws used to build Figure 4. The loci curves for the three components of the criterion are superimposed, and the white plus signs mark the location of its absolute minimum. Both solutions are fully consistent with the simulated data given the uncertainties.

of isothermal plasmas. The electron temperatures and emission measures of the plasmas are denoted  $T_c^P$  and  $EM^P$ , respectively. The corresponding inverted quantities are denoted  $T_c^I$  and  $EM^I$ . The probabilities  $P(T_c^I, EM^I | T_c^P, EM^P)$  and  $P(T_c^P, EM^P | T_c^I, EM^I)$  are stored in matrices of four dimensions. To maximize the clarity of the results, and since the thermal content of the plasma is the main object of DEM analysis, we reduce the number of dimensions by fixing the emission measure of the simulated plasmas to be  $EM^P = 2 \times 10^{29} \text{ cm}^{-5}$ . Furthermore, the probabilities are always presented whatever the emission measure by integrating them over  $EM^I$ , even though  $EM^I$  is of course solved for in the inversion process.

The chosen  $EM^P$  is typical of nonflaring active regions (e.g., Warren et al. 2011). Figure 3 shows as a function of  $T_c^P$  and  $EM^P$  the number of AIA bands in which a plasma produces more than 1 DN (detection threshold) and less than 11,000 DN (saturation). The left panel is for isothermal plasmas, and the right panel is for Gaussian DEMs with  $\sigma^P = 0.5 \log(T_e)$ . At the chosen  $EM^P$ , and since we did not implement the detector saturation in our simulations, we always have an exploitable signal in all six AIA coronal bands, except below a few  $10^5$  K. Conversely, solar structures outside the white areas produce signal only in some of the six bands, unless spatial or temporal summation is used. Therefore, the results presented in the following sections correspond to optimum conditions outside of which the combination of higher noise and possible lower number of valid bands will always lead to weaker constraints on the DEM.

### 3.1. Three Bands: EIT, TRACE, or Low Emission Measures

We first present inversion results using only three bands as an illustration of the situation encountered with previous EUV imaging telescopes like EIT, TRACE, or EUVI. The 17.1 nm and 19.5 nm coronal passbands of EIT and TRACE have direct equivalents in AIA, but the Fe xv 28.4 nm band does not. After comparison of its isothermal response (see, e.g., Figure 9 of Delaboudinière et al. 1995) with those of AIA (Figure 8), we chose the Fe xiv 21.1 nm band as its closest AIA counterpart. The three bands configuration is also similar to having six

bands and a low EM plasma.<sup>7</sup> Indeed, at  $5 \times 10^{26} \text{ m}^{-5}$  and  $1.5 \times 10^6$  K, values typical of coronal loops, only three of the six AIA coronal bands produce more than 1 DN (see Figure 3), the others providing only upper limit constraints to the DEM.

Panel (a) of Figure 4 shows a map of the probability<sup>8</sup>  $P(T_c^I | T_c^P)$ . It is worth noting that, as explained in Section 2.2,  $P(T_c^I)$  and thus  $P(T_c^P | T_c^I)$  could be evaluated only because the limitation to simple parameterized DEM forms allowed the computation of  $P(T_c^I | T_c^P)$ . The plot of  $P(T_c^I)$  (and thus the horizontal structures in panel (a)) shows that some temperature solutions  $T_c^I$  are more probable than others for any plasma temperature  $T_c^P$ . In the case of real observations, this can be misinterpreted as the ubiquitous presence of plasma at the most likely temperatures. This caveat was already analyzed by Weber et al. (2005) in the case of the 19.5–17.3 nm TRACE band ratio and we will discuss it further in Paper II for multithermal plasmas.

Both probability maps exhibit a diagonal from which several branches bifurcate. Below  $2 \times 10^5$  K and above  $10^7$  K the diagonal disappears because, since the bands have little sensitivity in these regions, the signal is dominated by noises and the inversion output is thus independent from the temperature. The general symmetry with respect to the diagonal reflects the equality  $P(T_c^P | T_c^I) = P(T_c^I | T_c^P) / P(T_c^I)$ . The diagonal is formed by the solutions  $T_c^I$  that are close to the input  $T_c^P$ , while the branches correspond to significant deviations from the input. In  $P(T_c^I | T_c^P)$ , these branches imply that two or more solutions  $T_c^I$  can be found for the same plasma temperature  $T_c^P$ . Conversely, reading the  $P(T_c^P | T_c^I)$  image horizontally, a given temperature solution  $T_c^I$  can be coherent with two or more plasma temperatures  $T_c^P$ . The (b) and (c) plots give the probability of the solutions for two plasma temperatures. At  $T_c^P = 3 \times 10^5$  K, the solution may be  $T_c^I = 3 \times 10^5$  K or  $1.2 \times 10^6$  K. At the typical coronal temperature  $T_c^P = 1.5 \times 10^6$  K, the inversion can yield  $1.5 \times 10^6$  K but also  $2 \times 10^5$  K or  $10^7$  K.

<sup>7</sup> For completeness, the plots for all combination of three to six bands are available online at [ftp.ias.u-psud.fr/cguennou/DEM\\_AIA\\_inversion/](http://ftp.ias.u-psud.fr/cguennou/DEM_AIA_inversion/).

<sup>8</sup> Defined as the probability for the solutions to lie between  $\log T_c$  and  $\log T_c + \Delta \log T_c$ .



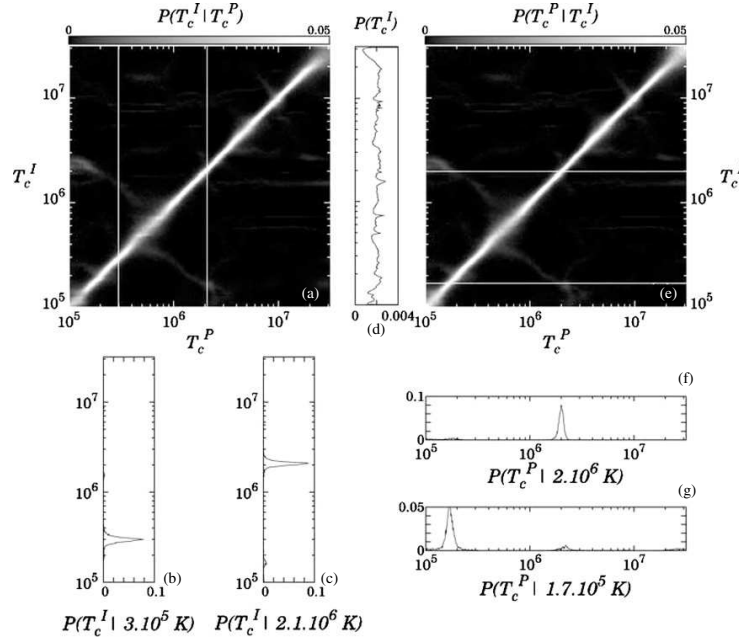


**Figure 6.** Same as Figure 4 for the six AIA coronal bands. The determination of the temperature of the simulated isothermal plasma is now unambiguous. From the width of the diagonal, we deduce the resolution of the isothermal inversion to be about  $0.05 \log(T_c)$ .

It is thus possible to incorrectly conclude that there is the presence of cool or hot coronal plasma while observing an average million-degree corona. This ambiguity has far-reaching implications since the detection of hot plasma is one of the possible signatures of nano-flares (e.g., Cargill 1994; Klimchuk 2006). Since by definition they correspond to the absolute minimum of the criterion, all solutions are fully consistent with the data given the uncertainties. One or more of the multiple solutions can be rejected only based on additional independent a priori information. For example, the high temperature solution corresponds to an EM of  $4 \times 10^{31} \text{ cm}^{-5}$  (right panel of Figure 5), which is extremely high considering the present knowledge of the corona. If no such information is available, however, both low- and high-temperature solutions can still be correctly interpreted as also compatible with a  $1.5 \times 10^6 \text{ K}$  plasma with the aid of the  $P(T_c^P | 3 \times 10^5)$  and  $P(T_c^P | 10^7)$  probability profiles in panels (f) and (g).

The reason for the formation of these branches is illustrated by Figure 5. On both panels, the background image is the value of the criterion  $C(\xi)$  for a  $T_c^P = 1.5 \times 10^6 \text{ K}$  plasma as a function of  $T_c$  and EM. The absolute minimum of the criterion, the arguments of which are the inverted parameters  $T_c^I$  and  $\text{EM}^I$  (Equation (5)), corresponds to the darkest shade of gray and is marked by a white plus sign. The criterion is the sum of three components, one per wave band (Equations (15) and (17)). The three superimposed curves are the loci EM curves for each band  $b$ , i.e., the location of the  $(T_c, \text{EM})$  pairs for which the theoretical intensities  $I_b^{\text{th}}$  equal the measured ones  $I_b^{\text{obs}}$ . Below the loci curves, the criterion is almost flat because at lower EMs the  $I_b^{\text{th}}$  values are much smaller than the constant  $I_b^{\text{obs}}$ . Conversely, the criterion is dominated by the  $I_{\text{th}}$  at high EMs. The darkest shades of gray and thus the minimum of the criterion are located between these two regions. The two panels correspond to two independent realizations of the random and systematic errors.

For each draw, the loci curves are randomly shifted along the EM axis around their average position. In the absence of errors, the three loci curves would cross in a single point at the plasma temperature  $T_c^P$ , giving a criterion strictly equal to zero. In the left panel, with random and systematic errors included, they do not intersect at a single point but the non-zero absolute minimum of  $C$ , where they are the closest together, is around  $T_c^P$ . However, the criterion has two other local minima, around  $2 \times 10^5 \text{ K}$  and around  $10^7 \text{ K}$ , where two or three of the loci curves also bundle up. In the right panel, a different random draw shifts the curves closest together around the high temperature local minimum that thus becomes the new absolute minimum. For this  $1.5 \times 10^6 \text{ K}$  plasma, the inversion thus yields solutions randomly located around the several local minima with respective probabilities given by the profile of Figure 4(c). When scanning the plasma temperatures, the positions of the minima vary, thus building the branches in the probability maps. In addition, depending on their location the minima can be more or less extended along one or the other axes, which results in a varying dispersion around the most probable solutions.

Systematic errors are simulated with random variables while they are in fact identical for all measurements. Thus, the computed  $P(T_c^I | T_c^P)$  does not give the probability of solutions  $T_c^I$  for the practical estimates of the calibration and atomic physics. In reality the output of the inversion is biased toward one or the other of the multiple solutions, but we do not know whether the calibration and atomic physics are under- or overestimated. Therefore, in order to deduce the probability that the plasma has a temperature  $T_c^P$  from an inverted temperature  $T_c^I$ , we must account for the probabilities of the systematics as defined in Section 2.4.3. The randomization samples their distribution, which ensures that the estimated  $P(T_c^P | T_c^I)$  are the probabilities relevant for interpreting  $T_c^I$ .

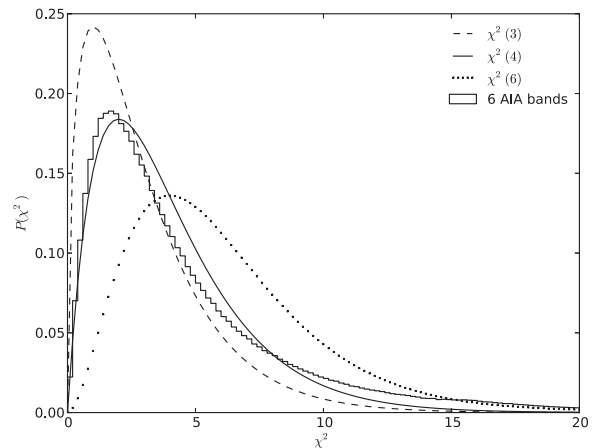
### 3.2. Six Bands: AIA

Figure 6 is the same as Figure 4, but now including the six AIA coronal bands in the analysis. Some secondary solutions persist at low probabilities, but compared to the three bands case, most of the solutions are now concentrated on the diagonal. This illustrates that the robustness of the inversion process increases with the number of bands or spectral lines. Comparison with Figure 4 quantifies the improvement brought by AIA over previous instruments. Neglecting the low probability solutions, if independent a priori knowledge justifies the isothermal hypothesis, the six AIA bands thus provide an unambiguous determination of the plasma temperature. The temperature resolution of the inversion can be estimated from the FWHM of the diagonal. It varies over the temperature range between 0.03 and 0.11  $\log T_c^P$ . It is of course modified if we assumed different uncertainties on the calibration and atomic physics from the ones chosen in Section 2.4.3. We tested the sensitivity of the temperature resolution to the level of uncertainty,  $\sigma_b^u$ , from 10% to 55%. The higher the uncertainty, the lower the temperature resolution and the more probable the secondary solutions.<sup>9</sup> For an estimated temperature  $T_c^I$  of 1 MK, the temperature resolution of the inversion varies between 0.02 for 10% error and 0.08  $\log T_c^P$  for 55% error. In the worst case, for 55% errors, the temperature resolution decreases to 0.2  $\log T_c^P$  for the temperature interval between 0.5 and 0.9 MK. At 1 MK, the resolution is proportional to the uncertainty level with a coefficient of 0.15 ( $\Delta T_c^P \sim 0.15 \sigma_b^u$ ).

Since by definition our method always finds the absolute minimum of the least-square criterion of Equation (15), the derived temperature resolution is an intrinsic property of the data and not of the inversion scheme. It is the result of the combination of the random and systematic errors and the shapes of the contribution functions. Its value is directly comparable to the findings of Landi et al. (2011). Those authors showed that the temperature resolution of the MCMC code of Kashyap & Drake (1998) applied to isothermal plasmas is 0.05  $\log T$ . Their tests were made on simulated observations of a  $10^6$  K plasma in 45 isolated spectral lines with 20% random errors. Assuming that the MCMC method does converge toward solutions consistent with the limitations of the data, the fact that the temperature resolution is comparable for six AIA bands and 45 spectral lines suggests that, in the isothermal case, it is driven by the uncertainty level rather than the number of observables. This conclusion is consistent with the isothermal limit of Figure 6 of Landi & Klimchuk (2010).

### 3.3. Residuals and Goodness of Fit Test

The probability maps presented in the above sections are valid for a given hypothesis on the plasma DEM distribution, but they would be useless without a test of its validity. The pertinence of the DEM model chosen to interpret the observations can be assessed by analyzing the distribution of the sum of squared residuals defined by Equations (15) and (16). If applying our inversion scheme to real data, we could compare the resulting residuals to the distribution derived from simulations for a given DEM model and thus quantify the probability that the data are consistent with the working hypothesis (e.g., isothermal or Gaussian).



**Figure 7.** Observed distribution of the sum of the squared residuals (solid histogram) differs somewhat from the expected four-degree  $\chi^2$  distribution (solid curve). It is slightly shifted toward a three-degree (dashed curve), which can be explained by a small correlation between the six AIA coronal bands.

The solid-line histogram of Figure 7 shows the distribution of  $\chi^2$  values corresponding to the plots of Figure 6. The distribution is close to a four-degree  $\chi^2$  distribution (solid curve) although not a perfect match, with a peak shifted to the left and an enhanced wing. The most probable value of the squared residuals is  $\sim 1.73$  and 95% of them are comprised between 0 and 15. Whatever the actual plasma DEM, any inversion made with the isothermal hypothesis and yielding a  $\chi^2$  value in this range can thus be considered consistent with an isothermal plasma given the uncertainties. This isothermal test is similar to that recommended by Landi & Klimchuk (2010), identifying our  $\chi^2$  with their  $F_{\min}$  and our maximum acceptable  $\chi^2$  with their  $\Delta F$ . This does not imply, however, that isothermality is the only or the best possible interpretation of the data because different DEMs can produce similar  $\chi^2$  values. The discrimination between DEM models will be discussed in Paper II.

The properties of the empirical distribution of squared residuals can be explained as follows. Since we simulated observations of a purely isothermal plasma, an isothermal model can always represent the data. Without errors, there would always be one unique couple  $(T_c^I, EM^I)$  corresponding to six intensities perfectly matching the six AIA observations, thus giving zero residuals. With errors, if we forced the solution  $(T_c^I, EM^I)$  to be the input  $(T_c^P, EM^P)$ , the summed squared residuals resulting from a number of random draws should have by definition the probability density function (PDF) of a six-degree  $\chi^2$  distribution (dotted curve of Figure 7) because we have six independent values of  $I_b^{\text{obs}} - I_b^{\text{th}}$  and we normalized the residuals to the standard deviation  $\sigma_b^u$  of the uncertainties. But since we solve for two parameters  $(T_c^I, EM^I)$  by performing a least-squares minimization at each realization of the errors, the solution is not exactly the input  $(T_c^P, EM^P)$  and we should expect a PDF with two degrees of freedom less (dashed curve). Instead of being a pure four-degree, the observed distribution is slightly shifted toward a three-degree because of two factors. First, the errors are a combination of Poisson photon noise and Gaussian read noise, while the  $\chi^2$  distribution is defined for standard normal random variables. Second, as discussed below, the six residuals are not completely independent.

<sup>9</sup> The corresponding probability maps are available online at [ftp.ias.u-psud.fr/guennou/DEM\\_AIA\\_inversion/](http://ftp.ias.u-psud.fr/guennou/DEM_AIA_inversion/).

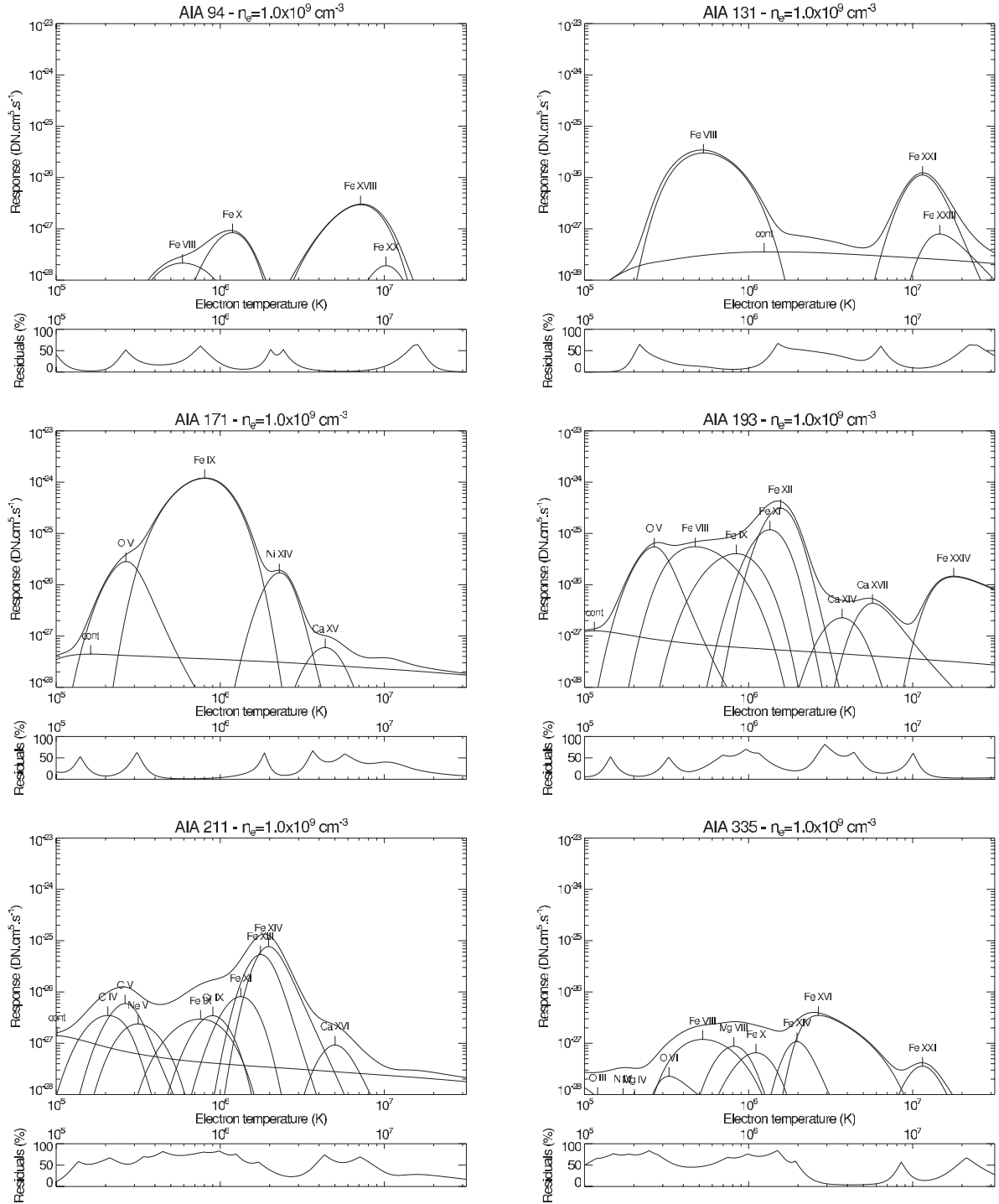


**Figure 8.** Isothermal response of the six AIA coronal bands between  $10^5$  and  $3 \times 10^7$  K. For each band, the thick curve is the total response and the thin curves are the partial responses for the ions that contribute the most in at least one temperature. The fraction of the total response accounted for by those dominant ions is shown below each main plot. Computations are for an electron number density of  $10^9 \text{ cm}^{-3}$ .



Figure 8 shows the response functions  $R_b(T_e)$  of the AIA bands to isothermal plasmas with electron temperatures from  $10^5$  to  $3 \times 10^7$  K for a constant electron number density of  $10^9 \text{ cm}^{-3}$ . For each band, the thick curve is the total response, and the labeled thin curves are the partial responses for the ions that contribute the most for at least one temperature. The fraction of the total response not accounted for by those dominant ions is shown below each main plot. Ionization stages common to several bands are found across the whole range of temperatures. O v dominates the response at  $2.5 \times 10^5$  K in the 17.1 nm, 19.3 nm, and 21.1 nm bands. Around 1 MK, Fe ix is found in the 17.1 nm, 19.3 nm, and 21.1 nm responses, and Fe x contributes to the 94 nm, 21.1 nm, and 33.5 nm bands. At 2 MK, Fe xiv is common to the 21.1 nm and 33.5 nm bands. This is consistent with the analysis of the AIA bands by O'Dwyer et al. (2010). Because of this redundancy, the response functions tend to have similar shapes in the regions of overlap, resulting in a correlation between the residuals.

#### 4. SUMMARY AND CONCLUSIONS

By restricting the solutions to functional forms described by a limited number of parameters, we obtained a complete statistical characterization of the DEM inversion. Even though they are not expected to accurately describe real coronal properties, these simple DEM distributions can nonetheless model a wide range of plasma conditions. The results presented in this series of papers can thus be fruitfully used to demonstrate many important properties and guide the interpretation of the output of generic DEM inversion codes. We illustrated the method by applying it to the six coronal bands of the AIA telescope. In this first paper, we limited ourselves to isothermal plasmas and isothermal solutions.

The case presented in Section 3.1 demonstrates the existence of multiple solutions if the number of bands is limited either by the design of the instrument or by a lack of signal. However, since our method provides the respective probabilities of the multiple solutions, it is possible to properly interpret the solutions as compatible with several plasma temperatures. Even if some of these properties have been illustrated in case studies, we provide here a systematic analysis of a wide range of plasma parameters. The computed distribution of squared residuals can be used to test the coherence of real AIA data with the isothermal hypothesis. This type of analysis can also help to determine the optimum data acquisition parameters for AIA (e.g., spatial binning and exposure time), ensuring that no secondary solution is present. In Section 3.2, we showed that, with enough signal, the six AIA coronal bands provide a robust reconstruction of isothermal plasmas with a temperature resolution obtained between 0.03 and 0.11  $\log T_e$ . The comparison with the three-band case quantifies the improvement brought by the new generation of instruments. The same method can be applied to other instruments with different response functions and different numbers of bands or spectral lines. This naturally requires the computation of the corresponding probability matrices and distribution of residuals.

The temperature resolution, and more generally the details of the probability matrices presented in Sections 3.1 and 3.2, depend on the amplitude and distribution of the random and systematic errors. We found the resolution to be proportional to the uncertainty level (at 1 MK,  $\Delta T_c^P \sim 0.15 \sigma_b^P$ ). We simulated plasmas with high EMs typical of active regions. Depending on the temperature, either the photon noise or the uncertainties on the calibration and atomic physics dominate. The illustrated

properties of the inversion, from the multiplicity of solutions to the temperature resolution, are thus driven by both random systematic errors. While the photon noise can be reduced by increasing the exposure time or binning the data, reducing the systematics requires better atomic data and photometric calibration, which is not trivial.


S.P. acknowledges the support from the Belgian Federal Science Policy Office through the international cooperation programs and the ESA-PRODEX program and the support of the Institut d'Astrophysique Spatiale (IAS). F.A. acknowledges the support of the Royal Observatory of Belgium. The authors thank J. Klimchuk for fruitful discussions and comments.

#### REFERENCES

- Aschwanden, M. J., & Boerner, P. 2011, *ApJ*, **732**, 81  
 Asplund, M., Grevesse, N., Sauval, A. J., & Scott, P. 2009, *ARA&A*, **47**, 4816  
 Boerner, P., Edwards, C., Lemen, J., et al. 2012, *Sol. Phys.*, **275**, 41  
 Brosius, J. W., Rabin, D. M., Thomas, R. J., & Landi, E. 2008, *ApJ*, **677**, 781  
 Brown, J. C., Dwivedi, B. N., Sweet, P. A., & Almléaky, Y. M. 1991, *A&A*, **249**, 277  
 Cargill, P. J. 1994, *ApJ*, **422**, 381  
 Craig, I. J. D., & Brown, J. C. 1976, *A&A*, **49**, 239  
 Craig, I. J. D., & Brown, J. C. 1986, *Inverse Problems in Astronomy: A Guide to Inversion Strategies for Remotely Sensed Data*, SERC (Bristol: Adam Hilger)  
 Del Zanna, G., Bromage, B. J. I., & Mason, H. E. 2003, *A&A*, **398**, 743  
 Delaboudinière, J.-P., Artzner, G. E., Brunaud, J., et al. 1995, *Sol. Phys.*, **162**, 291  
 Dere, K. P. 1978, *A&A*, **70**, 439  
 Dere, K. P., Landi, E., Mason, H. E., Monsignori Fossi, B. C., & Young, P. R. 1997, *A&AS*, **125**, 149  
 Dere, K. P., Landi, E., Young, P. R., et al. 2009, *A&A*, **498**, 915  
 Fludra, A., & Sylwester, J. 1986, *Sol. Phys.*, **105**, 323  
 Foster, A. R., & Testa, P. 2011, *ApJ*, **740**, L52  
 Golub, L., Deluca, E., Austin, G., et al. 2007, *Sol. Phys.*, **243**, 63  
 Goryaev, F. F., Parenti, S., Urnov, A. M., et al. 2010, *A&A*, **523**, A44  
 Guennou, C., Auchère, F., Soubrié, E., et al. 2012, *ApJS*, **203**, 26 (Paper II)  
 Guhathakurta, M., Fludra, A., Gibson, S. E., Biesecker, D., & Fisher, R. R. 1999, *J. Geophys. Res.*, **104**, 9801  
 Hahn, M., Landi, E., & Savin, D. W. 2011, *ApJ*, **736**, 101  
 Handy, B. N., Acton, L. W., Kankelborg, C. C., et al. 1999, *Sol. Phys.*, **187**, 229  
 Hannah, I. G., & Kontar, E. P. 2012, *A&A*, **539**, A146  
 Huber, M. C. E., Pauluhn, A., & von Steiger, R. 2002, in *Proc. SOHO 11 Symp. From Solar Min to Max: Half a Solar Cycle with SOHO*, ed. A. Wilson (ESA SP-508; Noordwijk: ESA), 213  
 Jefferies, J. T., Orrall, F. Q., & Zirker, J. B. 1972, *Sol. Phys.*, **22**, 307  
 Jordan, C. 1976, *Phil. Trans. R. Soc.*, **281**, 391  
 Judge, P. G., Hubeny, V., & Brown, J. C. 1997, *ApJ*, **475**, 275  
 Kashyap, V., & Drake, J. J. 1998, *ApJ*, **503**, 450  
 Klimchuk, J. A. 2006, *Sol. Phys.*, **234**, 41  
 Landi, E., & Klimchuk, J. A. 2010, *ApJ*, **723**, 320  
 Landi, E., & Landini, M. 1997, *A&A*, **327**, 1230  
 Landi, E., & Landini, M. 1998, *A&A*, **340**, 265  
 Landi, E., Reale, F., & Testa, P. 2012, *A&A*, **538**, A111  
 Lang, J., McWhirter, R. W. P., & Mason, H. E. 1990, *Sol. Phys.*, **129**, 31  
 Lemen, J. R., Title, A. M., Akin, D. J., et al. 2012, *Sol. Phys.*, **275**, 17  
 Martinez-Sykora, J., De Pontieu, B., Testa, P., & Hansteen, V. 2011, *ApJ*, **743**, 23  
 Mason, H. E., & Monsignori Fossi, B. C. 1994, *A&AR*, **6**, 123  
 Metropolis, N., & Ulam, S. 1949, *J. Am. Stat. Assoc.*, **44**, 335  
 McIntosh, S. W. 2000, *ApJ*, **533**, 1043  
 O'Dwyer, B., Del Zanna, G., Badnell, N. R., Mason, H. E., & Storey, P. J. 2012, *A&A*, **537**, A22  
 O'Dwyer, B., Del Zanna, G., Mason, H. E., Weber, M. A., & Tripathi, D. 2010, *A&A*, **521**, A21  
 Parenti, S., Bromage, B. J. I., Poletto, G., et al. 2000, *A&A*, **363**, 800  
 Parenti, S., & Vial, J.-C. 2007, *A&A*, **469**, 1109  
 Pottasch, S. R. 1963, *ApJ*, **137**, 945  
 Pottasch, S. R. 1964, *Space Sci. Rev.*, **3**, 816  
 Reale, F. 2002, *ApJ*, **580**, 566  
 Reale, F. 2010, *Living Rev. Sol. Phys.*, **7**, 5  
 Reale, F., Testa, P., Klimchuk, J., & Parenti, S. 2009, *ApJ*, **698**, 756

- Sanz-Forcada, J., Brickhouse, N. S., & Dupree, A. K. 2003, *ApJS*, **145**, 147
- Susino, R., Lanzafame, A. C., Lanza, A. F., & Spadaro, D. 2010, *ApJ*, **709**, 499
- Taylor, J. 1997, *Introduction to Error Analysis: The Study of Uncertainties in Physical Measurements* (2nd ed.; New York: Univ. Science Books)
- Testa, P., De Pontieu, B., Martinez-Sykora, J., Hansteen, V., & Carlsson, M. 2012, *ApJ*, **758**, 54
- Warren, H. P., Brooks, D. H., & Winebarger, A. R. 2011, *ApJ*, **734**, 90
- Weber, M. A., DeLuca, E. E., Golub, L., & Sette, A. L. 2004, in *IAU Symp. 223, Multi-Wavelength Investigations of Solar Activity*, ed. A. V. Stepanov, E. E. Benevolenskaya, & A. G. Kosovichev (Cambridge: Cambridge Univ. Press), 321
- Weber, M. A., Schmelz, J. T., DeLuca, E. E., & Roames, J. K. 2005, *ApJ*, **635**, L101
- Wiik, J. E., Dere, K., & Schmieder, B. 1993, *A&A*, **273**, 267
- Winebarger, A. R., Schmelz, J. T., Warren, H. P., Saar, S. H., & Kashyap, V. L. 2011, *ApJ*, **740**, 2
- Withbroe, G. L. 1975, *Sol. Phys.*, **45**, 301
- Young, P. R. 2005, *A&A*, **439**, 361

---



## On the accuracy of the Differential Emission Measure diagnostics of solar plasmas. Application to *SDO/AIA*. II. Multithermal Plasmas

### C.1

---

#### **Résumé**

Le formalisme de la Mesure d'Émission Différentielle (DEM) est l'un des outils les plus utilisés pour l'étude des atmosphères stellaires. Due à la nature inverse du problème, il existe plusieurs limitations, engendrées par les erreurs systématiques et aléatoires. Dans cette série d'articles, nous présentons une analyse de la robustesse de l'inversion de données *SDO/AIA*. De cette manière, on caractérise complètement l'inversion de DEM et ses propriétés statistiques, fournissant ainsi toutes les solutions compatibles avec un ensemble de données et les incertitudes associées, ainsi qu'un test concernant la compatibilité du modèle de DEM supposé. Tandis que l'article I se concentrait sur les plasmas isothermes, on considère maintenant des plasmas multithermes en analysant le comportement des solutions multithermes et isothermes. L'ambiguïté existante entre erreurs et multithermalité limite fondamentalement la résolution de l'inversion. On montre par exemple que si le plasma est multitherme, les solutions isothermes et multithermes sont biaisées vers des solutions particulières, autour de 1MK. Ce comportement est vrai quelque soit la valeur des résidus, conduisant donc à une interprétation erronée sur le plasma observé. De nouveaux outils sont ici proposés pour identifier et quantifier ces dégénérescences possibles des solutions, permettant ainsi de faciliter l'interprétation de l'inversion de DEM.

### C.2

---

**Article publié dans *The Astrophysical Journal***

ON THE ACCURACY OF THE DIFFERENTIAL EMISSION MEASURE DIAGNOSTICS OF SOLAR PLASMAS. APPLICATION TO *SDO*/AIA. II. MULTITHERMAL PLASMASC. GUENNOU<sup>1</sup>, F. AUCHÈRE<sup>1</sup>, E. SOUBRIÉ<sup>1</sup>, K. BOCCHIALINI<sup>1</sup>, S. PARENTI<sup>2</sup>, AND N. BARBEY<sup>3</sup><sup>1</sup> Institut d'Astrophysique Spatiale, Bâtiment 121, CNRS/Université Paris-Sud, UMR 8617, F-91405 Orsay, France; [chloe.guennou@ias.u-psud.fr](mailto:chloe.guennou@ias.u-psud.fr)<sup>2</sup> Royal Observatory of Belgium, 3 Avenue Circulaire, B-1180 Bruxelles, Belgium<sup>3</sup> SAp/Irfu/DSM/CEA, Centre d'études de Saclay, Orme des Merisiers, Bâtiment 709, F-91191 Gif sur Yvette, France

Received 2012 June 18; accepted 2012 October 5; published 2012 November 21

## ABSTRACT

Differential emission measure (DEM) analysis is one of the most used diagnostic tools for solar and stellar coronae. Being an inverse problem, it has limitations due to the presence of random and systematic errors. We present in this series of papers an analysis of the robustness of the inversion in the case of *SDO*/AIA observations. We completely characterize the DEM inversion and its statistical properties, providing all the solutions consistent with the data along with their associated probabilities, and a test of the suitability of the assumed DEM model. While Paper I focused on isothermal conditions, we now consider multithermal plasmas and investigate both isothermal and multithermal solutions. We demonstrate how the ambiguity between noises and multithermality fundamentally limits the temperature resolution of the inversion. We show that if the observed plasma is multithermal, isothermal solutions tend to cluster on a constant temperature whatever the number of passbands or spectral lines. The multithermal solutions are also found to be biased toward near-isothermal solutions around 1 MK. This is true even if the residuals support the chosen DEM model, possibly leading to erroneous conclusions on the observed plasma. We propose tools for identifying and quantifying the possible degeneracy of solutions, thus helping the interpretation of DEM inversion.

*Key words:* plasmas – Sun: corona – Sun: UV radiation

## 1. INTRODUCTION

A convenient approach for studying the thermal structure of the solar and stellar outer atmospheres is the differential emission measure (DEM) formalism. The DEM  $\xi(T_e)$  is a measure of the amount of emitting plasma along the line of sight (LOS) as a function of the electron temperature  $T_e$ . However, the intrinsic difficulties involved in this inverse problem lead to many complications in its inference, making its interpretation ambiguous. The central point of this series of papers is to provide new tools for systematically and completely characterizing the DEM inversions and assisting the DEM interpretation. Using the technique developed for this purpose, exhaustively described in Guennou et al. (2012, hereafter Paper I), it is possible to determine and to compare the DEM diagnostic capabilities of given instruments. With only three bands, the previous generation of imaging telescopes was shown not to be well suited for DEM analysis (e.g., Schmelz et al. 2009). The situation has changed with the availability of new multi-band instruments such as the Atmospheric Imaging Assembly (AIA) telescope (Lemen et al. 2012) on board the *Solar Dynamics Observatory*. Applying our technique to AIA, we show the increased robustness of the inversion for isothermal plasmas, but we also found intrinsic biases if the observed plasma is multithermal.

Using the notation of Paper I, the DEM is defined as

$$\xi(T_e) = \overline{n_e^2}(T_e) dp/d(\log T_e), \quad (1)$$

where  $\overline{n_e^2}$  is the square electron density averaged over the portions  $dp$  of the LOS at temperature  $T_e$  (Craig & Brown 1976). The observed intensity in the spectral band  $b$  of an instrument can be expressed as a function of the DEM  $\xi$  as follows:

$$I_b = \frac{1}{4\pi} \int_0^{+\infty} R_b(n_e, T_e) \xi(T_e) d \log T_e. \quad (2)$$

Details and references about the DEM formalism can be found in Paper I. Given a set of observations in  $N$  different bands, the DEM can in principle be inferred by reversing the image acquisition process described by Equation (2). However, solving for the DEM has proved to be a considerable challenge. The complications involved in its derivation are one of the reasons for controversial results regarding the thermal structure of the corona. For example, the DEM is one of the methods used to derive the still-debated physical properties of plumes (Wilhelm et al. 2011). Also, while heating models predict different thermal structures for coronal loops depending on the processes involved (e.g., Klimchuk 2006; Reale 2010), DEM analyses have provided ambiguous answers (Schmelz et al. 2009). Several studies (Feldman et al. 1998; Warren 1999; Landi & Feldman 2008) suggest the ubiquitous presence of isothermal plasma in the quiet corona. If confirmed, these results would challenge many theoretical models, but the reliability of the temperature diagnostics used has been questioned (e.g., Landi et al. 2012). Part of this is due to technical issues, such as the difficulty of subtracting the background emission (Terzo & Reale 2010; Aschwanden et al. 2008) or the possible spatial and temporal mismatch of the structures observed in different bands and/or different instruments. But the fundamental limitations of the DEM inversion clearly play a role.

Despite the many proposed inversion schemes, rigorously estimating levels of confidence in the various possible solutions given the uncertainty remains a major difficulty. In this work, we propose a strategy for exploring the whole parameter space, detecting the presence of secondary solutions, and computing their respective probabilities. We illustrate the method by characterizing the inversion of simulated observations of the AIA telescope. This approach allows us to quantify the robustness of the inversion by comparing the inverted DEM to the input of the AIA simulations. The main drawback is the limitation to simple DEM forms (i.e., described by a small number of

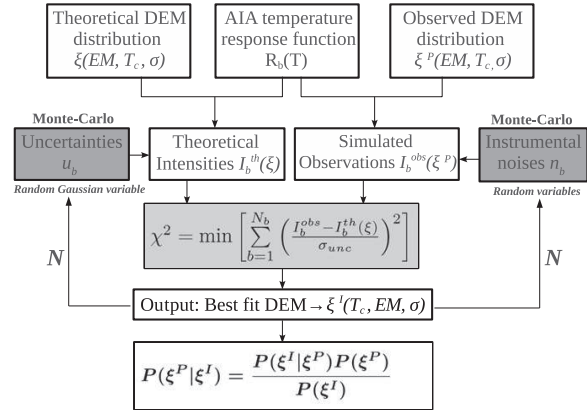


**Figure 1.** Summary of the technique used in this work. The AIA temperature response functions are computed using CHIANTI version 7.0. The simulated observations  $I_b^{\text{obs}}$  are calculated assuming a simple DEM model  $\xi^P$  (isothermal, Gaussian, or top-hat), and adding the instrumental random perturbations and systematic errors. The theoretical intensities  $I_b^{\text{th}}$  are computed assuming a DEM model  $\xi$ , for a large range of parameters. The inverted DEM  $\xi^I$  is evaluated by least-squares minimization of the distance between the theoretical intensities and the simulated observations. Using a Monte Carlo scheme,  $N$  realizations of the random and systematic errors  $n_b$  and  $s_b$  are computed. For a given set of parameters  $(EM^P, T_c^P, \sigma^P)$  of the plasma DEM  $\xi^P$ , the quantity  $P(\xi^I | \xi^P)$  is then evaluated. The probability  $P(\xi^P | \xi^I)$  is then derived using Bayes' theorem.

parameters), but the results provide important insights into the properties of more generic DEM inversions. The method can also easily be applied to any instrument, broadband imagers and spectrometers alike.

Paper I was dedicated to the analysis of isothermal plasmas, and showed the existence of multiple solutions in the case of a limited number of bands. Nevertheless, the statistical method developed in this work (which provides the respective probabilities of each secondary solution), enables us to properly interpret the solutions as consistent with several plasma temperatures. The use of the six AIA coronal bands was shown to increase the thermal diagnostic capabilities, providing a robust reconstruction of isothermal plasmas. The detailed analysis of the squared residuals showed that the DEM complexity is limited by the redundancy of information between the bands.

We now generalize the method of DEM models able to describe a great variety of plasma conditions, from isothermal to broadly multithermal. A summary of the technique is given in Figure 1 and its implementation is exhaustively described in Paper I. The core of our method resides in the probabilistic interpretation of the DEM solutions. The DEM  $\xi^I$  solution of the inversion is the one that minimizes a criterion  $C(\xi)$  defined as the distance between the intensities  $I_b^{\text{obs}}$  observed in  $N_b$  bands and the theoretical ones,  $I_b^{\text{th}}$ . We write

$$C(\xi) = \sum_{b=1}^{N_b} \left( \frac{I_b^{\text{obs}}(\xi^P) - I_b^{\text{th}}(\xi)}{\sigma_b^u} \right)^2 \quad (3)$$

$$\xi^I = \arg \min_{\xi} C(\xi)$$

$$\chi^2 = \min C(\xi),$$

where  $\sigma_b^u$  is the standard deviation of the uncertainties and  $\chi^2$  represents the residuals. Using Monte Carlo simulations of the systematic and random errors, we compute  $P(\xi^I | \xi^P)$ , the

conditional probability to obtain a DEM  $\xi^I$  knowing the plasma DEM  $\xi^P$ . Both types of errors are modeled as Gaussian random variables with a 25% standard deviation (see Section 2.3.3 of Paper I). Then, using Bayes' theorem we obtain  $P(\xi^P | \xi^I)$ , the probability that the plasma has a DEM  $\xi^P$  given the inverted DEM  $\xi^I$ . Using this latter quantity, it is possible to identify the range or multiple ranges of solutions consistent with a set of observations. Therefore, even if it is not possible to alleviate the degeneracy of the solutions, it is at least possible to notice and to quantify them. But the computation of the probability  $P(\xi^P | \xi^I)$  is practical only if the space of the solutions is limited. We therefore restrict the possible solutions to simple forms described by a small number of parameters: Dirac delta function, top-hat, and Gaussian. We thus do not propose a generic inversion algorithm, but using this approach, we were able to completely characterize the behavior of the inversion in well-controlled experiments.

All the results presented in the present paper concern multithermal plasmas. In Section 2, we analyze the properties of the isothermal solutions in order to determine to what extent it is possible to discriminate between isothermal and multithermal plasmas. Section 3 is then dedicated to the general case of multithermal inversions. The results are summarized and discussed in Section 4.

## 2. ISOTHERMAL SOLUTIONS

As already mentioned, a recurring question is that of the isothermality of solar plasmas. The EM loci technique (e.g., Del Zanna et al. 2002; Del Zanna & Mason 2003, and references therein) was originally proposed as an isothermality test. The EM loci curves are formed by the set of  $(EM, T_e)$  pairs for which the isothermal theoretical intensities exactly match the observations in a given band or spectral line. The isothermal hypothesis can then in principle be ruled out if there is no single crossing point of the loci curves. But a fundamental ambiguity arises from the inevitable presence of measurement errors.

Under the hypothesis of ideal measurements, the observations and the theoretical intensities are both reduced to  $I_b^0$ . Hence, the isothermal solution for a perfectly isothermal plasma leads to a residual  $\chi^2$  exactly equal to 0, and the EM loci curves all intersect at a common point. But, in reality, the presence of errors leads to over- or underestimations of the theoretical and observed intensities, which translates to a non-zero  $\chi^2$ . In this case, even though the plasma is isothermal, the EM loci curves do not intersect at a single point, each one being randomly shifted from its original position. But even with perfect measurements, the isothermal hypothesis would also yield a residual greater than zero if the observed plasma is multithermal, because in this case the  $I_b^0$  and  $I_b^{\text{th}}$  are intrinsically different. Therefore, measurement errors can be incorrectly interpreted as deviations from isothermality and vice versa; a variety of multithermal plasmas can be statistically consistent with the isothermal hypothesis. The question is then whether or not a perfectly isothermal plasma can be distinguished from a multithermal one and if so, under what conditions.

We thus investigate in this section the isothermal solutions  $\xi_{\text{iso}}^I$  obtained from simulated observations  $I_b^{\text{obs}}$  of plasmas of different degrees of multithermality. The adopted statistical approach allows us to quantify to what extent the robustness of the inversion is affected as a function of the degree of multithermality of the plasma. The plasma is assumed to have a

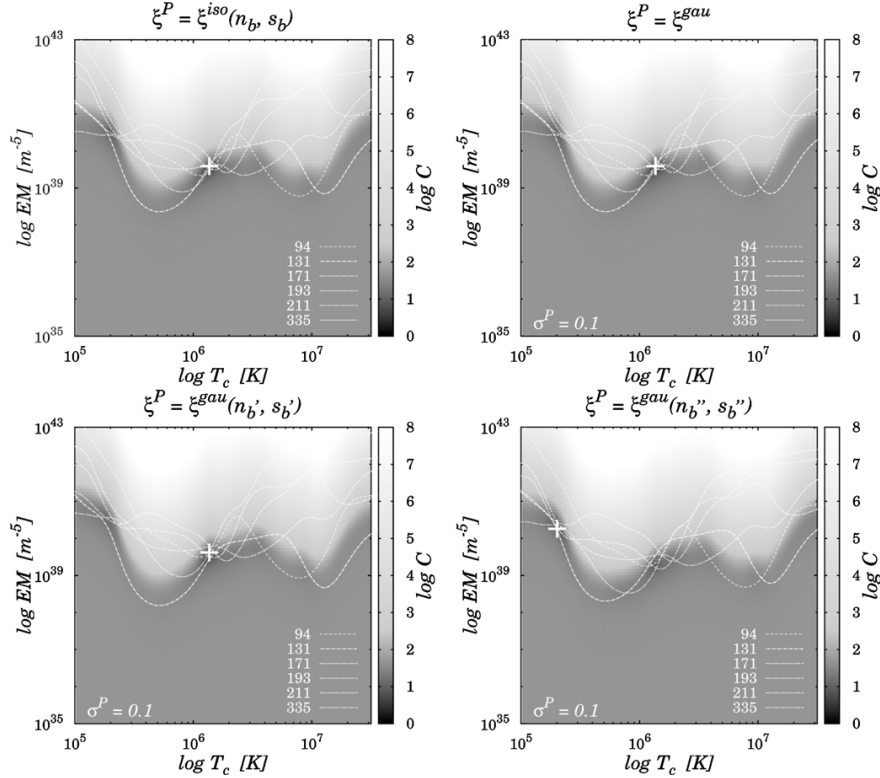


**Figure 2.** Equivalence between uncertainties and multithermality. The criterion  $C(EM, T_c)$  given by Equation (3), represented in gray scale, and its absolute minimum, marked by a white plus sign. The EM loci curves for each of the six AIA coronal bands are also represented (white lines), superimposed on the criterion. The location of the absolute minimum provides the isothermal solution  $\xi^I$  for a plasma having DEMs  $\xi^P$  centered on  $T_c^P = 1.5$  MK, and a total emission measure of  $2 \times 10^{29} \text{ cm}^{-5}$ . Top left: isothermal plasma having a DEM  $\xi^P = \xi^{\text{iso}}$  in the presence of random and systematic errors. Top right: multithermal plasma having a Gaussian DEM  $\xi^P = \xi^{\text{gau}}$  with a width  $\sigma^P = 0.1 \log T_e$ , without uncertainties. Uncertainties and multithermality both produce comparable deviations of the EM loci curves. Bottom: same as top right, but for two different realizations of the random and systematic errors  $n_b$  and  $s_b$ .

Gaussian DEM defined in  $\log T_e$  as

$$\xi_{\text{gau}}^P(EM, T_c, \sigma) = EM \mathcal{N}(\log T_e - \log T_c),$$

$$\text{with } \mathcal{N}(x) = \frac{1}{\sigma \sqrt{2\pi}} \exp\left(-\frac{x^2}{2\sigma^2}\right), \quad (4)$$

where EM is the total emission measure,  $T_c$  is the central temperature, and  $\sigma$  is the width of the DEM. It represents a plasma predominantly distributed around a central temperature  $T_c$  and can represent both isothermal and very multithermal plasmas.

The theoretical intensities  $I_b^{\text{th}}$  are limited to the case of isothermal solutions, corresponding to a DEM

$$\xi_{\text{iso}}(EM, T_c) = EM \delta(T_e - T_c), \quad (5)$$

where  $\delta$  is Dirac's delta function and EM is the total emission measure. The solution  $\xi^I$  of the inversion process then provides the pair  $(T_c^I, EM^I)$  that best explains the observations. The reference intensities  $I_b^0$  (see the previous section), used to compute both  $I_b^{\text{obs}}$  and  $I_b^{\text{th}}$  have been tabulated once and for all for 500 central temperatures from  $\log T_c(\text{K}) = 5$  to 7.5, 200 EMs from  $\log EM(\text{cm}^{-5}) = 25$  to 33, and for the Gaussian model 80 DEM widths from 0 to 0.8, expressed in units of  $\log T_e$  (see Section 2.3.2 of Paper I).

### 2.1. Ambiguity between Uncertainties and Multithermality

In Figure 2, the criterion  $C(EM, T_c)$  (Equation (3)) is plotted for different plasma configurations. It is represented in gray scale<sup>4</sup> and its absolute minimum, corresponding to the solution  $\xi^I$ , is marked by a white plus sign. The criterion is a function of the two parameters EM and  $T_c$  defining the isothermal solutions (Equation (5)). The white curves are the EM loci curves, corresponding to the minimum of the contribution of each band to the total criterion. In all panels, the simulated plasmas have DEMs centered on the typical coronal temperature  $T_c^P = 1.5 \times 10^6$  K, and a total emission measure  $EM^P = 2 \times 10^{29} \text{ cm}^{-5}$ , an active region value guaranteeing signal in all six bands (see Section 3 and Figure 3 in Paper I). The top left panel corresponds to an isothermal plasma ( $\sigma = 0$ ), which corresponds to the case presented in Section 3.2 of Paper I). Because of systematics,  $s_b$ , and instrumental noises,  $n_b$ , and thus the over- or underestimation of the observed and theoretical intensities  $I_b^{\text{obs}}$  and  $I_b^{\text{th}}$ , the EM loci curves are shifted up and down along the EM axis, with respect to the zero-uncertainty case (i.e.,  $n_b$  and  $s_b = 0$ ). Therefore, the curves never intersect all six at a single position, thus giving  $\chi^2 > 0$ . However, multithermality has the same effect: the criterion presented in the top right corresponds to a slightly multithermal plasma having

<sup>4</sup> All the criteria presented in this paper are available in color online at [ftp.ias.u-psud.fr/cguennou/DEM\\_AIA\\_inversion/](http://ftp.ias.u-psud.fr/cguennou/DEM_AIA_inversion/).



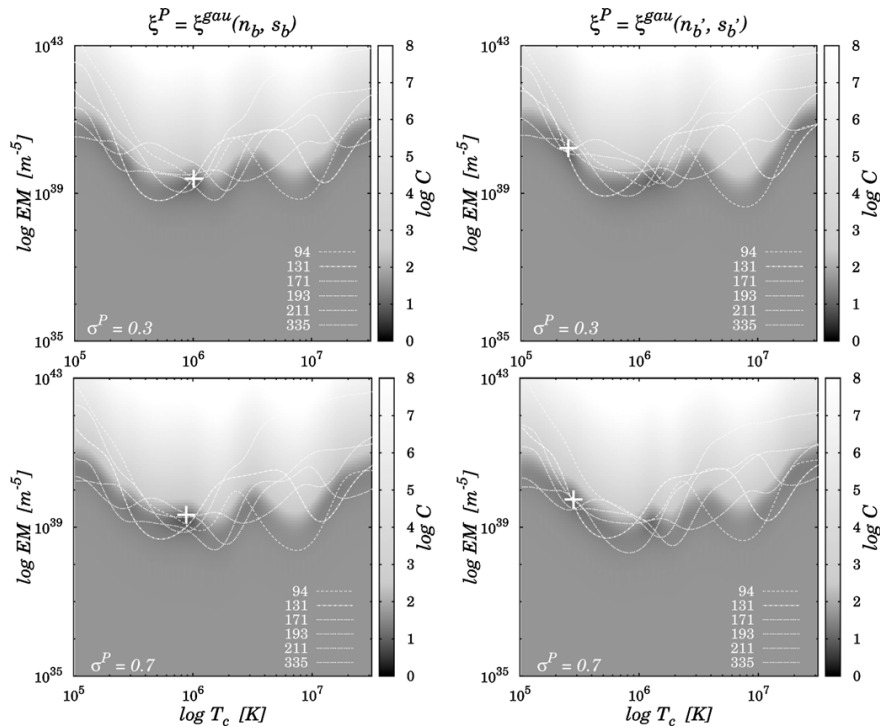


**Figure 3.** Isothermal solutions for different thermal widths. Same as Figure 2 for larger DEMs plasma widths. In the top row the plasma has a Gaussian DEM  $\sigma^P = 0.3 \log T_e$ , and  $\sigma^P = 0.7 \log T_e$  in the bottom row. For each thermal width, two different realizations of the random and systematic errors are presented, showing that the location of the absolute minimum can greatly vary.

a Gaussian DEM width of  $\sigma^P = 0.1 \log T_e$ . Even though in this case uncertainties have not been added, the loci curves and the absolute minimum, corresponding to the location where the curves are the closest together, are also shifted relative to each other along the EM axis and there is no single crossing point. Thus, errors and multithermality can both produce comparable deviations of the observations from the ideal isothermal case, hence the fundamental ambiguity between the two. The two criteria of the bottom panels have been obtained with the same plasma Gaussian DEM distribution, but now in the presence of random perturbations. These two independent realizations of the uncertainties illustrate an example of the resulting dispersion of the solutions.

In Figure 3, we increased the DEM width to  $\sigma^P = 0.3 \log T_e$  (top row) and  $\sigma^P = 0.7 \log T_e$  (bottom row) while keeping the same EM and central temperature. For each width, the left and right panels show two realizations of the uncertainties. The corresponding configuration of the loci curves and thus the value and position of the absolute minimum can greatly vary, even though the plasma is identical in both cases. It also appears that privileged temperature intervals exist where the solutions tend to concentrate. This phenomenon is intrinsically due to the shape of the EM loci curves. In the next subsection, we characterize the respective probabilities of occurrence of the various solutions for a wide range of plasma conditions. From the examples presented in Figure 3, we also note that the vertical spread of the loci curves tends to be larger for wider DEMs, which corresponds to larger  $\chi^2$  residuals. In Section 2.3, we will determine up to what DEM width the observations can be considered to be consistent with the isothermal hypothesis.

## 2.2. Probability Maps

We consider Gaussian DEM plasmas and scan all possible combinations of central temperatures and widths used to precompute the reference theoretical intensities. The total EM is kept constant at  $EM^P = 2 \times 10^{29} \text{ cm}^{-5}$ . For each combination of plasma parameters, 5000 Monte Carlo realizations of the random perturbations  $n_b$  and systematics  $s_b$  are obtained, leading to 5000 estimates of the observed intensities  $I_b^{\text{obs}}(\xi^P)$  in each band  $b$ . The isothermal least-square inversion of these 5000 sets of AIA simulated observations provides as many solutions  $\xi^I$ , allowing an estimation of  $P(\xi^I | \xi^P)$ .

Figures 4–6 show the resulting temperature probability maps for  $\sigma^P = 0.1, 0.3$ , and  $0.7 \log T_e$ , respectively.<sup>5</sup> The isothermal plasma case ( $\sigma^P = 0$ ) is shown in Figure 6 of Paper I. In all figures, the probability  $P(T_c^I | T_c^P)$  is obtained by vertically reading panels (a), given the probability of finding a solution  $T_c^I$  knowing the plasma central temperature  $T_c^P$ . The probability profiles for two specific plasma temperatures,  $1.5 \times 10^6$  and  $7 \times 10^6$  K, are shown in panels (b) and (c). Using Baye's theorem, the probability maps  $P(T_c^P | T_c^I)$  of panels (e) are obtained by normalizing  $P(T_c^I | T_c^P)$  to  $P(T_c^I)$ , the probability of obtaining  $T_c^I$  whatever  $T_c^P$  (panels (d)). In the bottom right panels (f) and (g), we show two example horizontal profiles giving the probability that the plasma has a central temperature  $T_c^P$  knowing the inverted temperature  $T_c^I$ .

In panels (a) and (e) of Figure 4, the most probable solutions are located around the diagonal. However, compared to the

<sup>5</sup> The probability maps for 80 widths from 0 to  $0.8 \log T_e$  are available in color online at [ftp.ias.u-psud.fr/cguennou/DEM\\_AIA\\_inversion/](http://ftp.ias.u-psud.fr/cguennou/DEM_AIA_inversion/).

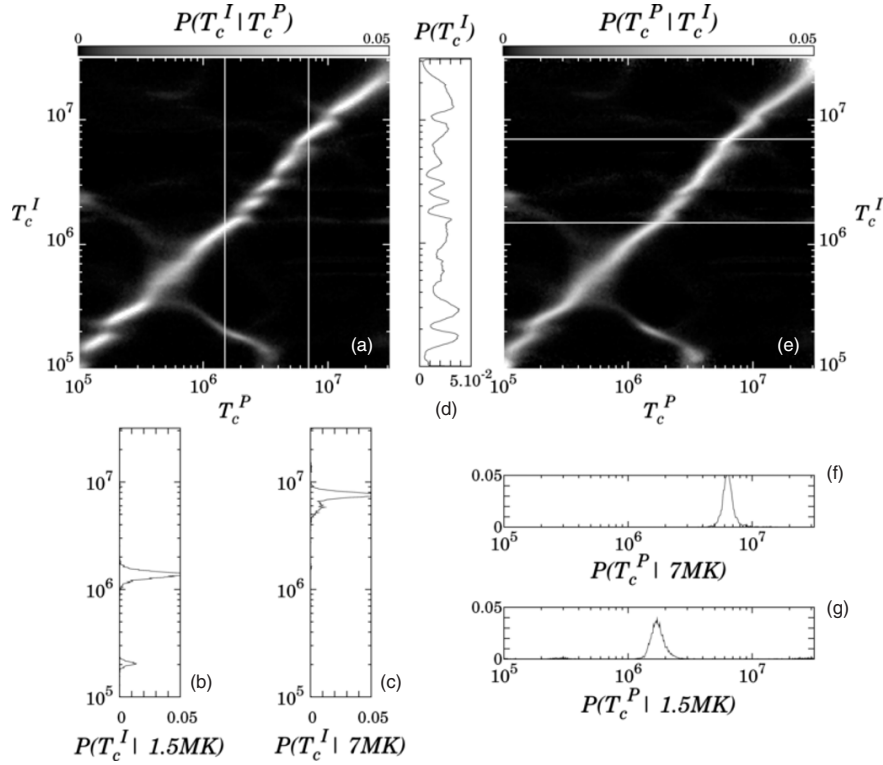


**Figure 4.** Maps of probabilities considering a Gaussian DEM plasma  $\xi^P = \xi^{\text{gau}}$  having a narrow thermal distribution of  $\sigma^P = 0.1 \log T_e$ , obtained by 5000 Monte Carlo realizations of the random and systematic errors  $n_b$  and  $s_b$ , and investigating the isothermal solutions. (a) Probability map  $P(T_c^I | T_c^P)$ , vertically reading. The central temperature  $T_c^I$  resulting from the inversion is presented whatever the total emission measure  $\text{EM}^I$ . (b) and (c) Probability profiles of  $T_c^I$  for plasma central temperatures  $T_c^P = 1.5 \times 10^6$  and  $7 \times 10^6$  K (vertical lines in panel(a)). (d) Total probability of obtaining  $T_c^I$  whatever  $T_c^P$  (see Section 1 and Section 2.1 of Paper I). (e) Vice versa, probability map  $P(T_c^P | T_c^I)$ , horizontally reading, inferred by means of Bayes' theorem using  $P(T_c^I | T_c^P)$  and  $P(T_c^I)$ . (f) and (g) Probability profiles of  $T_c^P$  knowing that the inversion result is, from top to bottom,  $7 \times 10^6$  and  $1.5 \times 10^6$  K.

case of an isothermal plasma (see Figure 6 of Paper I), the distribution is wider, irregular, and deviations from the diagonal greater than its local width are present. As shown by panel (d) and the nodosities in the map (a), the unconditional probability of obtaining a result  $T_c^I$  is nonuniform, meaning that some inverted temperatures are privileged whereas others are unlikely. Compared with Figure 6 of Paper I, profile (b) shows that the probability of secondary solutions at  $T_c^P = 1.5 \times 10^6$  K is increased with respect to the isothermal case. The apparition of these two solutions is illustrated in the bottom row of Figure 2. The bottom right panel corresponds to a realization of the errors yielding a solution close to the diagonal, while the bottom left panel of the same figure illustrates a case where the absolute minimum of the criterion is located at low temperature. Using the map of  $P(T_c^P | T_c^I)$ , it is, however, possible to correctly interpret the low-temperature solutions as also compatible with  $1.5 \times 10^6$  K plasma (profile (g)).

In Figure 5, the plasma DEM width is increased to  $\sigma^P = 0.3 \log T_e$ . As a result, the above-described perturbations with respect to the isothermal plasma case are amplified. The diagonal structure has almost disappeared, with discontinuities and reinforced and more diffuse nodosities. Multiple solutions of comparable probabilities are present over large ranges of plasma temperatures and consequently, the estimated  $T_c^I$  can be very different from the input  $T_c^P$ . For example, panel

(c) shows that for a  $7 \times 10^6$  K plasma, the most probable  $T_c^I$  is either  $1.6 \times 10^5$  or  $3 \times 10^5$  K. The unconditional probability  $P(T_c^I)$  of panel (d) is very nonuniform, some ranges of estimated temperatures being totally unlikely (e.g.,  $T_c^I = [1.5 \times 10^6, 4 \times 10^6]$  K) while others are probable for large intervals of  $T_c^P$  (e.g.,  $T_c^I = 3 \times 10^5$  K or  $10^6$  K). However, despite the jaggedness of  $P(T_c^I | T_c^P)$ , the map of  $P(T_c^P | T_c^I)$  can once again help to properly interpret the result of the inversion. For example, profile (g) shows that for  $T_c^I = 1.5 \times 10^6$  K, the distribution of  $T_c^P$  is distributed around  $T_c^P = 10^7$  K, which is exactly the plasma temperature that can yield an inversion at  $T_c^I = 1.5 \times 10^6$  K (see panel (a)). Panel (f), providing the probability distribution  $T_c^P$  knowing that the inversion result is  $T_c^I = 7 \times 10^6$  K, exhibits a broad probability distribution around  $T_c^P = 1.5 \times 10^7$ , showing that the plasma temperature thus deduced is very uncertain. This is to be compared to the  $0.05 \log T_e^P$  temperature resolution of the isothermal case (see Section 3.2 of Paper I).

As the DEM becomes even larger, the impact on the robustness of the inversion becomes greater. At  $\sigma^P = 0.7 \log T_e$ , the probability map  $P(T_c^I | T_c^P)$  of Figure 6(a) and the corresponding probability  $P(T_c^I)$  clearly show two privileged solutions:  $T_c^I = 10^6$  and  $3 \times 10^5$  K. The estimated isothermal temperatures are always the same for any  $T_c^P$ , as illustrated by



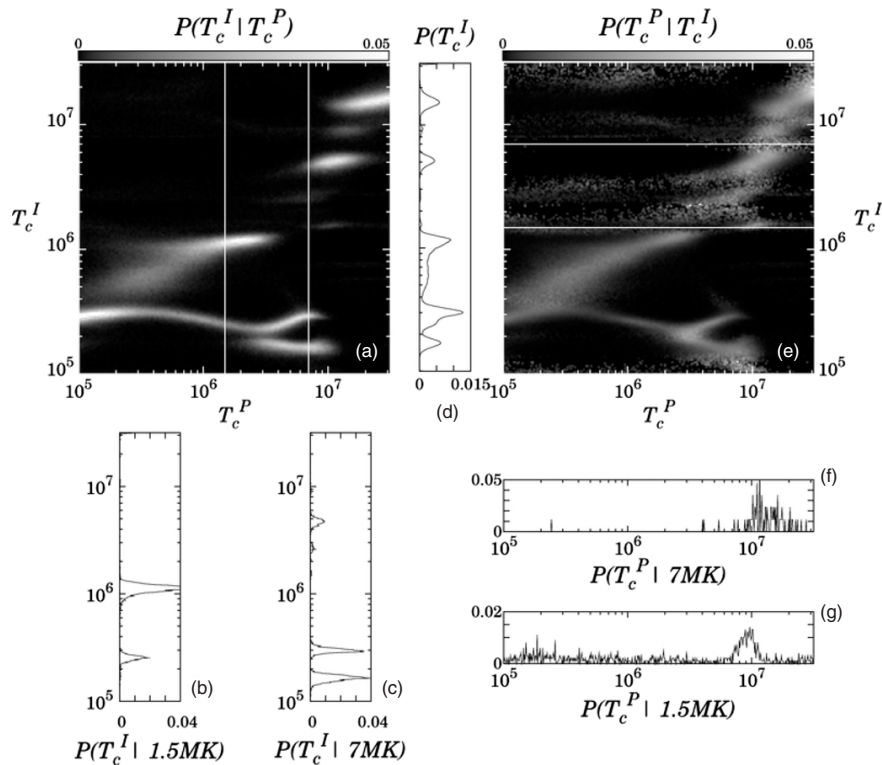


**Figure 5.** Same as Figure 4, but with a plasma DEM width increased to  $\sigma^P = 0.3 \log T_e$ . Many perturbations, already visible in Figure 4, are amplified: the distribution is wider, irregular, and the diagonal structure disappeared (see panel (a)). The presence of multiple solutions of comparable probabilities is increased for a large range of plasma temperatures  $T_c^P$ , leading to very different estimated  $T_c^I$  from the input  $T_c^P$ . The probability map  $P(T_c^I | T_c^P)$  can help us to properly interpret the inversion result, taking into account the secondary solutions and providing their respective probability.

panels (b) and (c). Therefore, the inversion results  $T_c^I$  contain no information on the plasma central temperature  $T_c^P$ . This is illustrated by the lack of structure in the probability map  $P(T_c^P | T_c^I)$  of panel (e). Profile (g) shows that for  $T_c^I = 1.5 \times 10^6$  K, the distribution of  $T_c^P$  extends over entire the temperature range.

### 2.3. Interpretation

We have shown that as the width of the plasma DEM increases, multiple solutions to the isothermal inversion appear. This phenomenon has been already mentioned by Patsourakos & Klimchuk (2007), using triple-filter TRACE data. After a proper treatment of the uncertainties, the authors found that their observations of coronal loops were consistent with both a high ( $\approx 1.5 \times 10^6$  K) and a low ( $\approx 5 \times 10^5$  K) isothermal plasma temperature. They correctly concluded that without a priori knowledge of the physical conditions in these loops, they could not rule out the cool plasma solutions. Even though we used six bands, multiple solutions appear anyway with increasing plasma width. In addition, as we have seen in Paper I, multiple solutions can exist even with an isothermal plasma if only a limited number of bands is available. This is another illustration of the similar effects of errors and multithermality.

The isothermal temperature solutions become progressively decoupled from the plasma central temperature as the width of the DEM increases. For very large DEMs (Figure 6), the inversion process yields exclusively either  $3 \times 10^5$  K or  $10^6$  K whatever the plasma  $T_c^P$ . These two temperatures correspond to

the preferential locations of the minima shown in the criteria of Figure 3. This is a generalization of the phenomenon analyzed by Weber et al. (2005) in the simpler case of the TRACE 19.5 over 17.3 nm filter ratio. The authors showed that in the limit of an infinitely broad DEM, the band ratio tends to a unique value equal to the ratio of the integrals of the temperature response functions. Furthermore, they showed that as the width of the DEM increases, the temperature obtained from the band ratio becomes decoupled from the DEM central temperature. We have found a similar behavior in the more complex situation of six bands. This is not, however, an intrinsic limitation of AIA. We can predict that the same phenomenon will occur with any number of bands or spectral lines. Indeed, for an infinitely broad DEM, since the observed intensities are equal to the product of the total EM by the integral of the response functions (Equation (2)), they are independent from the plasma temperature. Therefore, the inversion will yield identical results for any plasma temperature  $T_c^P$ , whatever the number of bands or spectral lines.

#### 2.3.1. Defining Isothermality

As already noted in Section 2.1 and in Figure 2, larger DEM widths correspond to larger squared residuals. From Paper I, the distribution of residuals to be expected for an isothermal plasma is known. Examining, then, the residuals for the solutions given in the probability maps of Section 2.2, the solutions may not all be statistically consistent with the isothermal hypothesis. We will thus analyze the distribution of residuals to define rigorously

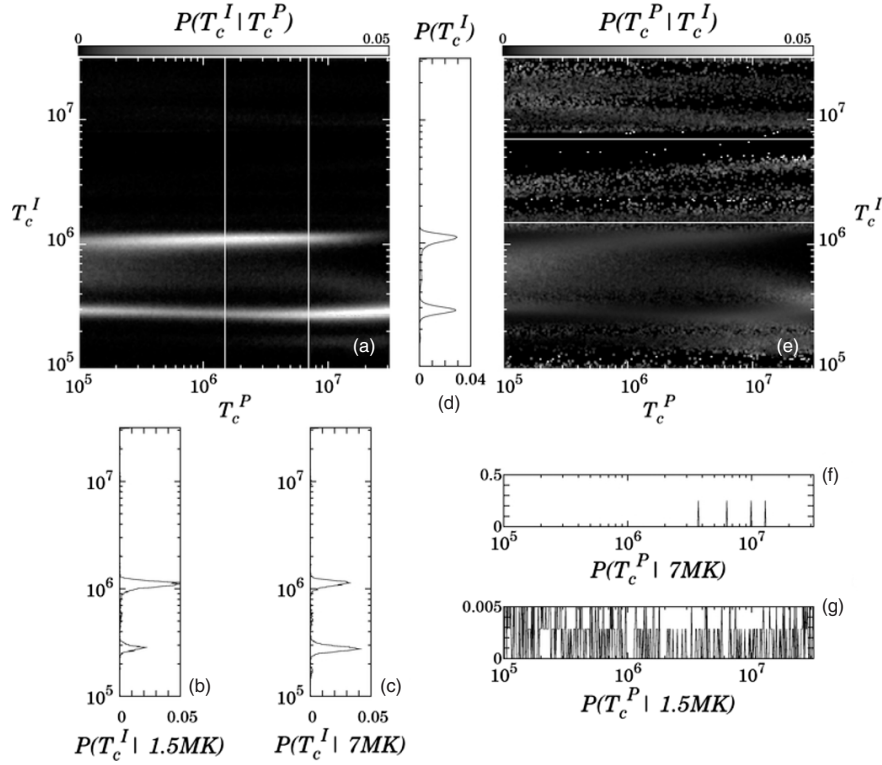


**Figure 6.** Same as Figure 4, but in the case of the plasma DEM width being increased to  $\sigma^P = 0.7 \log T_e$ . The impact on the robustness of the inversion is clearly increased in this case, showing two privileged isothermal solutions  $T_c^I$ , totally decorrelated from the input  $T_c^P$ . As a result, no information regarding the central temperature of the DEM can be extracted from the inversion.

a test of the adequacy of the isothermal model used to interpret the data.

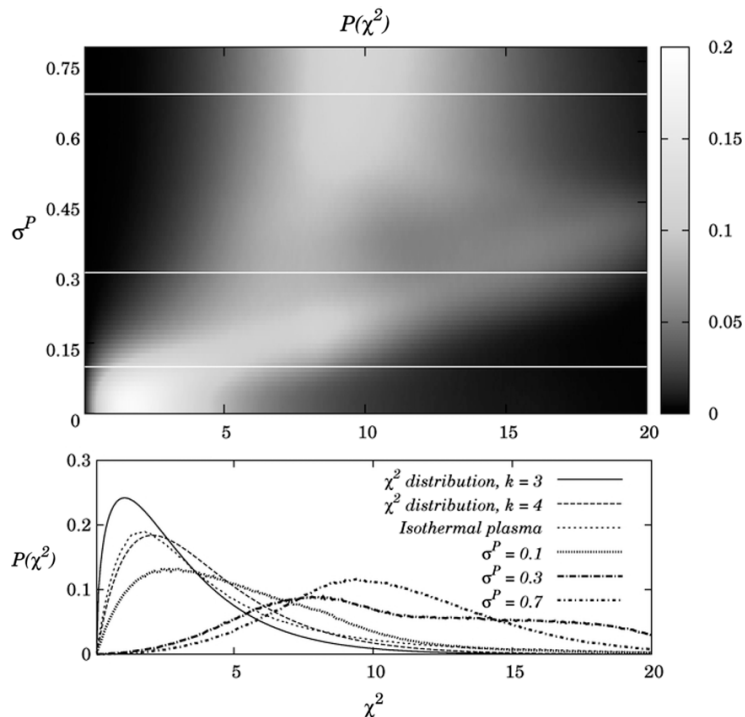
Because both the random and systematic errors  $n_b$  and  $s_b$  have been modeled by a Gaussian random variable, if the DEM model used to interpret the data can represent the plasma DEM, the residuals are equal to the sum of the square of six normal random variables (see Equation (3)). Since we adjust the two parameters EM and  $T_c$ , the residuals should thus behave as a four-degree  $\chi^2$  distribution.

Figure 7 shows the distribution of the squared residuals for all of the 80 DEM widths considered in the simulations. The shades of gray in the top panel correspond to the probability of obtaining a given  $\chi^2$  value (abscissa) as a function of the width of the plasma DEM (ordinate). In the bottom panel, four profiles give the distribution of squared residuals obtained for an isothermal plasma (thin dotted line) and for the three DEM widths discussed in Section 2.2:  $\sigma^P = 0.1$  (thick dotted line), 0.3 (thick dashed curve), and  $0.7 \log T_e$  (thick dash-dotted curve), corresponding to the white horizontal lines on the top panel. The theoretical  $\chi^2$  distributions of three (thin solid curve) and four degrees (dashed curve) are also plotted.

If the plasma is isothermal, the distribution of the residuals is slightly shifted toward a three-degree  $\chi^2$  instead of the expected four-degree one. In Paper I, we interpreted this as a correlation between the six AIA coronal bands. The distributions of residuals progressively depart from the isothermal case as the DEM width of the simulated plasma increases. The distributions become broader and their peaks are shifted toward higher values,

forming the diagonal structure in the top panel of Figure 7. This behavior stops around  $\sigma^P = 0.4 \log T_e$ . Above, the peaks of the distributions are shifted back toward smaller values and remain constant. As the DEM becomes wider, the simulated observations become independent from the plasma parameters, and all inversions tend to give the same solution and the same residuals.

These distributions of residuals provide a reference against which to test the pertinence of the isothermal model. The isothermal hypothesis can, for example, be invalidated for the solutions biased toward  $T_c^I \approx 1$  MK and corresponding to very multithermal plasmas (e.g.,  $\sigma^P = 0.7$ ; see Section 2.2 and Figure 6). Indeed, for a given inversion and its corresponding residual, the top panel of Figure 7 gives the most probable width of the plasma, assuming it has a Gaussian DEM. Let us assume that an isothermal inversion returns a residual equal to 5. Analyzing the histogram corresponding to the bottom row of the top panel of Figure 7 ( $\sigma^P = 0$ ), we can show that an isothermal plasma has a 68.2% chance of yielding  $\chi^2 \leq 5$ . This residual can therefore be considered consistent with an isothermal plasma. But reading the plot vertically, we see that the probability  $P(\chi^2 = 5)$  is greater for multithermal plasmas and peaks around  $\sigma^P = 0.12$ , which is thus in this case the most probable Gaussian width. For larger residuals, the situation is more complex because several plasma widths can have equally high probabilities. Past  $\chi^2 = 3.5$  the plasma has a higher probability to be Gaussian than isothermal and a Gaussian inversion is required to properly determine its most probable width and central temperature.



**Figure 7.** In the top panel, the distributions of the sum of the squared residuals corresponding to isothermal inversions of Gaussian DEM plasmas, as a function of the DEM width  $\sigma^P$ . Higher probabilities correspond to lighter shades of gray. The bottom panel shows cuts at  $\sigma^P = 0$  (isothermal), 0.1, 0.3, and 0.7  $\log T_e$  along with theoretical  $\chi^2$  distributions of three and four degrees.

Figure 7 is a generalization of the results obtained by Landi & Klimchuk (2010). It is equivalent to their Figure 2, identifying our  $\chi^2$  with their criterion  $F_{\min}$  and their solid line to the maximum of our  $\chi^2$  distribution as a function of  $\sigma^P$ . Their dashed lines are equivalent to our values of the half-peak, as a function of  $\sigma^P$ , given by the resolution of  $\chi^2(\sigma^P) = \chi^2_{\max}(\sigma^P)/2$ . Their Figure 2 was computed using 13 individual spectral lines for a 1 MK plasma and extends only up to  $\sigma^P \approx 0.2$ , while our Figure 7 was computed for the six AIA bands over a wide range of central temperatures and for widths up to  $\sigma^P = 0.8$ . Despite these differences, the two figures exhibit the same global behavior. Indeed, for any number of spectral lines or bands, the residuals of the isothermal inversion tend to increase as the width of the plasma DEM increases.

### 3. MULTITHERMAL SOLUTIONS

We now focus on multithermal solutions. The ability of AIA to reconstruct the DEM given the uncertainties is evaluated, and the probability maps associated to all parameters are computed, allowing us to take into account all the Gaussian DEMs consistent with the simulated observations. Both cases of consistent and inconsistent DEMs models between the simulations and the inversion assumptions are examined. After the previous section on isothermal solutions, this generalizes the study of the impact of a wrong assumption on the DEM shape.

As in the previous section, the simulated observations remain Gaussian, but we now consider Gaussian solutions, i.e., theoretical intensities  $I_b^{\text{th}}$  tabulated for the Gaussian DEM model. The model can thus in principle perfectly represent the plasma conditions.

#### 3.1. Three-dimensional Criterion

Investigating multithermal Gaussian solutions now, the least-square criterion given by Equation (3) thus has three dimensions  $C(\xi^{\text{gau}}) = C(\text{EM}, T_c, \sigma)$ . This three-dimensional parameter space is systematically scanned to locate the theoretical intensities best describing the simulated observations. Figure 8 shows this criterion for three cases illustrating different degrees of multithermality. In each row, from top to bottom, the simulated plasma has a DEM width  $\sigma^P$  of 0.1, 0.3, and 0.7  $\log T_e$ , respectively, centered on the temperature  $T_c = 1.5 \times 10^6$  K. On the left panels, the background image represents  $C(\text{EM}, T_c, \sigma^J)$ , the cut across the criterion in the plane perpendicular to the DEM width axis at the width  $\sigma^J$  corresponding to the absolute minimum (white plus sign). The curves are the equivalent of the loci EM curves in a multithermal regime: for each band  $b$  and for a given DEM width  $\sigma^P$ , they represent the loci of the pairs  $(\text{EM}, T_c)$  for which the theoretical intensities  $I_b^{\text{th}}$  are equal to the observations  $I_b^{\text{obs}}$ . As  $\sigma$  varies, they thus describe a loci surface in the three-dimensional criterion. The difference with the isothermal loci curves is that the theoretical intensities  $I_b^{\text{th}}$  have been computed for the multithermal case (i.e., considering a Gaussian DEM), and thus the parameter  $\sigma$  must be now considered. The right panels of Figure 8 display  $C(\text{EM}^J, T_c, \sigma)$ , the cuts across the criterion in the plane perpendicular to the EM axis at the  $\text{EM}^J$  corresponding to the absolute minimum of the criterion (also represented by a white plus sign).

The impact of multithermality on the criterion topology is clearly visible in the loci curves, inducing a smoothing of the curves as the multithermality degree increases. Indeed, the intensities  $I_b^0$  as a function of the central temperature

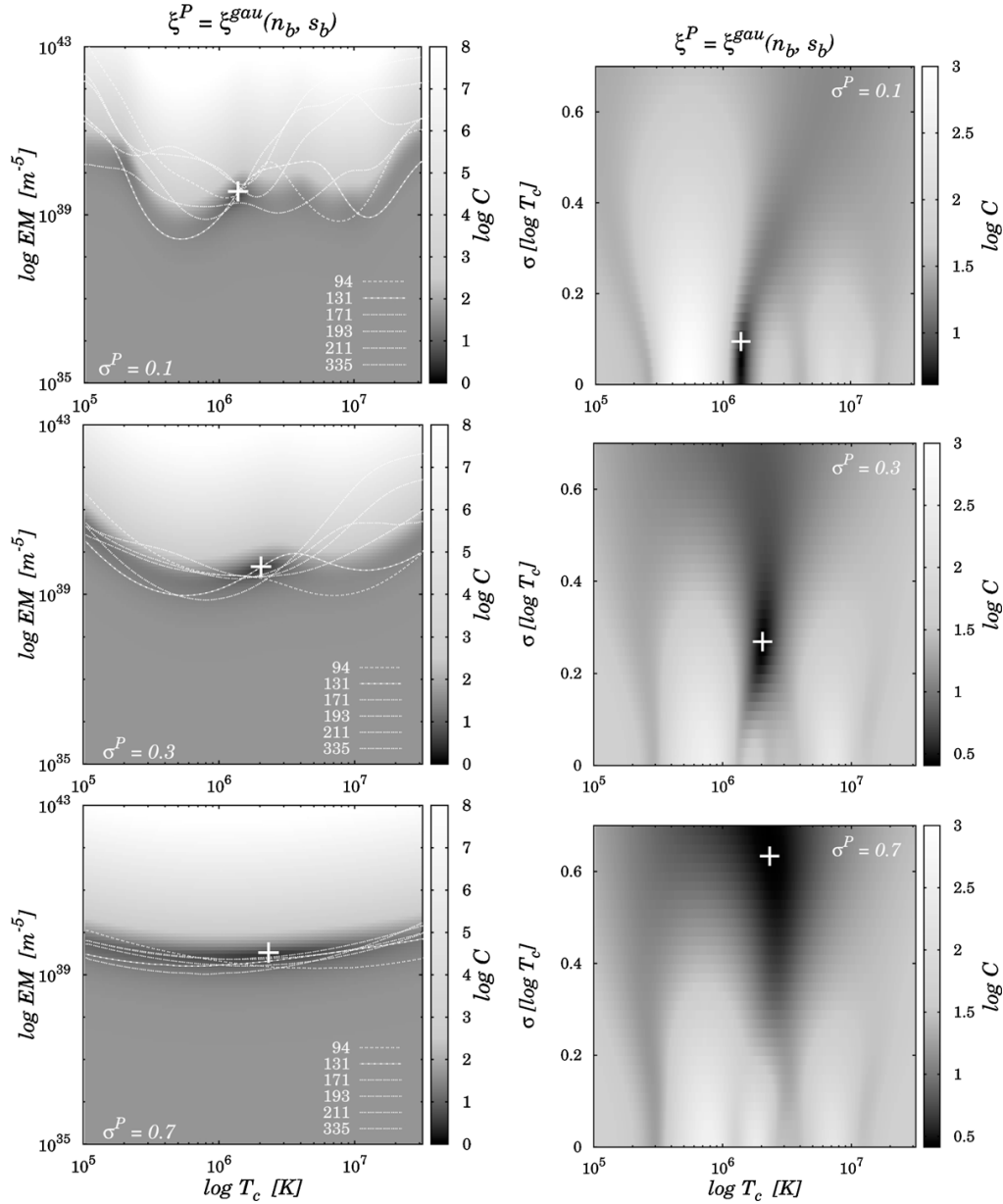


**Figure 8.** Criterion in case of Gaussian multithermal DEM inversions. The three-dimensional criterion is a function of  $EM^P$ ,  $T_c^P$ , and  $\sigma^P$ . The simulated plasma has a Gaussian DEM centered on 1.5 MK and a different width for each row. From top to bottom:  $\sigma^P = 0.1, 0.3,$  and  $0.7 \log T_c$ . The superimposed curves on the left panels represent the equivalent of the EM loci emission measure curves in a multithermal regime (see the detailed description in Section 3.1).

can be expressed as the convolution product between the instrument response functions and the DEM (see Section 2.3.2 of Paper 1). Therefore, the reference intensities  $I_b^0(EM, T_c, \sigma)$  computed for multithermal plasmas are equal to the isothermal ones smoothed along the  $T_c$  axis. As a result, the criterion exhibits a smoother topology and the minimum areas become broader and smoother as the multithermality degree increases, introducing more indetermination in the location of the absolute minimum. For each row, the realization of the uncertainties  $n_b$  and  $s_b$  yields a solution that is close to the simulation input. The cuts are therefore made at similar locations in the criterion in

order to best illustrate the modification of its topology. We will now analyze to what extent the distortion of the criterion affects the robustness of the inversion.

### 3.2. Probability Maps

In the case of DEM models defined by three parameters, and since the plasma  $EM^P$  is fixed, the probability matrices  $P(EM^I, T_c^I, \sigma^I | EM^P, T_c^P, \sigma^P)$  resulting from the Monte Carlo simulations have five dimensions. In order to illustrate the main

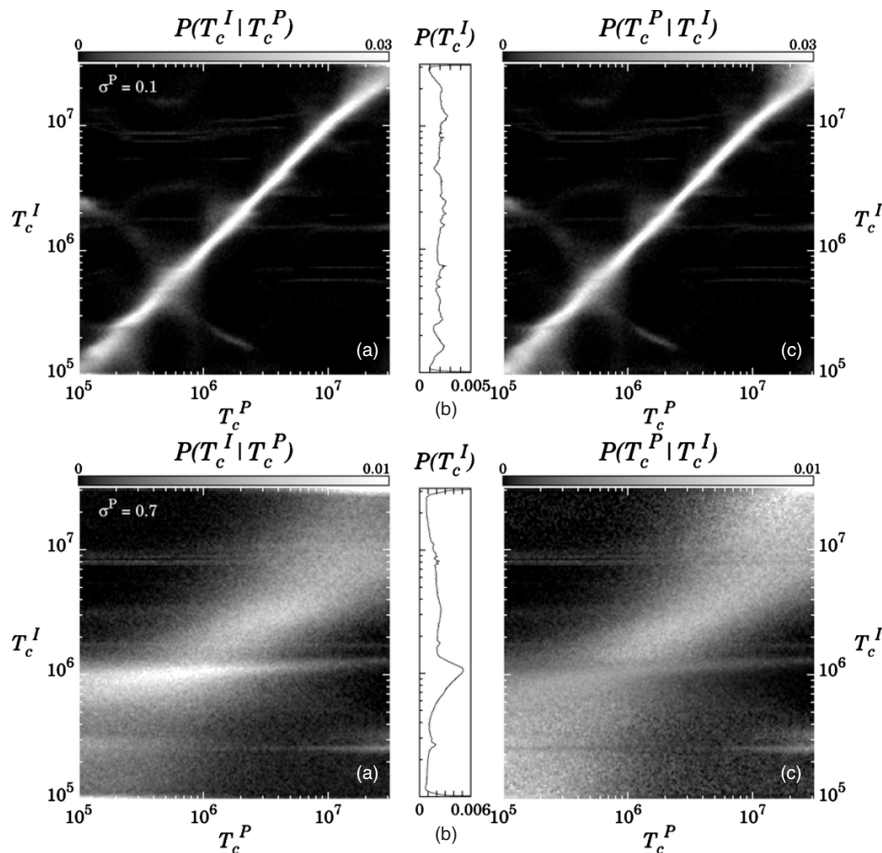


**Figure 9.** Same as Figure 4 but now investigating the multithermal solutions. The simulated observations are computed for DEM widths of  $\sigma^P = 0.1$  (top row) and  $0.7 \log T_e$  (bottom row). The probabilities are represented here whatever the emission measure  $EM^I$  and the Gaussian width  $\sigma^I$  returned by the minimization scheme. In the case of a low degree of multithermality plasmas, the solutions remain distributed around the diagonal. However, for broad DEM distributions, the solutions appear to be biased toward  $\sim 1$  MK, especially for plasmas exhibiting central temperature lower than 2 MK.

properties of these large matrices, we rely on combinations of fixed parameter values and summation over axes.

The associated probability maps are displayed in Figure 9 for simulated plasmas characterized by  $\sigma^P = 0.1$  (top panel) and  $\sigma^P = 0.7 \log T_e$  (bottom panel).<sup>6</sup> The probability maps are represented whatever the EM and DEM width obtained by inversion, i.e., the probabilities  $P(EM^I, T_c^I, \sigma^I | EM^P, T_c^P, \sigma^P)$  are integrated over  $EM^I$  and  $\sigma^I$ . In case of a narrow DEM distribution ( $\sigma^P = 0.1$ , top panels), the solutions are mainly distributed along the diagonal, with some secondary solutions at low probabilities. The accuracy of the determination of the central temperature  $T_c^P$  is improved compared to the isothermal inversion of the same plasma as shown in Figure 4: the diagonal is more regular and  $P(T_c^I)$  is more uniform. However, increasing the width of the DEM of the simulated plasma reduces the robustness of the inversion process. In the bottom panels ( $\sigma^P = 0.7$ ), we observe a distortion and an important spread of the diagonal. In particular, the horizontal structure in panel (a) and the consequent peak of  $P(T_c^I)$  show that the estimated temperature is biased toward  $T_c^I \sim 1$  MK, especially for plasma temperatures  $T_c^P < 2$  MK. This is to be compared with the privileged isothermal solutions in Figure 6, and the

same reasoning applies. For very broad DEMs, because of the smoothing of the  $I_b^0(EM, T_c, \sigma)$  along the  $T_c$  axis, the observed intensities are only weakly dependent on the central temperature, and thus all inversions tend to yield identical results. As a consequence, the probability map  $P(T_c^P | T_c^I)$  shows that over the whole temperature range considered there is a large uncertainty in the determination of  $T_c^P$ . The smoothing of the  $I_b^0(EM, T_c, \sigma)$  is due to the width of the plasma DEM and not to the properties of the response functions. It is therefore to be expected that the uncertainty in the determination of  $T_c^P$  persists even if using individual spectral lines.

In the same way, the conditional probabilities  $P(\sigma^I | \sigma^P)$  and  $P(\sigma^P | \sigma^I)$  of the DEM width are displayed on Figure 10. The probabilities are represented whatever the estimated temperature  $T_c^I$  and emission measure  $EM^I$ , for a simulated plasma having a DEM centered on  $T_c^P = 1$  MK. The conditional probability  $P(\sigma^I | \sigma^P)$  on panel (a) exhibits a diagonal that becomes very wide for large  $\sigma^P$  and from which another broad branch bifurcates at  $\sigma^I = 0.15 \log T_e$ . This branch is the analog of those observed on the temperature axis (top panels of Figure 9). For plasmas having a DEM width greater than  $\sigma^P = 0.3 \log T_e$ , the estimated width  $\sigma^I$  is decoupled from the input  $\sigma^P$ . Profiles (b) and (c) provide the conditional probabilities of  $\sigma^I$  for plasma DEM widths  $\sigma^P = 0.2$  and  $0.6 \log T_e$ , respectively.

<sup>6</sup> The probability maps for 80 widths from 0 to  $0.8 \log T_e$  are available in color online at [ftp.ias.u-psud.fr/cguennou/DEM\\_AIA\\_inversion/](http://ftp.ias.u-psud.fr/cguennou/DEM_AIA_inversion/).



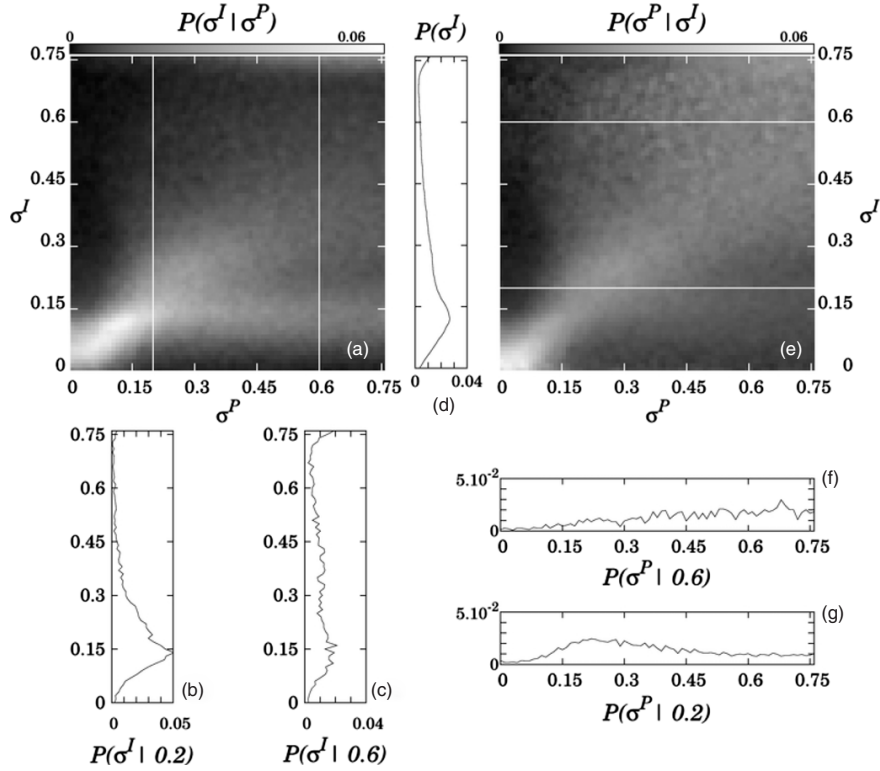


**Figure 10.** Maps of probabilities for the DEM width for a simulated plasma having a Gaussian DEM centered on  $T_c^P = 1$  MK. Probabilities are represented whatever the emission measure  $EM^I$  and the central temperature  $T_c^I$  obtained. The solutions appear to be biased toward  $\sigma^I \sim 0.12 \log T_e$  whatever the plasma widths, even if the situation improves for smaller widths.

As shown by panel (d), the unconditional probability  $P(\sigma^I)$  of obtaining  $\sigma^I$  whatever  $T_c^I$  for this  $10^6$  K plasma is biased toward  $\sigma^I = 0.12 \log T_e$ . Exploring the full probability matrix  $P(EM^I, T_c^I, \sigma^I | EM^P, T_c^P, \sigma^P)$ , we discovered that if the plasma DEM is broad, the small width solutions ( $\approx 0.12 \log T_e$ ) are the ones that were also biased toward a central temperature of  $10^6$  K in Figure 6. This is caused by the shape of the temperature response functions  $R_b(T_e)$ . A minimum is formed in the criterion  $C(T_e, \sigma)$  around ( $T_c = 1$  MK,  $\sigma = 0.12 \log T_e$ ) that tends to be deeper than the other local minima. Since for a very broad DEM plasma the simulated observed intensities  $I_b^{\text{obs}}$  are almost always similar, most of the random realizations of the perturbation  $s_b$  and  $n_b$  lead to an absolute minimum located in this deeper area of the criterion and thus, to the formation of the narrow solutions branch in  $P(\sigma^I | \sigma^P)$  panel (a). Therefore, very multithermal plasmas tend to be systematically measured as near isothermal and centered on  $10^6$  K.

Reading horizontally in panel (e) the inverse conditional probability  $P(\sigma^P | \sigma^I)$ , a large range of DEM widths  $\sigma^P$  is consistent with the estimation  $\sigma^I$ . Both plots (f) and (g), representing two cuts at  $\sigma^I = 0.2$  and  $0.6 \log T_e$ , can be used to deduce the most probable plasma DEM with  $\sigma^P$ . However, at  $\sigma^I = 0.6 \log T_e$ , almost all plasma widths have significant probabilities, considerably restricting the possibility of inferring relevant DEM properties. The situation improves for smaller widths, as shown in panel (g), even though the probability distribution is still broad. For narrow DEM distributions ( $\sigma^P < 0.2$ ), the width of the distribution decreases to about  $0.15 \log T_e$ , which thus represents the width resolution limit.

The analysis of the probability maps demonstrates that the robustness of the inversion is substantially affected by the degree of multithermality of the observed plasma. Furthermore, as we already noted, the simulations presented have been made in a favorable configuration where a significant signal is present in all six bands. For narrow plasma DEMs ( $\sigma^P < 0.15 \log T_e$ ), the six AIA coronal bands enable an unambiguous reconstruction of the DEM parameters within the uncertainties. The precision of the temperature and DEM width reconstruction is then given by the widths of the diagonals in Figures 9 and 10. For the temperature, that width is consistent with the resolution of  $[0.1, 0.2] \log T_e$  given by Judge (2010). However, both the accuracy and the precision of the inversion decrease as the multithermality degree of the simulated plasma increases, a wider range of solutions becoming consistent with the observations. In the case of a very large DEM plasma, the solutions are skewed toward narrow 1 MK Gaussians. The isothermal solutions biased toward 1 MK (Section 2.3) could be invalidated on the basis of their correspondingly high residuals (Section 2.3.1). But the biased Gaussian solutions are by definition fully consistent with a Gaussian plasma. This result generalizes that of Weber et al. (2005), and since our method ensures that the absolute minimum of the criterion is found, it is a fundamental limitation and not an artifact of the minimization scheme. Instead of being evidence for underlying physical processes, the recurrence of common plasma properties derived from DEM analyses may be due to biases in the inversion processes. However, using the type of statistical analysis presented here, it is possible to identify these biases and correct for them.

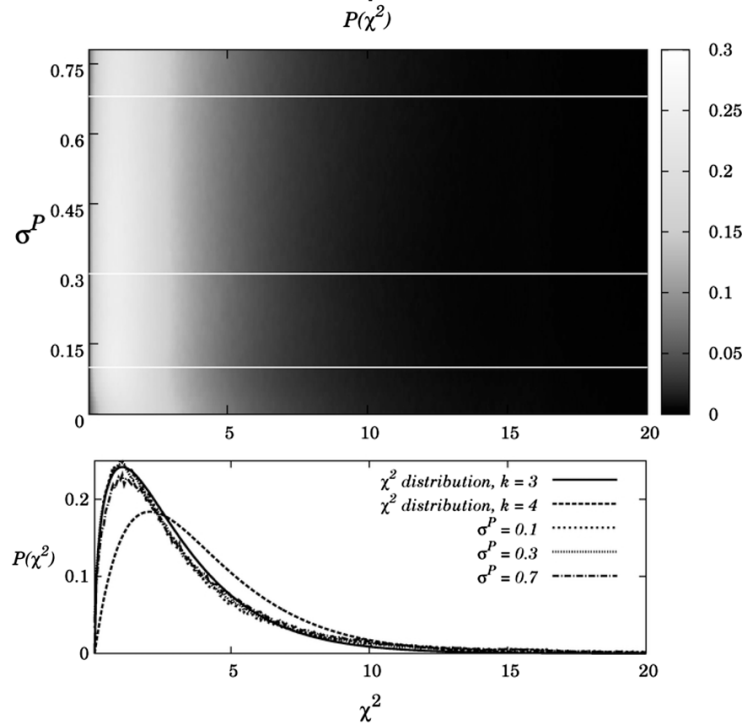


Figure 11. Same as Figure 7 for Gaussian solutions.

### 3.3. Residuals and Model Testing

The distribution of the sum of squared residuals is displayed in the top panel of Figure 11 as a function of the plasma DEM width,  $\sigma^P$ , of the simulated plasma. The three white horizontal lines represent the locations of the cuts at  $\sigma^P = 0.1$  (dotted line), 0.3 (dashed line), and  $0.7 \log T_e$  (dotted dashed line) shown in the bottom panel. Unlike for the isothermal solutions (Figure 3), the distributions are similar for all plasma widths and resemble a three-degree  $\chi^2$  distribution (thin solid line). The most probable value is about 1 and 95% of the residuals are between 0 and 10. Any DEM inversion yielding a  $\chi^2$  smaller than 10 can thus be considered consistent with the working hypothesis of a Gaussian DEM plasma. It does not mean, however, that a Gaussian is the only possible model, but that it is a model consistent with the observations. Since we perform a least-square fit of the six values  $I_b^{\text{obs}} - I_b^{\text{th}}$  by three parameters (EM,  $T_e$ ,  $\sigma$ ), this behavior is expected. The small correlation between the residuals observed in the isothermal case disappears with increasing DEM width. This can be explained by the smoothing of the criterion (see Figure 8) that reduces the directionality of its minima.

For model testing, a reduced chi-squared  $\chi_{\text{red}}^2 = \chi^2/n$ , where  $n$  is the number of degree of freedom, is sometimes preferred over a regular  $\chi^2$  test because it has the advantage of being normalized to the model complexity. Usually,  $n$  is the number of observations minus the number of fitted parameters. This assumes that the measurements are independent, which is what we wanted to test. In practice, a small correlation between the residuals is found in the isothermal case, but the effect is small and a reduced  $\chi^2$  can be used. It should be noted that the residuals have a nonnegligible probability to be greater than the peak of the corresponding  $\chi^2$  distribution. For plasmas

having Gaussian DEMs, for example, the residuals have about a 43% chance of being greater than 3 (Figure 11). This implies that seemingly large residuals are not necessarily proof of the inadequacy of the chosen DEM model. The working hypothesis can only be invalidated if it can be shown that another model has a greater probability of explaining the obtained residuals. This was, for example, the case in Section 2.3.1 where we have shown that if an isothermal inversion gives a squared residual greater than 3, the plasma DEM is more probably Gaussian than isothermal. We now explore a similar situation for Gaussian inversions.

Indeed, in reality the DEM shape is not known and it is interesting to test if a Gaussian is a pertinent model or if AIA has the capability to discriminate between different models. For this purpose, still considering Gaussian DEM solutions, the simulations of the observations are now performed using a top-hat DEM distribution defined as

$$\begin{aligned} \xi_{\text{hat}}(T_e) &= \text{EM} \Pi_{T_e, \sigma}(T_e), \\ \text{with } \Pi_{T_e, \sigma}(T_e) &= \begin{cases} \frac{1}{\sigma} & \text{if } |\log(T_e) - \log(T_c)| < \frac{\sigma}{2} \\ 0 & \text{else} \end{cases}. \end{aligned} \quad (6)$$

Like a Gaussian, this parameterization can represent narrow and wide thermal structures.

Figure 12 gives the associated temperature probability maps. The top panels correspond to simulated plasmas with a top-hat distribution of width  $\sigma^P = 0.1$ . Most of the solutions are concentrated around the diagonal, even though the robustness is somewhat affected for temperatures in the range  $5 \times 10^5 < T_c^P < 10^6$  K, where low probability secondary solutions exist. These two plots are very similar to the top panels of Figure 9, which give the probability of the Gaussian solutions for a

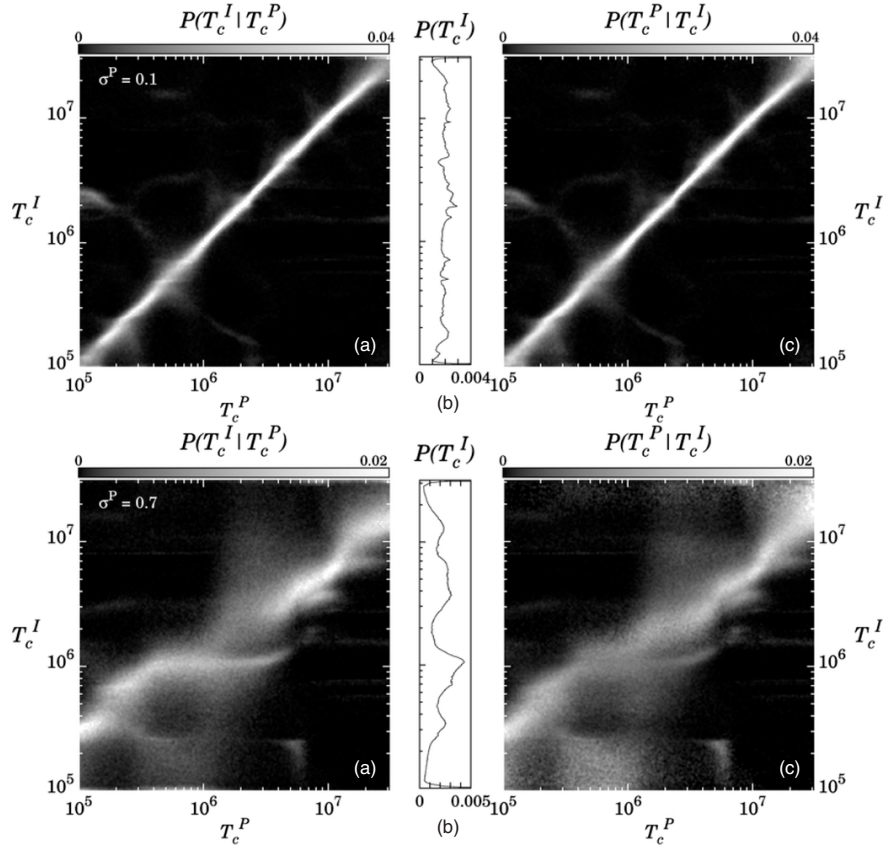


**Figure 12.** Same as Figure 9 but for a plasma having a top-hat DEM. The simulated observations are computed for DEM widths of  $\sigma^P = 0.1$  (top row) and  $0.7 \log T_c$  (bottom row).

Gaussian plasma. Therefore, even though the DEM assumed for the inversion is different from that of the plasma, the central temperature of the top hat is determined unambiguously.

The picture is different for wide plasma DEM distributions. In the bottom panels of Figure 12, with  $\sigma^P = 0.7$ , the diagonal has become very wide, structured and does not cross the origin any more. Some plateaus appear, meaning that for some ranges of plasma temperature  $T_c^P$ , the temperature  $T_c^I$  provided by the Gaussian solutions will be invariably the same. For  $5 \times 10^5 < T_c^P < 3 \times 10^6$  K, for example, a constant solution  $T_c^I = 1$  MK appears, as shown also by  $P(T_c^I)$  (bottom panel (b)). As a result, the inverse conditional probability map  $P(T_c^P | T_c^I)$  (bottom panel (c)) indicates that for an inversion output of 1 MK there is a large indetermination on the central temperature. The behavior of the solutions is thus globally equivalent to that described in Section 3.2 for the inversion of Gaussian DEM plasmas.

The observed distribution of the sum of the squared residual is very similar to those obtained with consistent Gaussian DEM models and is close to a three-degree  $\chi^2$  (see Figure 8). If the working hypothesis were a top-hat DEM, thus consistent with the plasma, the residuals would also be close to a three-degree  $\chi^2$ , as for any DEM model described by three parameters (see discussion above). The solar plasma has no reason to actually have a top-hat DEM. However, this numerical experiments shows that, using AIA data only and the  $\chi^2$  test, the

discrimination between two very different multithermal DEMs is practically impossible.

#### 4. SUMMARY AND DISCUSSION

In this work, we described a complete characterization of the statistical properties of the DEM inversion, rigorously treating both systematic and random errors. The developed methodology has been illustrated in the specific case of the AIA telescope, but the technique is generic and can be applied to any other instrument, spectrometers as well as imaging telescopes. By restricting ourselves to parametric DEMs, we could analyze in detail what occurs during the inversion process, and could therefore point out the fundamental difficulties involved in the DEM reconstruction. Even though only a few simple DEM distributions have been studied, important and generic conclusions regarding the robustness of the inversion problem have been reached. The method can be applied to other forms of DEMs as long as they can be defined by a small number of parameters.

Our technique provides new tools to facilitate the interpretation of the DEM inversion. By computing the  $P(\xi^I | \xi^P)$  probability matrices the robustness can be evaluated, secondary solutions can be detected, and their probabilities can be quantified. Since we do not know whether the systematic errors are over- or underestimated, their randomization in the computation of the inverse conditional probability  $P(\xi^P | \xi^I)$  ensures that all





# Can the Differential Emission Measure constrain the timescale of the energy deposition in the solar corona ?

## D.1

---

### **Résumé**

Dans cet article, une analyse des capacités du spectromètre *Hinode*/EIS à détecter des signatures radiatives du chauffage coronal est proposée. Plusieurs récentes études observationnelle de régions actives suggèrent que les mécanismes de chauffage à haute et basse fréquences sont tous deux cohérents avec les observations. Discriminer entre ces deux possibilités est important pour pouvoir identifier le (les) mécanisme(s) physique(s) du chauffage. Le formalisme de la Mesure d'Émission Différentielle (DEM) est un diagnostic qui permet de faire cette distinction, à travers l'étude de la pente de la DEM dans la partie basse température. Il est donc crucial de comprendre les incertitudes associées à la mesure de cette pente. En utilisant des estimations rigoureuses des différentes sources d'incertitudes impliquées dans le problème d'inversion, on estime ainsi les intervalles de confiances sur les pentes observées. Nos résultats montrent que l'incertitude associée à la reconstruction de la pente dépend fortement du nombre de raies contraignant la pente. L'incertitude caractéristique est estimée autour de  $\pm 1.0$ , dans les cas les plus favorables.

## D.2

---

**Article publié dans la revue *The Astrophysical Journal***

CAN THE DIFFERENTIAL EMISSION MEASURE CONSTRAIN THE TIMESCALE  
OF ENERGY DEPOSITION IN THE CORONA?C. GUENNOU<sup>1</sup>, F. AUCHÈRE<sup>1</sup>, J. A. KLIMCHUK<sup>2</sup>, K. BOCCHIALINI<sup>1</sup>, AND S. PARENTI<sup>3</sup><sup>1</sup> Institut d'Astrophysique Spatiale, Bâtiment 121, CNRS/Université Paris-Sud, F-91405 Orsay, France; [chloe.guennou@ias.u-psud.fr](mailto:chloe.guennou@ias.u-psud.fr)<sup>2</sup> Solar Physics Laboratory, NASA Goddard Space Flight Center, Greenbelt, MD, USA<sup>3</sup> Royal Observatory of Belgium, 3 Avenue Circulaire, B-1180 Bruxelles, Belgium

Received 2013 May 21; accepted 2013 June 28; published 2013 August 13

## ABSTRACT

In this paper, the ability of the *Hinode*/EIS instrument to detect radiative signatures of coronal heating is investigated. Recent observational studies of active region cores suggest that both the low and high frequency heating mechanisms are consistent with observations. Distinguishing between these possibilities is important for identifying the physical mechanism(s) of the heating. The differential emission measure (DEM) tool is one diagnostic that allows us to make this distinction, through the amplitude of the DEM slope coolward of the coronal peak. It is therefore crucial to understand the uncertainties associated with these measurements. Using proper estimations of the uncertainties involved in the problem of DEM inversion, we derive confidence levels on the observed DEM slope. Results show that the uncertainty in the slope reconstruction strongly depends on the number of lines constraining the slope. Typical uncertainty is estimated to be about  $\pm 1.0$  in the more favorable cases.

*Key words:* plasmas – Sun: corona – Sun: UV radiation – techniques: spectroscopic

*Online-only material:* color figures

## 1. MOTIVATIONS

Understanding how the Sun's outer atmosphere is heated to very high temperatures remains one of the central issues of solar physics today. The physical processes that transfer and dissipate energy into the solar corona remain unidentified and a variety of plausible mechanisms have been proposed (see Parnell & De Moortel 2012; Klimchuk 2006; Walsh & Ireland 2003; Zirker 1993 for a review of the various coronal heating models). If the magnetic origin of coronal heating seems to be currently well accepted (Reale 2010), the details regarding the energy transport from the photosphere to the corona or the energy conversion mechanisms are still open issues. Recently, efforts have focused on determining the timescale of energy deposition in the solar corona, providing constraints on the properties of the heating mechanisms, and allowing for a distinction between steady and impulsive heating scenarios. The nanoflares theory of Parker (1988), for example, is based on the idea that the corona is heated by a series of ubiquitous small and impulsive reconnection events. However, the term nanoflare is now used in a more general way, referring to any impulsive heating event that occurs on a small spatial scale, regardless of the nature of the mechanism (see Cargill 1994; Cargill & Klimchuk 2004; Klimchuk & Cargill 2001). Even wave heating takes the form of nanoflares by this definition (see Klimchuk 2006).

According to the impulsive or steady nature of the heating, coronal loops are predicted to present different physical properties at a given time. Observations suggest that coronal loops are probably not spatially resolved. For this reason more often a loop is modeled as a collection of unresolved magnetic strands, considering a strand to be a fundamental flux tube with an isothermal cross-section. Depending on the timescale of the heating mechanisms involved, the plasma within the individual strand is allowed or not allowed to cool and drain, via a combination of conductive and radiative cooling (Reale 2010). Therefore, the thermal structure of the whole loops will differ, with the proportion of hot to warm material depending on the time delay between heating events.

Recently, several authors took a particular interest in one potential diagnostic of the heating frequency based on the analysis of the slope of the differential emission measure (DEM) of active regions (ARs). Based on both theoretical and observational analysis, earlier analysis reported that the coolward part of the DEMs generally follows a power law, up to the emission measure (EM) peak ( $\sim 3\text{--}5$  MK):  $\text{DEM}(T) \propto T^\alpha$  with  $\alpha$  being the positive slope index (Jordan 1980; Dere 1982; Brosius et al. 1996). This slope provides indications directly related to the heating timescale: a large proportion of hot relative to warm material leads to a steep DEM slope, whereas a shallower slope corresponds to less hot material and more warm material. The former case is consistent with high frequency impulsive heating, where the short time delay (lower or equivalent to the cooling time) between two heating events does not allow for the cooling of a large proportion of material. In the latter case, the time delay between two heating events (now longer than the cooling time) allows the cooling of a significant quantity of the strand material. The limiting case, where the time delay tends to be zero, actually corresponds to the steady heating case, where the strand is continuously heated. Using different combinations of observations from the Extreme-ultraviolet Imaging Spectrometer (EIS; Culhane et al. 2007) on board the Japanese mission *Hinode* (Kosugi et al. 2007), the Atmospheric Imaging Assembly (AIA; Lemen et al. 2012) instrument on board the *Solar Dynamic Observatory* (SDO), and the *Hinode* soft X-Ray Telescope (Golub et al. 2007), several authors recently carried out new AR observational analyses, estimating slope values ranging from 1.7 to 5.17 for 21 different AR cores (Tripathi et al. 2011; Warren et al. 2011; Winebarger et al. 2011; Schmelz & Pathak 2012; Warren et al. 2012).

In the present work, we focus on the investigation of the possibilities of deriving the DEM from observations, and we provide a method to estimate the uncertainties associated with its parameters, especially the slope. We do not refer to any particular physical mechanism, such as magnetic reconnection or the dissipation of waves; we only refer to the timescale of the mechanism *itself*. Technical difficulties related to both

observational processing and diagnosis complicate the slope derivation and thus the associated physical interpretation. In particular, the DEM inversion problem has proven to be a real challenge, due to both its intrinsic underconstraint and the presence of random and systematic errors. Authors have previously been attentive to examining the fundamental limitations of this inversion problem (Craig & Brown 1976; Brown et al. 1991; Judge et al. 1997), and many different inversion algorithms have been proposed (Craig & Brown 1986; Landi & Landini 1997; Kashyap & Drake 1998; McIntosh 2000; Goryaev et al. 2010; Hannah & Kontar 2012). Despite all these attempts, reliably estimating the DEM and the uncertainties associated with the solution remains a major obstacle to properly interpreting the observations.

In this perspective, we developed in recent papers (Guennou et al. 2012a, 2012b, hereafter Papers I and II) a technique, applicable to broadband or spectroscopic instruments, which are able to completely characterize the robustness of the DEM inversion in specific cases. Using a probabilistic approach for interpreting the DEM solution, this technique, briefly reviewed in Section 2, is useful for examining the DEM inversion properties and provides a new means of interpreting the DEM solutions. Assuming that the DEM follows a power law, and applying our technique to the *Hinode*/EIS instrument, we derive estimates of the errors associated with the reconstructed DEM slopes, described in Section 3. The presence of uncertainties radically changes the conclusions regarding the compatibility between observations and models, as shown by Bradshaw et al. (2012) and described in Sections 3 and 4, where we also discuss the results in the context of steady versus impulsive coronal heating.

## 2. METHODOLOGY

The approach used in this work is very similar to that used in Papers I and II. The technique and the DEM formalism are exhaustively described therein, but a quick summary is given below.

### 2.1. Background

Under the assumption of an optically thin plasma, the observed intensity in a spectral band  $b$  can be expressed as

$$I_b = \frac{1}{4\pi} \int_0^{+\infty} R_b(T_e, n_e) \xi(T_e) d \log T_e, \quad (1)$$

where  $T_e$  is the electron temperature,  $\xi(T_e) = \overline{n_e^2(T_e)} dp/d \log T_e$  is the DEM<sup>4</sup> that provides a measure of the amount of emitting plasma as a function of temperature, with  $\overline{n_e^2}$  being the square electron density averaged over the portions  $dp$  of the line of sight (LOS) at temperature  $T_e$  (Craig & Brown 1976).  $R_b(T_e)$  is the temperature response function of a given instrument:

$$R_b(n_e, T_e) = \sum_{X,l} S_b(\lambda_l) A_X G_{X,l}(n_e, T_e) + \int_0^{\infty} S_b(\lambda) G_c(n_e, T_e) d\lambda, \quad (2)$$

where the first term refers to the spectral lines  $l$  of an atom  $X$  of abundance  $A_X$ , whereas the second describes the contribution

<sup>4</sup> We choose to define the DEM on a logarithmic scale, but the DEM can also be defined in linear scale as  $\xi(T_e) = \overline{n_e^2(T_e)} dp/dT_e$ . There is a factor  $d \log T_e/dT_e = 1/(\ln 10 T_e)$  between the two conventions.

of the continua.  $S_b(\lambda)$  is the spectral sensitivity of the spectral band  $b$  of the instrument, and  $G_{X,l}$  and  $G_c$  are the contribution functions taking into account all the physics of the coronal emission processes (Mason & Monsignori Fossi 1994). The total EM is obtained by integrating the DEM over the logarithm of temperature. The inference of the DEM from a set of observations involves the inversion of Equation (1), which is hindered by both the presence of random instrumental perturbations and systematic errors on the instrument calibration and on the atomic physics. The purpose of our work here is to investigate the limitations induced by uncertainties in the DEM inversion process, concentrating in particular on the determination of the slope of the distribution. Our method is quite general, but we will deal specifically with observations obtained by the *Hinode*/EIS spectrometer. Using simulations of the *Hinode*/EIS observations  $I_b^{\text{obs}}$  and comparing them to the theoretical expectation  $I_b^{\text{th}}$ , including the perturbations engendered by the uncertainties, it is possible to quantify the reliability of the DEM inversion of the EIS data.

In simple terms, our approach is essentially the following. We start with an assumed (called “true” hereafter) DEM with a particular functional form. From this we generate a synthetic spectrum, introducing errors associated with unknown atomic physics, instrumental calibration, and photon counting noise. We then determine the DEM that provides the best fit to the synthetic spectrum, which we take to be the DEM that minimizes the differences in the line intensities. This inferred DEM has the same functional form as the true DEM. Only the parameters are different. The most important parameter is the slope, and by comparing the true and inferred slope, we obtain an error in the slope measurement for this particular set of atomic physics, calibration, and noise errors. By running many trials, with many different sets of errors chosen from appropriate probability distributions, we finally deduce an estimate of the uncertainty in the slope determination.

The core of our method resides in the probabilistic approach of the DEM inversion: let us assume a plasma with a true DEM  $\xi^T$ ; the DEM solution  $\xi^I$  is the one that minimizes the criterion  $C(\xi)$ :

$$\xi^I = \arg \min_{\xi} C(\xi),$$

$$C(\xi) = \sum_{b=1}^{N_b} \left( \frac{I_b^{\text{obs}}(\xi^T) - I_b^{\text{th}}(\xi)}{\sigma_b^u} \right)^2. \quad (3)$$

The solution  $\xi^I$  minimizes the distance between the theoretical intensities  $I_b^{\text{th}}$  and the observed ones  $I_b^{\text{obs}}$  in  $N_b$  spectral bands. The normalization  $\sigma_b^u$  corresponds to the standard deviation of the uncertainties. The residuals  $\chi^2 = \min C(\xi)$  provide an indication of the goodness of the fit. It is worth noting that, as mentioned by Testa et al. (2012), Landi & Klimchuk (2010), and Papers I and II, a low  $\chi^2$  does not necessarily imply that the solution is the good one or the only one. While our study has broad applicability, we concentrate specifically on observations from the EIS spectrometer on board *Hinode*. The criterion is in this case the sum of the contribution of 30 components, one per spectral line. We used the set of 30 lines listed in Table 1, identical to the one used by Bradshaw et al. (2012) and Reep et al. (2013) in order to carry out practical comparison between observations and model predictions (see Section 3), using the uncertainties derived in this work. Most of them belong to the more prominent lines in the AR regime (Del Zanna & Mason 2005). Some used lines arise from the

**Table 1**  
List of the *Hinode*/EIS Spectral Lines Used in Our Simulations

Ions	Wavelength (Å)	log (T[K])	Total Uncertainty $\sigma_{\text{unc}}$
Mg v	276.579	5.45	61.03%
Mg vi	268.991	5.65	61.03%
Mg vi	270.391	5.65	61.03%
Mg vii <sup>b</sup>	278.404	5.80	62.85%
Mg vii	280.745	5.80	61.03%
Si vii	275.354	5.80	61.03%
Si ix	258.082	6.05	61.03%
Si x	258.371	6.15	61.03%
Si x	261.044	6.15	61.03%
Fe ix	188.497	5.85	61.03%
Fe ix	197.865	5.85	61.03%
Fe x	184.357	6.05	61.03%
Fe xi	180.408	6.15	61.03%
Fe xi	188.232	6.15	61.03%
Fe xii	192.394	6.20	61.03%
Fe xii	195.119	6.20	61.03%
Fe xiii	202.044	6.25	61.03%
Fe xiii	203.828	6.25	61.03%
Fe xiv	264.790	6.30	61.03%
Fe xiv	270.522	6.30	61.03%
Fe xiv <sup>b</sup>	274.204	6.30	62.85%
Fe xv	284.163	6.35	61.03%
Fe xvi	262.976	6.45	61.03%
S x	264.231	6.15	53.15%
S xiii <sup>b</sup>	256.685	6.40	55.23%
Ca xiv	193.866	6.55	61.03%
Ca xv	200.972	6.65	61.03%
Ca xvi	208.604	6.70	61.03%
Ca xvii <sup>b</sup>	192.853	6.75	62.85%

**Notes.** Lines are sorted by elements as a function of the peak temperature of the contribution functions. The blended lines are specified with the index *b*. The fourth column indicates the percentage of total uncertainty applied to each spectral line, resulting from both systematic and random errors.

same ion species, and thus we only have 20 different ion formation temperatures available to constrain the DEM. Column 4 of Table 1 indicates the temperatures where the contribution functions peak. However, these additional lines are used in practice as redundant information to decrease the uncertainties. Using Monte Carlo simulations of the instrumental noises  $n_b$  and systematic errors  $s_b$  (see Section 2.3 for a detailed description of the uncertainties), the conditional probability  $P(\xi^I|\xi^T)$  to obtain the inferred DEM  $\xi^I$  knowing that the true DEM is  $\xi^T$  can be computed. Then, the inverse conditional probabilities  $P(\xi^T|\xi^I)$ , giving the probability that the true DEM is  $\xi^T$ , knowing the inferred results can be deduced from Bayes' theorem. This latter quantity contains all the information possible to extract from a set of observations given the level of uncertainties.

Thus, the range or multiple ranges of solutions able to explain the observations within the uncertainties can be identified. The derivation of  $P(\xi^T|\xi^I)$  requires knowing  $P(\xi^I)$ , and, obviously, because of the uncertainties, a great number of solutions  $\xi^I$  can be potentially consistent with a set of observations. Therefore, the computation of this probability is practical only if the space of the solutions is limited, for otherwise it would require the exploration of an infinite number of possible DEMs. For practical reasons, the number of parameters defining the DEM is limited to four: the slope  $\alpha$ , the temperature

of the peak  $T_p$ , the cutoff at high temperature  $\sigma$  and the total EM.

## 2.2. Active Region DEM Model

In order to represent in a more realistic way the observed DEMs, we used the following parameterization of the AR DEM model, represented for different sets of parameters in Figure 1.

1. A power law for the low temperature wing:  $T_e < T_0$

$$\xi_{\text{AR}}(T_e) = k \text{EM} \times T_e^\alpha$$

with  $k = T_0^{-\alpha} \mathcal{N}_{0.15}(\log T_0 - \log T_p)$

and  $\mathcal{N}_\sigma(x) = \frac{1}{\sigma\sqrt{2\pi}} \exp\left(-\frac{x^2}{2\sigma^2}\right)$ , (4)

where  $\alpha$  is the slope of the DEM coolward of the DEM peak,  $T_p$  is the temperature of the DEM peak, and EM is the total EM. The normalization constant  $k$  is used to ensure the continuity and smoothness of the DEM model: the slope must be tangent to the fixed Gaussian connector (see below), at the point  $T_0$ , depending on the slope value.

2. A Gaussian high temperature wing:  $T_e > T_p$

$$\xi_{\text{AR}}(T_e) = \text{EM} \mathcal{N}_\sigma(\log T_e - \log T_p), \quad (5)$$

where  $\sigma$  is the standard deviation of the Gaussian wing. Thus, beyond the temperature of the DEM peak, the DEM is described by a Gaussian distribution at high temperature, defined by the  $\sigma$  parameter.

3. A fixed width Gaussian connection:  $T_0 < T_e < T_p$

$$\xi_{\text{AR}}(T_e) = \text{EM} \mathcal{N}_{0.15}(\log T_e - \log T_p), \quad (6)$$

where  $T_0$  is the point where the slope  $\alpha$  is tangent to the fixed Gaussian  $\mathcal{N}_{0.15}$ . The connector has been added to ensure that the DEM model is continuous and smooth, corresponding to a continuous first derivative.

A large range of DEM parameters is explored, computing the reference theoretical intensities  $I_b^0$ , used to deduce  $I_b^{\text{obs}}$  and  $I_b^{\text{th}}$  (see Section 2.3), for electron temperatures  $T_e$  ranging from  $\log T_e = 5$  to  $\log T_e = 7.5$  in steps of  $0.005 \log T_e$ . The slope  $\alpha$  varies from 1.0 to 6.0 in steps of 0.05, and the high temperature wing is explored from  $\sigma = 0.01$  to  $0.05 \log T_e$  in steps of 0.01. The total EM varies between  $3 \times 10^{26}$  and  $3 \times 10^{29} \text{ cm}^{-5}$  with a resolution of 0.1 in logarithmic scale, and the temperature of the peak  $T_p$  varies between  $\log T_p = 5.9$  and  $\log T_p = 6.9$  in steps of 0.02. Limiting the possible range of each parameter allows us to pre-compute once and for all the reference theoretical intensities  $I_b^0$  as a function of the four parameters  $\alpha$ ,  $\sigma$ ,  $T_p$ , and EM, for each of the 30 lines used in this work (Table 1). The variation interval of each parameter is in good agreement with the current observational measurements. Figure 1 illustrates the large range of parameters explored in this work. The EM is fixed to the typical AR value of  $\text{EM} = 10^{28} \text{ cm}^{-5}$  while the others parameters  $\alpha$ ,  $\sigma$ , and  $T_p$  are allowed to vary. The five curves on the left are all drawn for the same peak temperature  $T_p = 10^6 \text{ K}$  and a fixed Gaussian high temperature wing of  $\sigma = 0.1 \log T_e$ , whereas the slopes varies between 1 and 5. The last five curves on the right display the variation of the high temperature wing: the central temperature  $T_p$  and the slope  $\alpha$  are now fixed to, respectively,  $T_p = 10^{6.8} \text{ K}$  and  $\alpha = 5$ , whereas the  $\sigma$  parameter varies between 0.05 and 0.49.

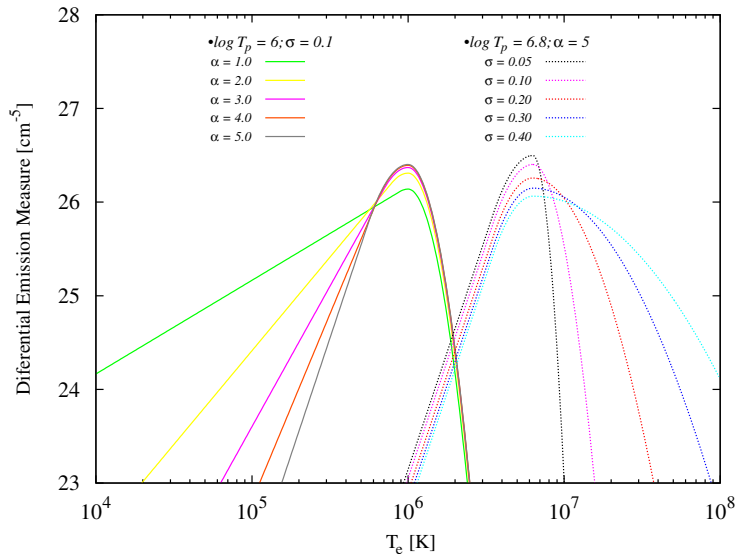


**Figure 1.** Some examples of the parameterization of the AR DEM model (see Section 2.2). The total emission measure is adjusted to the typical AR value of  $EM_{AR} = 10^{28} \text{ cm}^{-5}$ . The left group illustrates the slope variations, whereas the right group depicts variety of high temperature wing parameterizations. In the first case, the temperature of the coronal peak and the width of the high temperature part are fixed to, respectively,  $T_p = 10^6 \text{ K}$  and  $\sigma = 0.1 \log T_e$ , while the slope of the five distinct parameterizations varies between 1 and 5. On the right, the peak temperature is increased to  $T_p = 10^{6.8} \text{ K}$  and the slope is fixed to  $\alpha = 5$ , while the  $\sigma$  parameter varies between 0.05 and 0.4.

(A color version of this figure is available in the online journal.)

### 2.3. Uncertainties

Following the initial reasoning of Paper I, the theoretical intensities  $I_b^{th}$  and  $I_b^{obs}$  can be expressed as  $I_b^{th} = I_b^0 + s_b$  and  $I_b^{obs} = I_b^0 + n_b$ , where values of  $I_b^0$  are called the reference theoretical intensities,  $n_b$  are the random perturbations, and  $s_b$  are systematic errors. The reference theoretical intensities are equal to  $I_b^{obs}$  and  $I_b^{th}$  in the case of hypothetically perfect knowledge of the atomic physics and observations. They have been computed via Equations (1) and (2) and using the given AR DEM model  $\xi_{AR}$  (see Section 2.2). We used the CHIANTI 7.1 atomic database (Dere et al. 1997; Landi et al. 2013), and for each of the spectral lines  $b$  listed in Table 1, the EIS reference theoretical intensities have been calculated using the function `eis_eff_area` (Mariska 2010) of the Interactive Data Language *Solar Software* package.

The different nature of the random and systematic uncertainties  $n_b$  and  $s_b$  affects the observations in distinct ways (Taylor 1997). The random errors affect the data in an unpredictable way, i.e., they could be revealed by a hypothetically large number of experiments, the error on each measurement differing for each attempt. A set of *Hinode*/EIS observations is randomly perturbed by various factors: the Poisson photon shot noise and the detection noises, such as thermal or read noise, often assumed to be Gaussian. These phenomena are well known and can be realistically simulated: Poisson perturbations  $P_\lambda$  and  $\sigma_{ccd} = 6e^-$  rms (McFee 2003) of Gaussian CCD read noise are added, before conversion to digital numbers, using the conversion gains of the EIS spectrometer.

In contrast, the systematic uncertainties cannot be revealed by the repetition of the same experience, always pushing the results in the same direction and thus leading to a systematic and *unknown* over- or underestimation. Besides, it is difficult to estimate the probability distribution of the systematics. In

the following, the probability distribution of such uncertainties will be considered to be Gaussian, as is generally assumed. The observational intensities  $I_b^{obs}$  are affected by the uncertainty associated with the calibration of the instrument, estimated by Culhane et al. (2007) to be around  $\sigma_{cal} = 25\%$  for the two different CCD cameras of the EIS instrument. This uncertainty refers to the absolute calibration. We used two independent Gaussian variables to model it, one for each camera. All the lines falling on one camera are perturbed by the same amount for each random realization of the uncertainties. The difference between the two cameras can be as large as 40%. In the second set of uncertainties described in Section 3, this difference is reduced to 20%. In addition, the degradation of the instrument response over time can also include an additional systematic uncertainty, biasing the results in a given direction.

The theoretical expectations  $I_b^{th}$  are impacted by a complex chain of uncertainties of a different nature. Thus, the estimation of the errors on the contribution functions  $G_c$  and  $G_{X,I}$  (see Equation (2)) is a more challenging task. In particular, recasting the expression of the observed intensities into Equation (1) is possible only via several implicit physical assumptions (Judge et al. 1997): the plasma is considered to be an optically thin gas, in statistical and ionization equilibrium. The electron velocity distribution function is generally considered to be Maxwellian, as in the CHIANTI database, and the abundance of each element must be constant over the LOS. A discrepancy of the observed coronal plasma with one of these assumptions potentially affects the interpretation of the data. For example, the observed enhancement of the low first ionization potential (FIP) elements (Young 2005) in the solar corona possibly induces a non-uniformity of the abundances along the LOS.

Incompleteness in the atomic databases, such as missing transitions, or inaccuracy in some physical parameters such as ion–electron collision cross-sections, de-excitation rates,



etc., also results in systematic uncertainties. For example, the recent release from version 7.0 to version 7.1 of the CHIANTI spectral code (Landi et al. 2013), including important improvements in the soft X-ray data, clearly shows that version 7.0 of the CHIANTI database was incomplete in the 50–170 Å wavelength range, leading to strong inaccuracy in the emissivity calculations of some Fe ions from Fe VIII to Fe XIV. These updates particularly affect the temperature response function of the 94 and 335 Å channels of the *SDO*/AIA instrument. Atomic structure computations are based on two different types of electron scattering calculations: the distorted wave (see Crothers 2010 for details) or the close coupling approximation (see McCarthy & Stelbovics 1983 for details), the latter being generally more accurate. Ionization balance implies equilibrium between the ionization and recombination processes, but if the plasma is out of equilibrium or in a dynamic phase, the CHIANTI calculations of line intensities are not consistent with the observations. However, these effects should not be important except for very hot plasmas produced by impulsive heating (Bradshaw & Klimchuk 2011; Reale & Orlando 2008), and possibly also for cool plasmas well below 1 MK, when the radiative cooling can greatly accelerate (Raymond 1990; Reale & Landi 2012; Cargill & Bradshaw 2013). In those regimes, temperature-sensitive line ratios of individual ions may be a better way to constrain the models (Raymond 1990). Within the temperature range used, the evolution is slow enough and the density is high enough that ionization equilibrium is generally a good approximation. In any case, out-of-ionization equilibrium conditions add an additional uncertainty to the DEM analysis as usually performed. In that sense, our results on the slope uncertainties are lower limits. The impact of a deviation of the electron velocity distributions from a Maxwellian on the ionization equilibrium and on the electron excitation rates has been studied by Dzifčáková (1992, 2000), showing that the intensities of spectral lines can be significantly altered. The effects of radiative loss inaccuracy has also been investigated by Reale & Landi (2012), demonstrating that changes in radiative loss has an important impact on the plasma cooling time, which itself impacts the conclusions of the impulsive heating models. Some studies have been recently carried out to evaluate the impact of using inconsistent atomic physics data in the DEM inversion process (Landi & Klimchuk 2010; Landi et al. 2012; Testa et al. 2012) and found that the DEM robustness can be significantly altered, leading to important uncertainties on the reconstruction accuracy.

To take into account all these effects, we include the uncertainties in our Monte Carlo simulations using normally distributed random variables. For each realization (each simulation), we choose a number randomly from a Gaussian distribution with a half-width  $\sigma_i$ , considering the four following separate classes.

1. *Class 1.* The first uncertainty class  $\sigma_{at}$  involves errors that are different for each and every spectral line; thus we used 30 independent Gaussian random variables to model it (i.e., a different random number for each line). These include errors in the radiative and excitation rates, atomic structure calculations, etc.
2. *Class 2.* The second class  $\sigma_{ion}$  involves errors that are the same for every line of a given ion but different for different ions. We used the same random number for multiple lines of the same ion (e.g., Fe XIV 264, 270, and 274 Å), but different random numbers for different ions, thus resulting in 20 independent Gaussian random variables (3 different Mg ions, 3 Si ions, 8 Fe ions, 2 S ions and 4 Ca ions). This class

corresponds to errors in the ionization and recombination rates.

3. *Class 3.* The third class  $\sigma_{abu}$  involves errors that are the same for every line of a given element, but different for different elements; thus we used five different Gaussian variables (one per element). These are errors in the elemental abundances that are unrelated to the FIP effect.
4. *Class 4.* Finally, the fourth class,  $\sigma_{fip}$ , involves the additional errors that are the same for every low-FIP element corresponding to errors on the coronal abundance of such elements. In order to simulate this effect, we adopted a mean FIP bias of 2.5, then adding an uncertainty of  $\sigma_{fip}$  on this enhancement factor itself, through an identical Gaussian variable. All our sets of spectral lines, except the two Sulfur lines are finally perturbed in the same way.
5. In addition to these atomic physics uncertainties, a generic uncertainty of  $\sigma_{ble} = 15\%$  is added on the blended lines, to account for the added technical difficulties to extract a single line intensity from the data. Blended lines are underlined by a *b* in the EIS spectral lines list in Table 1.

Each theoretical line intensity  $I_b^{th}$  is then modified by the sum of the four random numbers representing the four uncertainty classes (plus a fifth random number in case of blended lines), leading to  $I_b^{th} = [(1+R_1)(1+R_2)(1+R_3)(1+R_4, \text{ if low FIP})(1+R_5, \text{ if blended})]I_b^0$ . Note that the  $R_i$  values are equally likely to be positive or negative, and the amplitude of the random number is very likely to be less than the Gaussian half-width but will occasionally be larger and on rare occasion will be much larger. All the random numbers are reset for each new realization. The resulting uncertainty of each spectral line is reported in Column 4, where the  $\sigma_{unc}$  is obtained by quadratically summing all the sources of uncertainty, as is appropriate if the errors are independent:  $\sigma_{unc}^2 = \sigma_{at}^2 + \sigma_{ion}^2 + \sigma_{abu}^2 + \sigma_{cal}^2 + \sigma_{fip}^2 + \sigma_{ble}^2$  if applicable).

In order to determine appropriate amplitudes for the four classes of uncertainty related to atomic physics, we polled a group of well-known solar spectroscopists (G. Del Zanna, G. Doschek, M. Laming, E. Landi, H. Mason, J. Schmelz, and P. Young). There was a good consensus that the generic amplitudes are approximately  $\sigma_{at} = 20\%$  for class 1 and  $\sigma_{ion} = \sigma_{abu} = \sigma_{fip} = 30\%$  for each of the other three classes. It was noted, however, that the errors could be substantially larger or smaller for specific spectral lines. Adding these uncertainties in quadrature leads to a total atomic physics uncertainty ranging between 46.9% and 57.6%. In subsequent discussions with the spectroscopy experts, the opinion was expressed that a total uncertainty of this magnitude is too large for some well-studied lines. Compatibility checks can be applied to observations, which sometimes suggest smaller uncertainties. For example, if several lines from the same ion, e.g., Fe XIV, consistently imply a similar EM, then the class 1 errors (excitation rates) are probably small for those lines. Another example is that if the iron lines representing different stages of ionization (Fe X, XI, etc.) follow a consistent trend, such as implying a smooth DEM, then the class 2 errors (ionization rates) are probably small for these lines.

We have therefore considered a second set of uncertainties leading to a total uncertainty (i.e., atomic physics plus calibration) ranging between 25% and 30%, to obtain values of uncertainties typically used in observational analysis: classes 1–4 are now evaluated to 10%, whereas the calibration errors are decreased to  $\sigma_{cal} = 20\%$ . The results corresponding to both of

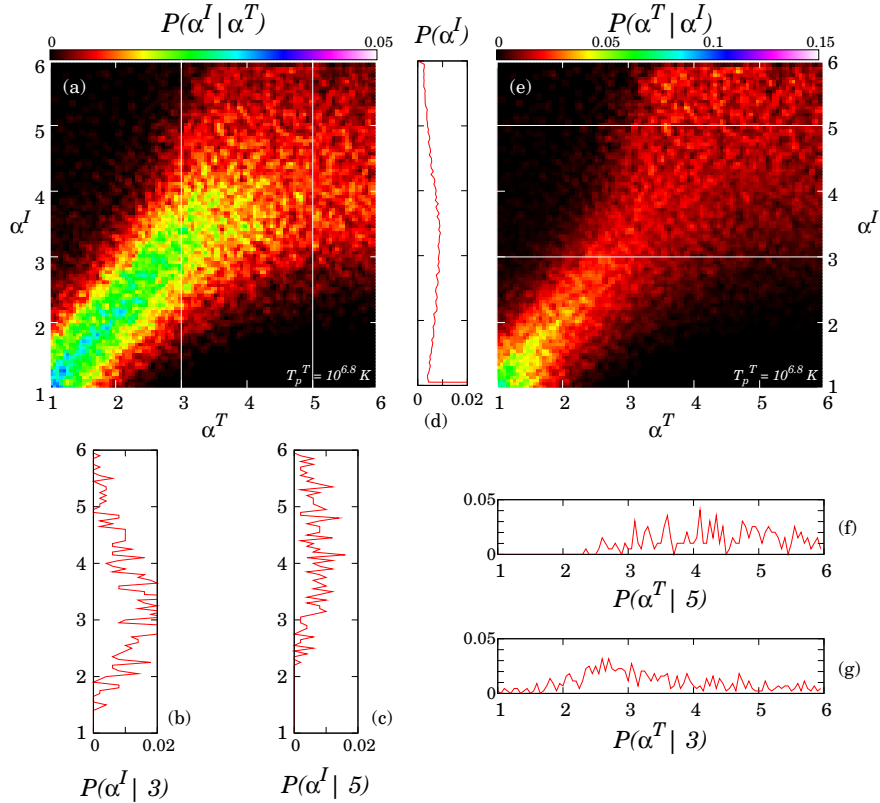


**Figure 2.** Maps of probability for the DEM slope, considering an active region (AR) DEM (see Figure 1), and achieved by 1000 Monte Carlo realizations of the random and systematic errors  $n_b$  and  $s_b$ . In this case, the true DEM is characterized by constant emission measure  $EM_{AR}^T = 10^{28} \text{ cm}^{-5}$ , a fixed high temperature wing of  $\sigma^T = 0.2 \log T_e$  and a peak temperature of  $T_p^T = 10^{6.8} \text{ K}$ ; only the  $\alpha^T$  parameter is investigated here. (a) Probability map  $P(\alpha^I | \alpha^T)$ , vertically reading. (b) and (c) Probability profiles of  $\alpha^I$  for true parameter  $\alpha^T = 3$  and 5 corresponding to vertical lines in panel (a). (d) Total probability  $P(\alpha^I)$  to obtain  $\alpha^I$  whatever  $\alpha^T$ . (e) Vice versa, probability map  $P(\alpha^T | \alpha^I)$ , horizontally reading, inferred by means of Bayes' theorem. (f) and (g) Probability profiles of  $\alpha^T$ , knowing that the inversion results are, from top to bottom, 5 and 3. From these probability distributions, the slope mean and confidence level are estimated to be  $\alpha^T = 4.47 \pm 0.87$  for panel (f) and  $\alpha^T = 3.39 \pm 1.07$  for panel (g); see the text in Section 3 for details.

(A color version of this figure is available in the online journal.)

these sets of uncertainties are presented in Section 3. Ultimately, a customized set of uncertainties should be developed for the specific line lists that have been used in published studies. This is beyond the scope of our present investigation but is something we plan for the future. Until such customized uncertainties are available, it is our opinion that the primary set of uncertainties (20%, 30%, 30%, and 30%) are the most appropriate for estimating the uncertainties in the DEM slope. Atomic physics uncertainties are difficult to determine, but the associated systematic errors have decreased in the last decades thanks to more sophisticated computation facilities and more accurate atomic physics experiments.

Even though we have tried to simulate the systematic errors in a realistic way, some additional sophistications could also be added in our model. Our treatment of class 1 and 2 uncertainties as intensity modifications is an approximation. In reality, errors in excitation, ionization, and recombination rates are manifested as modifications in the  $G_{X,l}$  and  $G_c$  contribution functions of the lines (see Equation (2)). These functions change shape and central position as well as amplitude. A given modification in  $G_{X,l}$  or  $G_c$  will therefore produce an intensity change that depends on the DEM. Treating this properly could be done in the future but is beyond the scope of this initial work. Future

studies might also account for the correlation between various uncertainties. For example, if the class 2 error for Fe XIV is positive, the class 2 error for Fe XIII and Fe XV is likely to be negative.

### 3. RESULTS

In order to quantify the influence of both random and systematic errors, we performed several Monte Carlo simulations with the uncertainties described in Section 2.3 and the AR DEM model described in Section 2.2. The 30 lines described in Table 1 have been used. The simulated observations  $I_b^{\text{obs}}$  and the theoretical intensities  $I_b^{\text{th}}$  have been calculated with the same AR DEM model. In this way, the model can perfectly represent the simulated EIS data. Since the solutions correspond by definition to the absolute minimum of the least-square criterion (Equation (3)), all solutions are fully consistent with the simulated data. Thus, the comparison between the input simulated data and the inversions reveal limitations associated with the presence of uncertainties, and not by the inversion scheme *itself*. We argue that this is actually an optimistic case, since a practical analysis of real observations generally uses blind inversion. The different existing DEM solving algorithms, whether they

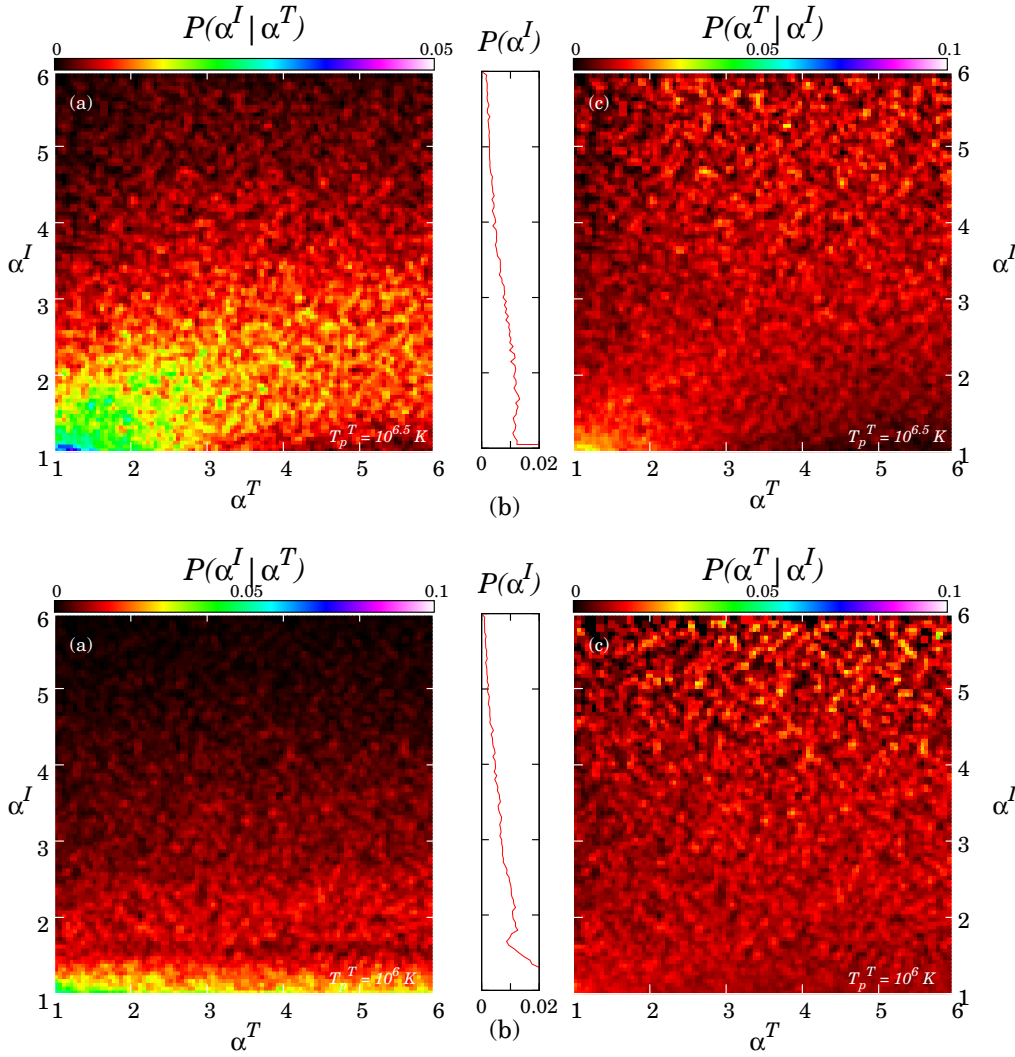


**Figure 3.** Same as Figure 2 but with a true DEM characterized by peak temperatures of, respectively,  $T_p^T = 10^{6.5}$  and  $T_p^T = 10^6$  K, from top to bottom. The decrease of the number of constraining lines associated with the uncertainties clearly deteriorates the quality of the inversion, increasing the confidence level to a typical value of 1.3 (see also Figure 6).

(A color version of this figure is available in the online journal.)

are based on forward or inverse methods, include additional assumptions to ensure uniqueness, such as the smoothness of the solution. Thus, the mathematical difficulties inherent in solving the inverse problem generally introduce additional ambiguity in the results, while our method allows us to separate the sources of error and to study the impact of uncertainties only.

In the following, the four parameters defining the simulated observations with a true AR DEM are denoted  $EM^T$ ,  $T_p^T$ ,  $\sigma^T$  and  $\alpha^T$ , respectively, whereas the associated inferred parameters resulting from the least-square minimization are denoted  $EM^I$ ,  $T_p^I$ ,  $\sigma^I$  and  $\alpha^I$ . It is useful to think of the coronal plasma parameters as the “true” values, while the inverted ones can be thought of as the “observed” values. To reduce the number of dimensions and for the sake of clarity, we choose to fix the EM of the simulated observations  $I_b^{\text{obs}}$  to a constant value  $EM_{\text{AR}}^T = 10^{28} \text{ cm}^{-5}$ , typical of ARs. Since we focus our

attention on the ability to reconstruct the slope coolward of the peak of the DEM ( $\alpha$  parameter), we also fix the width of the high temperature wing  $\sigma$  in both our simulated observations  $I_b^{\text{obs}}$  and theoretical expectations  $I_b^{\text{th}}$ : only the EM,  $\alpha$ , and  $T_p$  are solved for here. The width  $\sigma$  is fixed to the arbitrary constant value  $\sigma^T = \sigma^I = 0.2 \log T_e$ . We verified that the value of  $\sigma$  does not affect the results on the slope. Thus, the probability matrices  $P(EM^I, T_p^I, \sigma^I = 0.2, \alpha^I | EM^T = EM_{\text{AR}}^T, T_p^T, \sigma^T = 0.2, \alpha^T)$  are finally reduced to five dimensions. To illustrate the main properties of these large matrices, we display them by different combinations of fixed parameter values and summation over axes.

The probability maps resulting from such a simulation are displayed in Figure 2 for DEMs characterized by a peak temperature of  $T_p^T = 10^{6.8}$  K. The probabilities are presented regardless of the  $EM^I$  and the peak temperature  $T_p^I$  by integrating



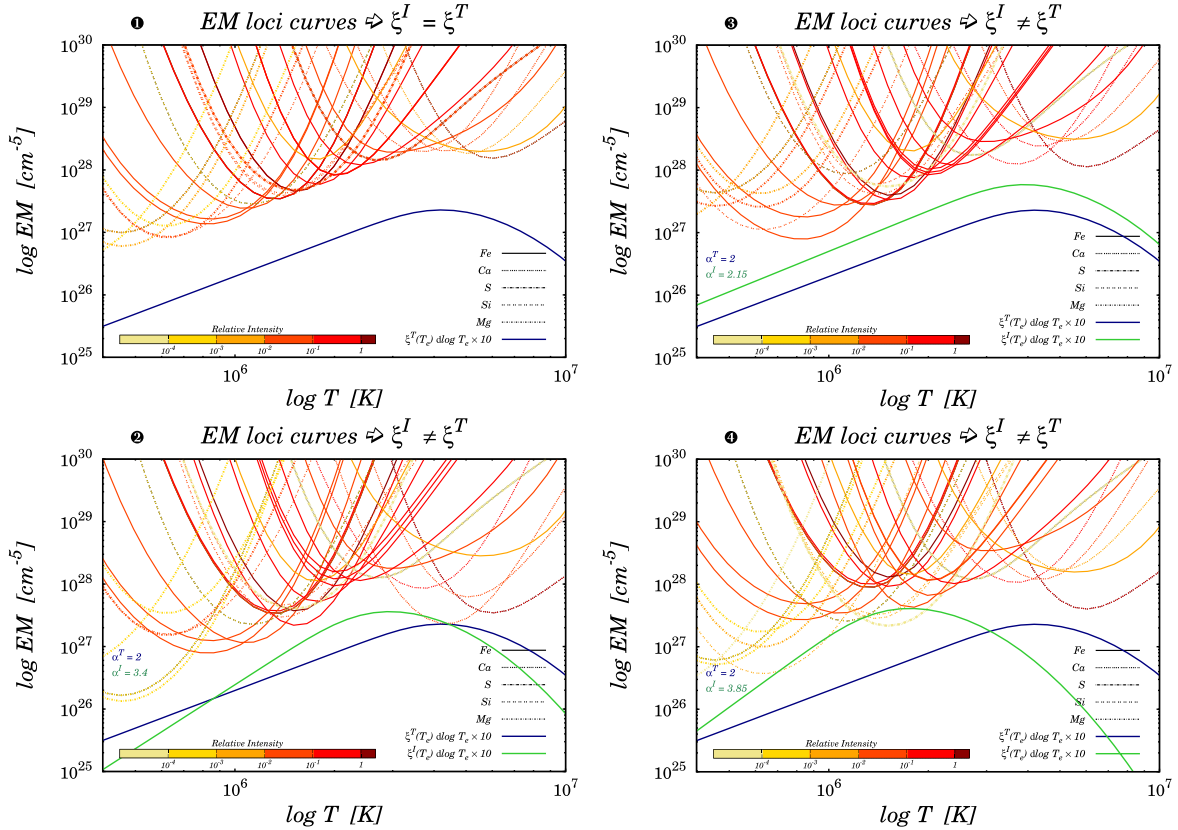


**Figure 4.** Left: Illustration of the potential discrepancy between the true DEM  $\xi^T$  (solid blue line) and the estimated one  $\xi^I$  (solid green line), due to the presence of both random and systematic errors. The EM loci curves are represented as a function of the elements, sorted by line type, and as a function of their relative intensity, sorted by color, from pale yellow (faintest) to dark red (strongest). Top: no uncertainty in this first case; thus the inferred DEM  $\xi^I$  is equal to the initial one  $\xi^T$ . Bottom: a given realization of systematic and random errors, leading to a discrepancy between true and inferred DEMs. Right: same as left panels, but for two different realizations of systematic and random errors. The bottom case illustrates an extreme case, leading to a strong discrepancy between input and inferred DEMs.

them over  $EM^I$  and  $T_p^I$ , even though  $EM^I$  and  $T_p^I$  are of course solved for. This allows us to plot two-dimensional probability maps. Panel (a) of Figure 2 displays the conditional probability  $P(\alpha^I|\alpha^T)^5$  of finding a solution  $\alpha^I$  knowing the slope  $\alpha^T$ . Vertical cuts through panel (a) given probability profiles are shown in panels (b) and (c) for the two specific values of  $\alpha^T = 3$  and  $\alpha^T = 5$ , respectively.

The main diagonal structure indicates that the solutions  $\alpha^I$  are linearly correlated with the input  $\alpha^T$ . In  $P(\alpha^I|\alpha^T)$  in panel (a) of Figure 2, the spreading of the solutions around the diagonal implies that a range of inferred results  $\alpha^I$  is consistent with the same true slope parameter  $\alpha^T$ , given the level of uncertainties involved in this problem. We also note that for steep slopes, the spreading of the solutions is greater. This is due to the fact that the emission is, in these cases, dominated by higher temperatures, leading to a loss of low temperature lines, which further reduces the temperature range available to constrain the slope. Panels (b) and (c) show ranges of possible inferred solutions for the same true input parameter: considering  $\alpha^T = 3$  (panel (b)), the distribution of the solutions  $\alpha^I$  is peaked around 3, with more probable values in the 2.5–4 range. In contrast, panel (c) shows that the solutions  $\alpha^I$  consistent with

the input true slope  $\alpha^T = 5$  may be in the 2–6 interval with a quasi-uniform distribution. If no additional independent a priori information is available, the results of inversion are thus highly uncertain.

However, the computed probability map  $P(\alpha^I|\alpha^T)$  is not usable in a practical way, i.e., with the DEM inversion of true observations. Indeed, since the systematics are in reality identical for all measurements, the output  $\alpha^I$  will be always biased in the same way. Ignoring to what extent the theoretical intensities are over- or underestimated, we must take into account all the potential inferred solutions. Therefore, in order to deduce the probability distribution of the true parameters  $\alpha^T$  consistent with a given inferred result  $\alpha^I$  we computed the inverse probability map  $P(\alpha^T|\alpha^I)$  using Bayes's theorem (see Section 2.2 of Paper I for more details). This quantity is therefore the relevant one for interpreting a given inferred result  $\alpha^I$ . Thus, using Bayes' theorem as described in Section 2 and the total probability  $P(\alpha^I)$  displayed in panel (d), the inverse conditional probability  $P(\alpha^T|\alpha^I)$  shown in panel (e) can be computed. A horizontal cut through panel (e) gives the probability distribution of the true slope  $\alpha^T$  for a given observed slope  $\alpha^I$ . Panels (f) and (g) show examples for  $\alpha^I = 5$  and  $\alpha^I = 3$ . The lack of structure in the first case indicates that a large range of true slopes is consistent with the inferred results:  $3 < \alpha^T < 6$ . In the

<sup>5</sup> Defined as the probability for the solutions to be between  $\alpha$  and  $\alpha + \Delta\alpha$ .

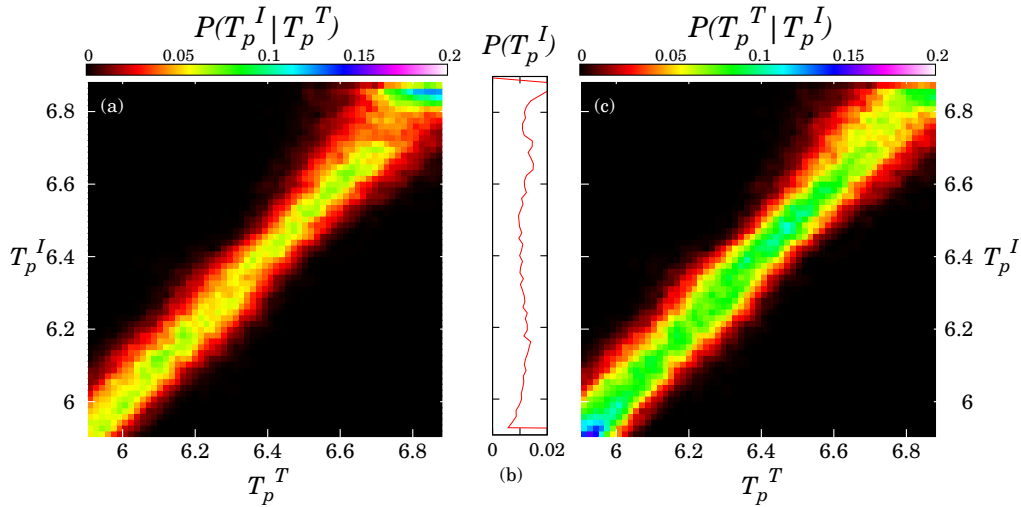


**Figure 5.** Maps of probability for the peak temperature, represented for a simulated observation with a true DEM slope of  $\alpha^T = 1.5$ . Results originate from the same simulations framework as in Figure 2, showing that if the slope is strongly impacted by the presence of uncertainties, the peak temperature is still well constrained, providing confidence levels between 0.7 and 0.85 MK.

(A color version of this figure is available in the online journal.)

second case, the most likely value of the true slope is similar to the observed slope of 3, but there is again a wide range of true slopes that are consistent with this observed slope.

The probability distribution of panel (e) is very useful to assist the DEM inversion interpretation: from this we can compute descriptive statistic quantities such as the standard deviation and the mean of the probability distribution for a given  $\alpha^I$ , which give a quantitative representation of the reconstruction quality and uncertainty. From panel (f), we derived a mean value of  $\bar{\alpha}^P = 4.47$  for a given result of  $\alpha^I = 5$ . The standard deviation, evaluated to 0.87 in this case, characterizing the dispersion of the results, is an estimation of the confidence level on the slope reconstruction. From this, a proper interpretation of the DEM inversion result can be derived, providing a final result of  $\alpha^T = 4.47 \pm 0.87$ , for a given inferred result of  $\alpha^I = 5$ . In panel (g), the mean value is estimated to be  $\bar{\alpha}^P = 3.39$ , whereas the inferred slope was  $\alpha^I = 3$ . The associated standard deviation is 1.07, leading to a final result of  $\alpha^T = 3.39 \pm 1.07$ .

The situation clearly deteriorates as the temperature of the peak temperature decreases. This is illustrated in Figure 3, which is the same as Figure 2 but now for plasmas with true peak temperatures  $T_p^T = 10^{6.5}$  K (top) and  $T_p^T = 10^6$  K (bottom). Compared to the previous case, the probability distributions are clearly wider and less regular. Whatever the inferred result  $\alpha^I$ , the probability distribution of the possible true solutions  $\alpha^T$  extends over the entire possible range. For  $T_p^T = 10^{6.5}$  K, we found a typical standard deviation of 1.3–1.4, similar to the one computed for the extreme low temperature peak of  $10^6$  K. For completeness, the probability maps for 63 peak temperatures  $T_p^T$ , from  $10^{5.9}$  to  $10^{6.9}$  K, and an animation showing the whole amplification of the perturbations are available online at [ftp://ftp.ias.u-psud.fr/cguennou/DEM\\_EIS\\_inversion/low\\_temperature\\_part/slope/](http://ftp.ias.u-psud.fr/cguennou/DEM_EIS_inversion/low_temperature_part/slope/). This deterioration can be explained by the cumulative effects of the decreasing of number of EIS lines and the smaller temperature range available to constrain the slope part of the DEM. In Figure 2, the DEM temperature peak is  $T_p^T = 10^{6.8}$  K and thus all 30 lines constrain the slope and the temperature range in which the slope is allowed

to vary covers 1.35 decades. Considering the case displayed in the top of Figure 3, where  $T_p^T = 10^{6.5}$  K; this number of lines decreases to 26, whereas the temperature range decreases to about 1 decade. In the extreme case of  $T_p^T = 10^6$  K, only eight lines constrain the DEM slope, while the temperature range is reduced to only 0.35 decades.

The potential discrepancy between the true DEM  $\xi^T$  and the inferred one  $\xi^I$  is illustrated in Figure 4 by showing three different realizations of uncertainties (Figure 4 (left bottom) and right panels), as well as the perfect case (Figure 4 (top left)). The EM loci curves, formed by the set of (EM,  $T_e$ ) pairs for which the isothermal theoretical intensities exactly match the observations for a given spectral line (see Del Zanna & Mason 2003 for more details), are represented for each case as a function of both the element, given by the line type, and the relative intensity, given by the color from pale yellow (faintest) to dark red (strongest). In case 1 of Figure 4 (left panels), the loci curves are perfectly aligned, and thus the estimated values of DEM  $\xi^T$  perfectly match the initial true DEM  $\xi^T$ . Case 2 (Figure 4, left) shows a realization of the perturbation  $n_b$  and  $s_b$ , each loci curve being randomly shifted from its original position. This corresponds to a deviation of the solution  $\xi^I$ , the estimated temperature peak being underestimated from  $T_p^T = 4$  MK to  $T_p^T = 2.8$  MK and the slope increased to the steeper value of  $\alpha^I = 3.4$  while the initial true slope was  $\alpha^T = 2.0$ . Note that the relative intensity of each line plays a key role in the reconstruction: the more intense lines have more important weight in the inversion process, even though we normalize the  $\chi^2$  by the different uncertainties sources, including the photon noise (see Equation (3)). Cases 3 and 4 in Figure 4 (right panels) show another different realization of errors leading in case 3 to an overestimation of the total EM, and in case 4 to a significant deviation of the peak temperature  $T_p$ .

The reconstruction of the temperature peak is much better constrained than the slope. Figure 5 displays the probability maps associated with the  $T_p$  parameter, for a true shallow slope  $\alpha^T = 1.5$ , and a constant AR emission measure  $\text{EM}_{\text{AR}}^T$ . Probabilities are now represented whatever the  $\text{EM}^I$  and  $\alpha^I$  by

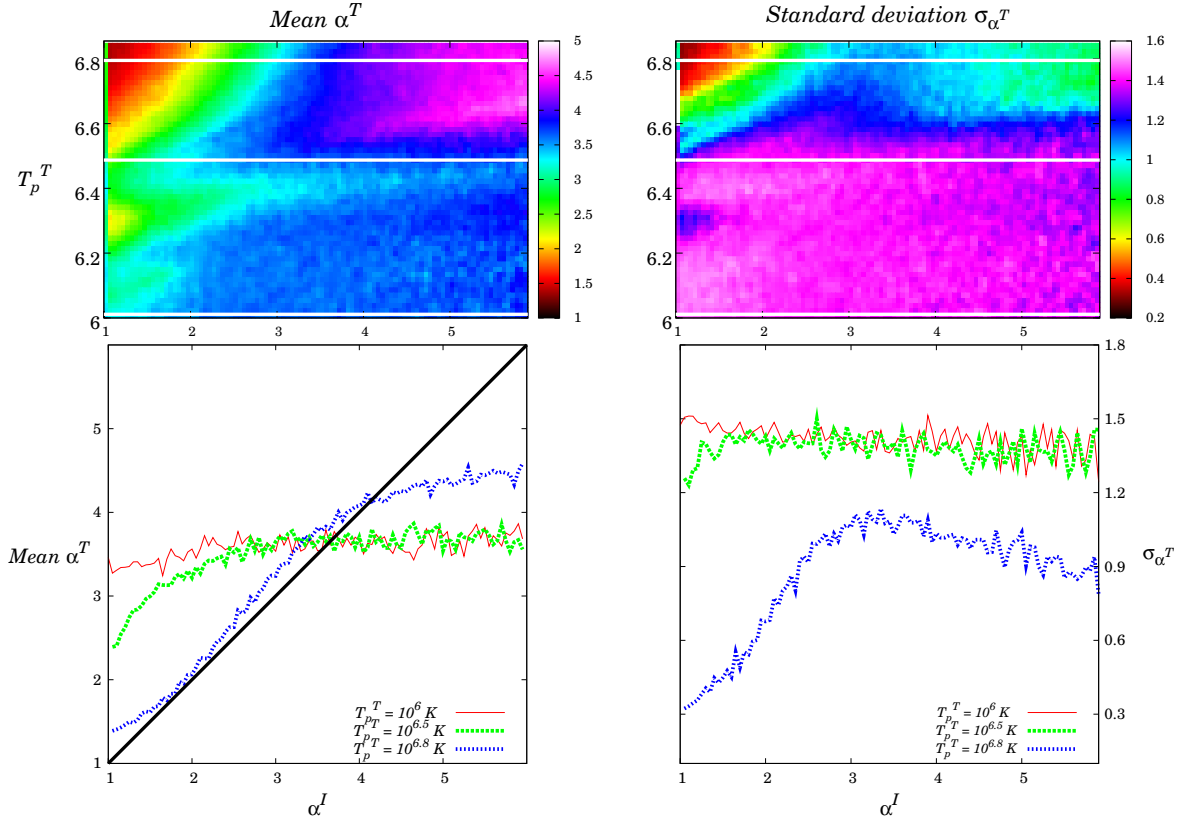


**Figure 6.** Mean and standard deviation of the true slopes  $\alpha^T$  consistent with a given inversion result  $\alpha^I$ . Top: mean (left) and standard deviation (right) maps represented as a function of the peak temperature and the inversion result  $\alpha^I$ . Bottom: cut across the mean (left) and standard deviation (right), corresponding to the white horizontal lines. The peak temperatures are fixed to respectively  $T_p^T = 10^6$  K (solid lines),  $T_p^T = 10^{6.5}$  K (dashed bold lines), and  $T_p^T = 10^{6.8}$  K (dashed lines), corresponding to the probability maps displayed in Figures 2 and 3.

(A color version of this figure is available in the online journal.)

integrating them over the  $EM^I$  and  $\alpha^I$  axes. Results are very similar whatever the chosen input  $\alpha^T$ , and the probability maps presented here are typical.<sup>6</sup> Most of the solutions are condensed around the diagonal. The use of the 30 lines provides an unambiguous determination of the peak temperature. However, the confidence interval remains quite large: we found a typical standard deviation between 0.7 and 0.85 MK associated with the spread of the solutions around the diagonal for the different tested plasma slopes, with extreme values varying between 0.1 and 1.3 MK.

These results can finally be summarized in the two graphs of Figure 6. The first one, on the right, displays the mean slope value of the initial true  $\alpha^T$ , knowing the inferred result  $\alpha^I$ . On the top, the map shows the slope mean value, represented as a function of both the peak temperature  $T_p^T$  and the inferred results  $\alpha^I$ . The quantity  $\alpha^T$  has been computed from the probability distribution  $P(\alpha^T|\alpha^I)$ , in the same way than described previously. The three different horizontal profiles displayed on the bottom and denoted by the horizontal white lines on the top, correspond to the three different probability maps displayed

in Figures 2 and 3. Using these curves, it is possible to correctly interpret the results of the inferred  $\alpha^I$ , thus providing the slope mean value computed from the probability distribution of all true slopes consistent with the given inferred results. The diagonal (solid black line) correspond to a perfect agreement between  $\alpha^T$  and  $\alpha^I$ . The bias of  $\alpha^T$  strongly affects the results for the low temperature profiles  $T_p^T = 1$  MK (solid red line) and  $T_p^T = 3.2$  MK (solid green line), and in a less significant way the high temperature profile  $T_p^T = 6.3$  MK (solid blue line). This bias around the diagonal reflects in reality the initial bias of the solutions observed in the probability maps  $P(\alpha^I|\alpha^T)$  previously presented and taken into account by computing the inverse probability maps  $P(\alpha^I|\alpha^T)$ . For low temperature peaks, the corresponding probability distributions are very wide, almost covering the whole space of the solutions (see Figure 3). Consequently, the slope mean value approaches a roughly constant value of  $\alpha^T = 3.5$ , with, in this case, large associated standard deviation. The behavior of this latter quantity (i.e., the confidence level) is shown on the right side of Figure 6, uniformly ranging between  $\sigma_{\alpha^T} = 1.3$ –1.4 for temperature peak lower than  $T_p^T = 10^{6.5}$  K, as expected in light of the above. For the high temperature peak  $T_p^T = 10^{6.8}$  K, the confidence level extends between 0.3 and 1.15, depending on the value of the inferred slope  $\alpha^I$ .

<sup>6</sup> The probability maps of the peak temperature for 101 values of  $\alpha^T$  ranging from 1 to 6 are available online at [http://ftp.ias.u-psud.fr/cguennou/DEM\\_EIS\\_inversion/low\\_temperature\\_part/slope/](http://ftp.ias.u-psud.fr/cguennou/DEM_EIS_inversion/low_temperature_part/slope/)

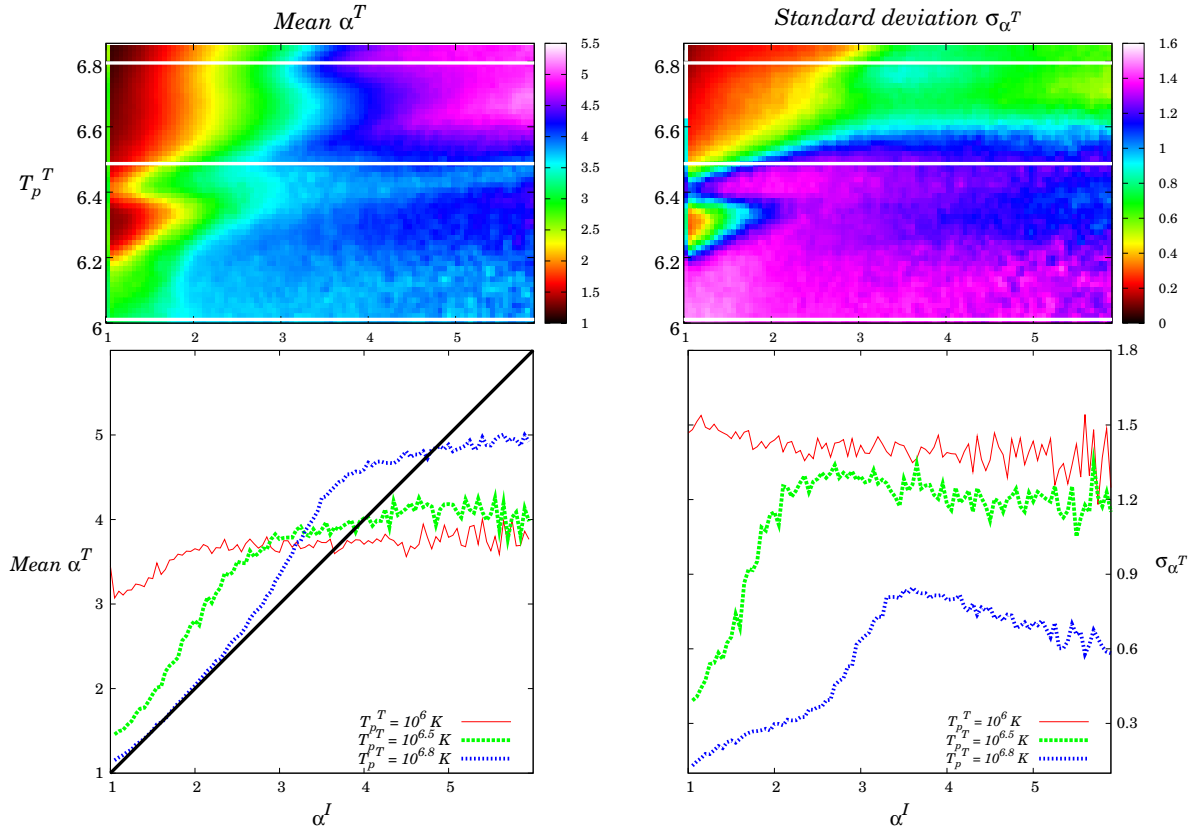


**Figure 7.** Same as Figure 6, but considering now the second set of uncertainties (leading to a total uncertainty ranging between 25% and 30%; see Section 2.3). For AR DEMs with high temperature peak, the confidence level is significantly decreased from 0.9 to 0.6. However, for low temperature peak AR DEMs, results are similar. (A color version of this figure is available in the online journal.)

The summarized results regarding the second set of uncertainties used in this work and described in Section 2.3 are displayed in Figure 7. In this case, the atomic physics uncertainties are greatly reduced from 20% to 10% for class 1 and from 30% to 10% for classes 2 through 4, while the calibration uncertainties are reduced from 25% to 20%. The resulting total uncertainty varies between 25%–30% depending on the line. As expected, the reduced uncertainties lead to an improved correlation between the estimated slope  $\alpha^I$  and the true one  $\alpha^T$ , particularly for the medium temperature peak around  $10^{6.5}$  K. As a result, the standard deviation is decreased, ranging now between 0.2 and 0.8 for  $T_p^T = 10^{6.8}$  K, 0.3 and 1.2 for  $T_p^T = 10^{6.5}$  K, and approaching the same constant value as before, around  $\sigma_{\alpha^T} = 1.4$ . Maps like these in Figures 6 and 7 are useful for interpreting the DEM inversions from true observations: given the slope and the temperature of the peak, both the mean value and the confidence level can be derived.

The confidence levels derived in the present work can be used to evaluate the agreement between theoretical model predictions and DEM measurements. In the recent paper by Bradshaw et al. (2012), the authors carried out a series of low-frequency nanoflare simulations. They investigated a large number of heating and coronal loop properties, such as the magnitude and duration of the nanoflares and the length of the loop. They concluded that the low frequency heating mechanism cannot explain DEM slopes  $\alpha \geq 2.6$ , similar to the findings of

Mulu-Moore et al. (2011). Comparing their results to the current observations of AR cores (see Section 1 for corresponding references), they found that 36% of observed AR cores are consistent with low-frequency nanoflare heating if uncertainties in the slope measurements are ignored. Using, then, the slope uncertainties estimated around  $\Delta\alpha \pm 1$  in this work, they concluded that as few as zero to as many as 77% of AR cores are actually consistent with low-frequency nanoflares. More recently, Reep et al. (2013) studied a scenario they call a “nanoflare train” in which a finite series of high-frequency nanoflares occur within the same loop strand and then cease. The predicted slopes are in the range  $0.88 \leq \alpha \leq 4.56$ . Using again an uncertainty of  $\Delta\alpha \pm 1$ , they concluded that 86% to 100% of current AR core observations are consistent with such trains.

The determination of the uncertainties associated with the atomic physics processes is no simple matter, as discussed in Section 2.3; that is why we have tested two different sets of uncertainties. However, the most important issue here, considering the temperature peaks currently derived in observational analysis, is that whatever the set of uncertainties used to determine the confidence level on the reconstructed slope, their typical values remain important relative to what is necessary to strongly constrain the timescale of the coronal heating. Warren et al. (2012) and Winebarger et al. (2012), for example, derived temperature peak generally around  $\log T_e = 6.6$ , whereas

Schmelz & Pathak (2012) derived temperature peaks generally between  $\log T_e = 6.5$  and  $\log T_e = 6.7$ . For these typical values, the slope uncertainties varies between  $\Delta\alpha = \pm 0.9$  and 1.3 for slopes  $\alpha > 3$  when using the first set of uncertainties, and it varies between  $\pm 0.6$  and 1.0 when using the second set of smaller uncertainties. It appears, therefore, that it is not yet possible to place strong constraints on the coronal heating timescale using observed DEM slopes and the predictions of theoretical models. Further improvements in reducing atomic physics uncertainties are highly desirable.

#### 4. SUMMARY AND CONCLUSIONS

The slope of the DEM distribution coolward of the coronal peak can potentially be used to diagnose the timescale of energy deposition in the solar corona. Indeed the DEM slope provides important information on the proportion of hot to warm material, which is useful to determine the heating timescale. Recent observational studies of AR cores suggest that some AR cores are consistent with low frequency heating mechanisms, where the plasma cools completely before being reheated, while others show consistency with high frequency energy deposition, where rapid reheating causes the temperature to fluctuate about a particular value. Distinguishing between these possibilities is important for identifying the physical mechanism of the heating. It is therefore crucial to understand the uncertainties in measurements of observed DEM slopes.

In this work, we presented an application of our recently developed technique in the specific case of typical AR DEMs, in order to properly estimate confidence level of the observed DEM slopes and assist the DEM interpretation. Using a probabilistic approach and Monte Carlo simulations of uncertainties to interpret the DEM inversion, our method is useful for examining the robustness of the DEM inversion, and to analyze the DEM inversion properties. Comparing simulated observations of the *Hinode*/EIS spectrometer with inferred results, the range or multiple ranges of solutions consistent with a given set of measurement can be estimated, along with their associated probabilities. From such probability distributions, statistical quantities can be derived, such as the standard deviation, providing rigorous confidence levels on the DEM solutions.

In this way, we carefully assess the errors in the DEM slopes determined from *Hinode*/EIS data. Both random and systematic errors have been taken into account. We paid particular attention to the description of the systematic errors related to the atomic physics process and abundances. Uncertainties associated with ionization fractions, elemental abundances, FIP effect, and a combination of uncertainties in the radiative and excitation rates have been simulated. Additional systematic errors have been added to the blended lines, to take into account the technical difficulties in isolating a single line intensity. We argue that our work actually provides an optimistic estimation of the slope confidence levels: the mathematical difficulties intrinsic to solving an inverse problem introduce additional ambiguity, while our method allows us to focus only on the impact of intrinsic uncertainties. The fact that our inverted DEMs have the same functional form as the true ones, known a priori, means that our slope uncertainties are lower limits. In reality, the form of the true DEM is unknown, and this introduces additional uncertainty through the use of blind inversion.

In Section 3, we demonstrated how the slope reconstruction is affected by the uncertainties. The analysis of the probability maps provides a range of slopes consistent with the observed DEM slopes. These maps show that in most cases, a large range

of solutions is consistent with the measurements. The presence of uncertainties degrades the quality of the inversion, leading to typical confidence levels around 0.9–1.0. However, the inversion robustness, and thus the confidence level, largely depends on the number of lines constraining the slope. For DEMs with high temperature peaks [5–6 MK], about 20 lines contain suitable information, while low temperature peaks [1–3 MK] reduce this number to less than 10. For these latter cases, the effect of the uncertainties leads to larger confidence levels, about 1.3 and more in some cases.

The slope confidence levels derived in the present work are useful for quantifying the degree of agreement between theoretical models and observations. Current slope reconstructions can thus be properly compared to theoretical expectations. However, the typical derived confidence levels remain significant compared to the majority of observed slopes values concentrated between 1.5 and 5. The sizable confidence levels make it difficult to draw definitive conclusions about the suitability of a given heating model, implying on one hand that a model might be consistent with the majority of observations or, on the other hand, with none at all (see Bradshaw et al. 2012 for a practical application of these confidence levels). When relaxing the constraint on the DEM slopes as in Reep et al. (2013), the slope DEM diagnostic does not allow us to distinguish between different scenarios because observations can thus be explained by a variety of different heating models.

Our generic approach can be improved for specific datasets and additional sophistication can be incorporated (see Section 2.3). We could, for example, use a customized set of uncertainties for a given set of lines. However, the main important point of our work is that, even for uncertainties that would seem to be on the low end of what is feasible (our second set of uncertainties), the corresponding uncertainty in the measured slope may be too large to definitively exclude or corroborate a given heating scenario in many cases. The methodology presented here can also be used to establish the optimal set of lines required to obtain the smallest possible confidence levels. Such preliminary investigations can be very helpful to optimize future instruments, whether it be spectrometer or broadband imagers, in order to maximize their DEM diagnostic capabilities.

S.P. acknowledges the support from the Belgian Federal Science Policy Office through the international cooperation programs and the ESA-PRODEX program and the support of the Institut d'Astrophysique Spatiale (IAS). F.A. acknowledges the support of the Royal Observatory of Belgium. The work of J.A.K. was supported by the NASA Supporting Research and Technology Program. The authors would like to thank G. Del Zanna, H. Warren, G. Doschek, M. Laming, E. Landi, H. Mason, J. Schmelz, and P. Young for fruitful discussions and comments about atomic physics uncertainties. Discussions with H. Mason, H. Warren, and P. Testa at the second meeting of the Bradshaw/Mason International Space Science Institute Team were also very helpful.

#### REFERENCES

- Bradshaw, S. J., & Klimchuk, J. A. 2011, *ApJS*, 194, 26  
 Bradshaw, S. J., Klimchuk, J. A., & Reep, J. W. 2012, *ApJ*, 758, 53  
 Brosius, J. W., Davila, J. M., Thomas, R. J., & Monsignori-Fossi, B. C. 1996, *ApJS*, 106, 143  
 Brown, J. C., Dwivedi, B. N., Sweet, P. A., & Almléaky, Y. M. 1991, *A&A*, 249, 277  
 Cargill, P. J. 1994, *ApJ*, 422, 381